Development of non-convex artificial aggregates for pavements

A thesis submitted to attain the degree of

DOCTOR OF SCIENCES OF ETH ZURICH
(Dr. sc. ETH Zurich)

presented by

Nicholas A. Conzelmann

MSc Process Engineering, ETH Zurich

born on July 4, 1988

citizen of Germany

accepted on the recommendation of
Prof. Dr. Christoph R. Müller, examiner
Prof. Dr. Erik Schlangen, co-examiner
Dr. Frank J. Clemens, co-examiner
Dr. Lily D. Poulikakos, co-examiner

2022

Table of Contents

Summary

Roads are the infrastructural backbone of civilization, in ancient Egypt for example, roads had their own hieroglyph:

which can be translated into road-with-shrubs [1]. Throughout the times, different construction techniques have been used for roads, nowadays the most common road surfaces are asphalt concrete pavement or unbound gravel. Both types of road surfaces consist primarily of mineral aggregates, typically crushed rock, while for asphalt pavement the aggregates are compounded with bitumen, with a volume fraction of roughly 5%. Despite the importance of aggregates, most research into improving asphalt pavements has focused on the bitumen, for example to reduce the permanent deformation by incorporating polymers into the bitumen or adding bitumen rejuvenators to facilitate the recycling of asphalt pavement. But there is a growing interest to shift the attention towards aggregates, one example is a 2014 report of the United Nations Environment Programme (UNEP) [2] that concludes that viable construction aggregates are becoming rare globally. To tackle this problem, different studies have investigated the replacement of virgin aggregates with aggregates derived from waste materials such as demolition waste. While other studies have investigated the manufacturing of artificial aggregates via sintering of waste incineration ash or the bonding of mineral powders with cementing agents. Each of these studies however have yielded aggregates of random shapes, the question whether artificial aggregates with specifically designed shapes could improve the

properties of asphalt pavements has not been addressed widely in previous work.

This dissertation aims to address this question by first investigating how non-convex aggregate shapes of varying sphericity affect the porosity and permeability of the bulk-structure that is formed by aggregates, the so-called packing. The results show that (i) the porosity increases with decreasing aggregate sphericity, (ii) porosities exceeding 0.7 can be achieved, and (iii) the water permeability increases exponentially with increasing porosity. It was also revealed that permeabilities up to two magnitudes higher compared to the most permeable porous asphalt pavements made with packings of common crushed rock aggregates, which shows the potential of artificial aggregates to improve the properties of permeable pavements.

To investigate whether the shape of artificial aggregates can be varied without affecting the structural properties of their packings, the probability distribution functions of the aggregate stresses were investigated. This investigation revealed that the stress distribution becomes more heterogeneous as the aggregate sphericity decreases, with some aggregates being subject to eight times the average stress. Consequently, the material for the manufacturing of such non-convex artificial aggregates needs to be chosen such that the aggregates can withstand such high stresses.

Alumina ceramic was investigated as a material for the manufacturing of artificial aggregates. To be able to manufacture complex non-convex shapes, additive manufacturing was the method of choice. To this end a ceramic-polymer filament feedstock was prepared that can be used in consumer-grade 3D printers. The 3D printed parts were

subsequently heat treated to evaporate the polymer and sinter the remaining ceramic. This method was successfully used to manufacture complex aggregate shapes, and it was found that the 3D printed parts shrink anisotropically during sintering. The results also show that the parts should be placed in a powder bed during polymer removal to increase the compressive strength of the final aggregate.

This dissertation shows that artificial aggregates with non-convex shapes can improve certain properties of asphalt pavements and reports a protocol to manufacture such aggregates using additive manufacturing. Nonetheless, additional work focusing on the manufacturing, structural and functional durability of non-convex aggregates is necessary for the practical application of artificial aggregates in road pavements.

Zusammenfassung

Straßen sind das infrastrukturelle Rückgrat einer Zivilisation, im alten Ägypten zum Beispiel hatten Straßen ihre eigene Hieroglyphe:

welche als Strasse-mit-Sträuchern übersetzt werden kann [1]. Im Laufe der Jahrtausende wurden verschiedene Bauweisen für Straßen verwendet, heutzutage findet man am häufigsten Asphalt oder ungebundene Schotterbeläge. Beide Arten von Straßenbelägen bestehen hauptsächlich aus mineralischen Zuschlagstoffen, in der Regel gebrochenem Gestein, wobei für Asphaltbelägen die Zuschlagstoffe zusätzlich mit Bitumen mit einem Volumenanteil von etwa 5% gebunden werden. Trotz der grossen Bedeutung der mineralischen Zuschlagstoffe konzentrierte sich die Forschung zur Verbesserung von Asphaltbelägen bisher grossteils auf das Bitumen, z. B. durch die Zugabe von Polymeren zum Bitumen, um die dauerhafte Verformung des Belages zu reduzieren, oder die Benutzung von Bitumenverjüngungsmitteln, um das Recycling der Asphaltbeläge zu verbessern. Es werden jedoch immer mehr Forderungen laut, die Aufmerksamkeit mehr auf die Zuschlagstoffe zu lenken. Ein Beispiel dafür ist ein Bericht des Umweltprogramms der Vereinten Nationen (UNEP) aus dem Jahr 2014 [2], welcher zu dem Schluss kommt, dass brauchbare Bauzuschlagstoffe weltweit immer seltener werden. Um dieses Problem zu lösen, haben verschiedenen Studien der Ersatz von frischen Zuschlagstoffen durch Abfallmaterialien wie Bauschutt untersucht. Andere Studien untersuchten die Herstellung künstlicher Gesteinskörner durch Sintern von

Müllverbrennungsasche oder die Bindung von Mineralpulver mit Zement. Jede dieser Studien hat jedoch Gesteinskörner mit zufälligen Formen hervorgebracht. Die Frage, ob künstliche Gesteinskörner mit speziell entwickelten Formen die Eigenschaften von Asphaltbelägen verbessern könnten, wurde bisher kaum behandelt.

In dieser Dissertation wurde zunächst untersucht, wie sich nichtkonvexe Gesteinskörner mit unterschiedlicher Sphärizität auf die Porosität und die Wasserdurchlässigkeit der von den Gesteinskörnern gebildeten Schüttung, auswirken. Die Ergebnisse zeigten, dass (i) die Porosität mit abnehmender Sphärizität der Gesteinskörner zunimmt, (ii) Porositäten von über 0,7 erreicht werden können und (iii) die Wasserdurchlässigkeit mit zunehmender Porosität exponentiell zunimmt. Es wurden Wasserdurchlässigkeiten beobachtet, welche um bis zu zwei Größenordnungen höher sind verglichen zu den durchlässigsten porösen Asphaltbelägen aus gewöhnlichem Schotter, was zeigt, dass künstliche Gesteinskörner das Potential haben die Eigenschaften von durchlässigen Belägen zu verbessern.

Um zu untersuchen, ob die Form der künstlichen Gesteinskörner beliebig variiert werden kann, ohne die strukturellen Eigenschaften ihrer Schüttungen zu beeinträchtigen, wurden die Wahrscheinlichkeitsverteilungen der mechanischen Spannungen in den Gesteinskörnern untersucht. Dabei zeigte sich, dass die Spannungsverteilung mit abnehmender Sphärizität der Gesteinskörner heterogener wird, wobei einige Gesteinskörner dem Achtfachen der durchschnittlichen Belastung ausgesetzt sind. Folglich muss das Material, welches für die Herstellung solcher nichtkonvexer künstlichen Gesteinskörner verwendet wird, so

gewählt werden, dass die Gesteinskörner diesen hohen Belastungen standhalten können.

Aluminiumoxidkeramik wurde als Material für die Herstellung künstlicher Aggregate untersucht. Um die komplexen nichtkonvexen Formen herstellen zu können, war additive Fertigung die Methode der Wahl. Zu diesem Zweck wurde ein Keramik-Polymer-Filament hergestellt, das in normalen 3D-Druckern für Heimanwender verwendet werden kann. Die 3D-gedruckten Teile wurden anschließend wärmebehandelt, um das Polymer zu verdampfen und die Keramik zu sintern. Mit dieser Methode konnten erfolgreich künstliche Gesteinskörnern mit komplexen Formen hergestellt werden. Dabei stellte sich heraus, dass die 3D-gedruckten Teile während des Sinterns anisotrop schrumpfen. Es zeigte sich auch, dass die Teile während der Polymerentfernung in ein Pulverbett gelegt werden sollten, um Mikrorisse zu vermeiden und die Druckfestigkeit der fertigen Gesteinskörner zu erhöhen.

Diese Dissertation zeigt, dass künstliche Gesteinskörner mit nichtkonvexen Formen bestimmte Eigenschaften von Asphaltbelägen verbessern können und ein Vorgehen, welches zeigt wie solche Gesteinskörner mittels additiver Fertigung hergestellt werden können. Für die praktische Anwendung von künstlichen Gesteinskörnern in Straßenbelägen ist jedoch weitere Forschungsarbeit nötig, welche sich insbesondere mit der Herstellung, sowie der Dauerhaftigkeit der Struktur und der funktionellen Eigenschaften von nichtkonvexen Gesteinskörnern befasst.

1   Introduction

Road surfaces cover 2.1% of Switzerland [3]. These surfaces are largely made up of roads paved with asphalt concrete or unbound roads, usually with a surface of compacted gravel. Both construction techniques are based on aggregates, typically crushed rock or gravel. For gravel roads the aggregates are poured and compacted, while for asphalt concrete the aggregates are bound by bitumen with a fraction of approximately 5%. In Switzerland, gravel surfaces are exclusively used for poorly frequented agricultural roads, more important roads such as urban roads or highways are always paved. Consequently, in the past research has focused on the improvement of asphalt pavements.

1.1   State of the art in pavement research

To improve the performance and sustainability of asphalt pavements some general trends have been identified, such as polymer modification of the bitumen phase to decrease the permanent deformation of pavement [4,5], fiber reinforcement of asphalt [6] and the incorporation of recycled asphalt pavement [7]. Further research lead to novel developments such as self-healing asphalt [8] and energy harvesting from pavements [9]. The modification of bitumen by polymers expands the temperature range for which a bitumen is viable. For example, the addition of specific polymers add reinforcement that can help to prevent permanent deformations (rutting) of the pavement at high temperatures. If instead of a polymer-modified soft bitumen, a hard grade bitumen would be used to prevent rutting at high temperatures the hard bitumen becomes brittle at low temperatures which leads to cracking of the pavement. To reduce the environmental impact of the

pavement the virgin polymer can be replaced by a waste polymer, for example from plastic bottles or tires [10,11]. A further method to reduce the environmental impact of pavement is to recycle the pavement itself, by grinding up the old pavement and re-using it as a material called reclaimed asphalt pavement (RAP) [7]. Since the bitumen in recycled pavement is subject to ageing, which hardens the bitumen, virgin bitumen is added to the recycled pavement before re-use. However, adding virgin bitumen negatively affects the environmental impact of pavement recycling and is also costly. A different approach is to soften the aged bitumen by adding rejuvenators to the recycled pavement [12]. Fiber reinforcement serves a similar purpose as polymer modifications in that it can be used to increase the rutting resistance of the pavement. For this method steel, glass, or polymer fibers are compounded with aggregates and bitumen to produce a pavement material with a longer service life than conventional asphalt concrete. The service life can also be improved by incorporating rejuvenator capsules into the material [8]. When an aged pavement cracks under stress the capsules break open, releasing the rejuvenator into the pavement and closing the cracks. In doing so, the capsules give the pavement self-healing capabilities.

This non-exhaustive review, on the research into improving asphalt concrete, shows that research has focused mostly on improving the bitumen phase, while the aggregate phase has not been modified. A reason for the lack of research on aggregates might be the abundance of viable aggregate material, e.g. limestone, in developed countries such as Switzerland, the European Union and the United States of America. Globally however, viable aggregate materials are less abundant and becoming sparse, a problem which is also

highlighted by a 2014 report of the United Nations Environment Programme (UNEP) [2].

1.2 Artificial aggregates

To address the scarcity of viable aggregate materials, some researchers have investigated the replacement of virgin crushed rock aggregates by other (waste) materials [13–15]. Among the investigated materials are polymers [13,16,17], ash from municipal solid waste incineration (MSWI) [18,19], blast furnace slag [14,20,21] and even seashells [15] or palm oil clinker [22]. Zoorob & Suprama have replaced 30 vol.-% of the aggregates in asphalt concrete with low density polyethylene (LDPE) polymer pellets, creating a material termed Plastiphalt [13]. They report that the Plastiphalt has superior mechanical properties compared to the control containing only mineral aggregates. Another study investigated cross-linked polyethylene (XLPE) waste polymer obtained by shredding cable insulation and found that replacing more than 5 vol.-% of aggregates in roller compacted concrete pavement leads to a loss of the materials strength [17]. MSWI ash frequently finds application in construction materials such as asphalt concrete, since deposing of the ash is costly as it is classified as hazardous waste. The idea is that the bitumen encapsulates the MSWI ash and prevents hazardous contents such as heavy metals from leaching into the environment. This practices however has been criticized by some researchers who termed the construction of roads with such waste materials "linear landfilling" [23]. Nevertheless, one study found that replacing 15 wt.-% and 20 wt.-% of aggregates with MSWI ash sieved to be smaller than 4.75 mm yields a material that satisfies the Marshal test requirements for a road surface course [18]. Heavy metal leaching is also a problem for blast furnace slag used in asphalt pavements, however it was found that aggregates of

3

crushed copper slag can be used to control the resilient modulus value of asphalt mixtures with RAP owing to the shape of the crushed slag aggregates [14]. Beneficial aggregate shapes were also obtained for crushed steel slag, whereby the slag aggregates were used to replace coarse limestone aggregates in a hot mix asphalt [21]. The study found that replacing 39 vol.-% and 62 vol-% of the coarse aggregates leads to improved mechanical properties of the mixture, replacing 100% of the coarse aggregates however decreases the indirect tensile strength and the resistance to moisture damage. Two recent studies have investigated aggregates derived from organic waste, namely crushed seashells of Peruvian Scallops and crushed palm oil kernels [15,22]. The results show that crushed palm oil kernels can replace up to 100% of the fine aggregate in stone mastic asphalt, while maintaining the Marshall mix design requirements. Tests with crushed seashells show that replacing 30 wt.-% of the aggregates size 0.3–2.36 mm reduces the Marshall stability of the mixture, however replacing 4 wt.-% of the fine aggregates with crushed seashells can reduce the permanent deformation of mixtures, due to the angular shape of the aggregates.

While some of these studies on aggregate replacements have controlled the aggregate size by crushing and sieving, which are also done for common (limestone) aggregates, in none of these studies the aggregate shape was explicitly designed. Even though the results of some of the studies indicate that the aggregate shape, rather than the material are what influences the asphalt performance. A further type of study has investigated the manufacturing of artificial aggregates from waste materials such as slag and fly ash, which gives some control over the aggregate shape, these artificial aggregates however have not been considered as aggregates for pavements

but instead for concrete [24,25]. Two different approaches for the manufacturing of artificial aggregates can be distinguished, which are cold-bonding using cementitious materials [26,27] and sintering at high temperatures [28,29].

Two studies by Cioffi et al. [30] and Colangelo and Cioffi [24], which investigated the cold-bonding of MSWI bottom ash as well as cement kiln dust, slag and marble sludge, produced lightweight artificial aggregates that satisfy the technical requirements for structural use in Italy [24,30]. Lightweight aggregates which could be used in concrete preparation were also produced in a further study from red mud and fly ash [31]. In all of these studies on cold-bonding, the aggregates are granulated from waste powder using a rotating pelletizer. The rotating pelletizer process, however, yields nearly spherical aggregates, while the only shape parameters that can be varied are the size of the aggregates and the surface asperity, as confirmed in a review on the cold-bonding of artificial aggregates [27]. Therefore, cold-bonding of artificial aggregates leaves little flexibility for the design of the aggregate shape. While spherical aggregate shapes are desired for concrete made with portland cement, asphalt concrete requires angular aggregates to reduce the permanent deformation of pavements.

High temperature sintering has been investigated for waste materials such as MSWI fly ash [28] and MSWI bottom ash [29]. It has been found that sintering produces lightweight aggregates with sufficiently high compressive strength for building applications [28,29]. For high temperature sintering, the waste material powder is first pressed into an intermediate specimen, typically of cylindrical shape, which are subsequently sintered at up to 1000°C [32]. This process gives

more control over the aggregate shape than rotating pelletization used for cold-bonding. Yet, the intermediate specimens are very fragile which require the shapes to be convex, e.g. cubes or cylinders, while non-convex shapes such as stars or tetrapods are infeasible. Non-convex aggregate shapes however have the potential (i) to improve the strength of certain types of asphalt with aggregate-aggregate interlocking for instance for stone mastic asphalt or porous asphalt, (ii) to increase the porosity of permeable asphalt pavements and (iii) to unlock novel applications such as energy harvesting from pavements. Such non-convex aggregate shapes have thus far not been investigated for the use in asphalt pavements, which is hence the topic of this dissertation.

To this end, a major question to be addressed is how the aggregate shape influences the bulk-structure formed by the pouring (and compressing) aggregates. This question is also an open field of research in soft condensed matter physics, where aggregates are typically called particles and the bulk-structure of poured (and compressed) particles is called a packing.

1.3 Particle packings

1.3.1 Spheres

Arguably the most basic particle shape is the sphere. For packings of equal spheres two different packing configurations, viz. face-centered-cubic and hexagonal close packing, are known to yield the closest possible packing configuration with a packing density $\varphi = \frac{\pi}{3\sqrt{2}} \approx 0.7405$. These closest possible packing configurations have been conjectured by Kepler in 1611 and yet a formal proof of the conjecture was only accepted in 2017 [33]. This 406 year long duration for

establishing a formal proof of the densest possible sphere packing hints towards the complexity of studying particle packings. A further sign is that for ellipsoids, which differ ever so slightly from spheres, no densest possible packing configuration is known yet. Fortunately, the closest possible packing configurations are uncommon in nature and industry, as granular materials only attain these configurations under particular circumstances, for example due to the combined compression and shearing of monodisperse (equally sized) spheres [34] or the oscillatory shearing of cubes [35]. More often, the packings encountered in nature and industry are in a random configuration.

The packing formed by pouring spheres into a vibrated container is often called the random close packing (RCP) and is often quoted with a packing density of $\varphi \approx 0.64$ [36]. However, if the sphere packing is not agitated by vibration, packing densities of $\varphi \approx 0.6$ and less can be found [37]. In fact it has been argued by Torquato et al. [38] that the RCP is ill-defined and that the packing density of spheres increases monotonically with increasing order, until the closest possible configuration is reached. Torquato et al. [38] further argue that instead of a RCP one should define a maximally random jammed (MRJ) packing, whereby a jammed packing is defined as a packing in which no particle can be moved without any displacement of other particles. A different definition of jamming is that of a packing which can transmit a load without the rearrangement of the particles [39]. This second definition makes it evident that jamming is essential for an aggregate packing used in construction applications.

1.3.2 Ellipsoids

Turning now to non-spherical particles this literature review will first focus on ellipsoids, since they are an affine transformation of spheres. Some of the most important works on ellipsoid packings have been reported by Donev et al. [40–42]. In their seminal work [40], they found that the densest lattice packing of ellipsoids has the same packing density as the densest sphere packing ($\varphi \approx 0.7405$), which can be derived analytically, utilizing that ellipsoids are an affine transformation of spheres. However, in the same work they reported even denser non-lattice periodic packings for prolate ellipsoids (American-football shaped) with aspect ratios (α_{elli}) exceeding $\sqrt{3}$ and for oblate ellipsoids (lentil shaped) with $\alpha_{elli} < 1/\sqrt{3}$, where $\alpha_{elli} = b/a$ and a,b and c ($b = c$) are the lengths of the ellipsoids' semi-axes. These crystalline non-lattice packings are composed of periodically replicated unit cells of multiple particles, contrary to lattice packings where the unit cell consists of single particles. For these crystalline packings Donev et al. [40] have found a packing density of $\varphi = 0.7707$ but did not claim that this density is the densest possible ellipsoid packing. For disordered packings Donev et al. [41] have observed that the packing density varies with α_{elli}, displaying an M-shaped curve with a (local) minimum with $\varphi \approx 0.64$ at $\alpha_{elli} = 1$ (spheres) and two peaks, both with $\varphi \approx 0.71$, at $\alpha_{elli} = 0.6$ and $\alpha_{elli} = 1.5$. This M-shaped curve has been confirmed by multiple follow-up studies [37,43–45], which found that the packing density value at the peaks varies slightly with the packing protocol ($0.68 \leq \varphi \leq 0.72$), the peak positions ($\alpha_{elli} = 0.6$ and $\alpha_{elli} = 1.5$) however are unaffected by the packing protocol.

1.3.3 Superquadric particles

In numerical works, the surface of ellipsoidal particles is often modelled using the superquadric equation, because the contact detection between such particles can be solved numerically efficiently [46]. While the superquadric equation can be formulated more generally [47], the most common formulation found in particle simulations is that for superellipsoids:

$$f(x, y, z) =$$
$$\left(\left(\frac{x}{a}\right)^{2/n_2} + \left(\frac{y}{b}\right)^{2/n_2} \right)^{n_2/n_1} + \left(\frac{z}{c}\right)^{2/n_1} - 1 \qquad (1.1)$$

In Eq. (1.1) a, b and c are the half-lengths of the particle along its principal axes (equal to the ellipsoid semi-axes) and the parameters n_1 and n_2 determine the so-called blockiness of the particles, whereby the particles gain sharper corners, i.e. the blockiness increases, for n_1 and n_2 decreasing from 1 to 0, or for n_1 and n_2 increasing from 1 to ∞. In practice the values for n_1 and n_2 are typically limited to $n_1 < 2$ and $n_2 < 2$, which yields convex particles, due to limitations of the contact detection algorithm [46]. The shapes that can be represented include spheres ($a=b=c$ and $n_1=n_2=1$), ellipsoids ($a\neq b$ and $n_1=n_2=1$), cubes ($a=b=c$ and $n_1=n_2<1$), cylinders ($a=b$, $n_1<1$ and $n_2=1$), octahedra ($a=b=c$ and $n_1=n_2=2$) and the Steinmetz solid ($a=b=c$, $n_1=1$ and $n_2=0$).

Delaney & Cleary [43] have published some of the earliest work on random packings of superquadric particles. They varied the aspect ratio ($\alpha_{elli}=a/b$) and blockiness ($0.4 < n_1 < 1.0$) while keeping $n_1 = n_2$. For low blockiness values ($n_1 = n_2 =1$) and varying α_{elli} they recover the M-shaped φ-α_{elli}-curve for oblate and prolate ellipsoids, the results are reproduced in Figure 1. It was further found that for increasing blockiness

values (i.e. decreasing n_1 and n_2) φ increases, because the particle faces become more and more planar, leading to face-to-face alignments of neighboring particles and leading in turn to an increase in φ. Their results show that the φ-α_{elli}-curves are equidistant for $\alpha_{elli} < 0.6$ and $\alpha_{elli} > 1.5$. Specifically, for $\alpha_{elli} = 0.5$ and $n_1 = n_2 = 1$ they find $\varphi \approx 0.70$ while for the same aspect ratio and $n_1 = n_2 = 0.4$ they find $\varphi \approx 0.76$, similarly, for $\alpha_{elli} = 3$ and $n_1 = n_2 = 1$ $\varphi \approx 0.66$, and for $n_1 = n_2 = 0.4$ and $\alpha_{elli} = 3$ $\varphi \approx 0.72$. For $0.6 < \alpha_{elli} < 1.5$ however the increase of φ with decreasing n_1 and n_2 is higher compared to increase of φ with decreasing n_1 and n_2 for $\alpha_{elli} < 0.6$ and $\alpha_{elli} > 1.5$. Additionally, for $0.6 < \alpha_{elli} < 1.5$ the rate of this increase with decreasing n_1 and n_2 increases the closer α_{elli} is to 1 (spheres/cubes). So, while for $n_1 = n_2 = 0.67$ one still observes a flattened M-shaped φ-α_{elli}-curve, the local minimum at $\alpha_{elli} = 1$ cannot be observed for $n_1 = n_2 = 0.5$. When increasing the blockiness of cubes further, i.e. $n_1 = n_2 = 0.4$, one even observes a distinct local maximum at $\alpha_{elli} = 1$ with $\varphi \approx 0.82$. The rate with which φ increases with increasing blockiness is higher the closer α_{elli} is to 1 because of the large planar surfaces of cubes which favors a face-to-face alignment of particles. Compared to cubes ($\alpha_{elli} = 1$), the planar faces of cuboids ($\alpha_{elli} \neq 1$) are smaller and therefore a face-to-face alignment is less likely. The results of Delaney & Cleary [43] have been reproduced by multiple follow-up studies [45,48–50] and Zhao et al. [45] have additionally investigated particles with $n_1 > 1$ and $n_2 > 1$ ($0.4 < n_1 = n2 < 1.4$), for which a sphere transforms into an octahedron instead of a cube. For such shaped particles, when increasing the blockiness by increasing n_1 and n_2 from 1 to 1.4 similar results are obtained as for increasing the blockiness from $n_1 = n_2 = 1$ to $n_1 = n_2 = 0.4$, i.e. φ increases with increasing blockiness and the rate of the increase is higher the closer α_{elli} is to one. However, this correlation of increasing φ with increasing blockiness (for $1 <$

$n_1 = n_2 < 1.4$) is only observable for $0.5 < \alpha_{elli} < 1.5$, while outside of this range no clear correlation between particle blockiness and φ can be identified.
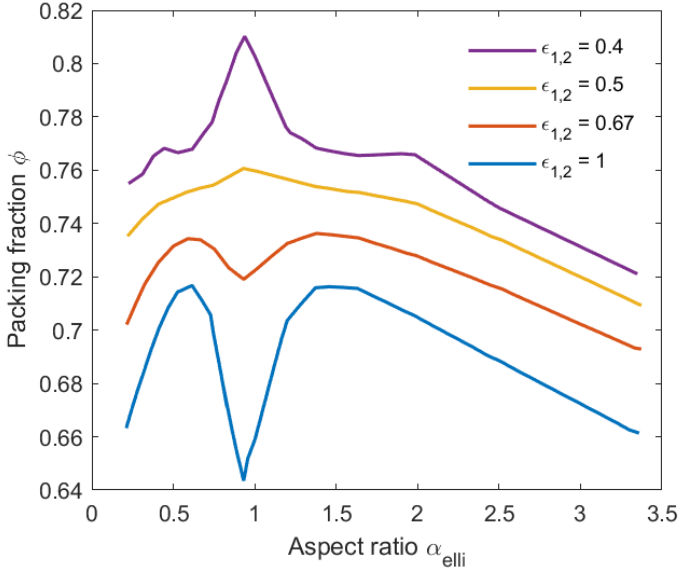
Figure 1: Packing fraction as a function of aspect ratio of superquadric particles. This data is reproduced from Delaney & Cleary [43].

1.3.4 Spherocylinders

Visually similar to prolate ellipsoids are spherocylinders which consists of a cylinder with hemispherically-capped ends. Spherocylinders of different shape are usually distinguished by their aspect ratio α_{scyl} which is defined as the length of the spherocylinder divided by its diameter. An important early work on random spherocylinder packings was reported by

Williams & Philipse [51] who already identified the most striking features of their φ-α_{scyl}-curve, which are a peak at α_{scyl} = 1.5 with $\varphi = 0.70$ and a monotonic decrease for $\alpha_{scyl} > 1.5$. They further found that the packing density of spherocylinders reaches an asymptotic value of $\varphi \approx 0.05$ for $\alpha_{scyl} \geq 80$. The shape of the φ-α_{scyl}-curve with a peak at $\alpha_{scyl} = 1.5$ has since been confirmed in multiple further studies [37,52,53]. However, the maximum packing density of spherocylinders has varied on the packing protocol ($0.65 \leq \varphi \leq 0.72$). Overall, the packing density versus aspect ratio curve is similar for spherocylinders and prolate ellipsoids.

As the number of particle shapes is infinite, a plethora of other convex particle shapes have been investigated, for example tetrahedra [54–56], other polyhedral [57] or natural shapes such as rice [58] crushed rock [59]. These shapes will not be discussed in detail here. Instead, in the following a different group of particles will be discussed, namely non-convex particles.

1.3.5 Non-convex particles

The convexity of particles could be quantified, for example by defining the convexity as the volume of a particle divided by the volume of its convex hull. However, in the following no rigorous definition for the convexity will be considered and instead the particles in this group share visual similarities, for example that they are constructed by intersecting multiple (sphero-)cylinders. Nevertheless, if the convexity of such particles would be quantified, the values for the convexity would undoubtedly differ significantly from the values obtained for particles such as spheres, ellipsoids, or cubes.

While later studies often use spherocylinders to model non-convex particles, in an early numerical study by Malinouskaya et al. [60] a sphere was crossed by equally sized ellipsoids to create "spiky" particles. They created different particles using 3, 4 or 6 ellipsoids, with the center of each ellipsoid being congruent with the center of the central sphere and using equal angles between every ellipsoid. By varying the aspect ratio of the ellipsoids, the particles changed their shape from a sphere with bumps to "spiky stars" with a barely visible sphere. The particle shapes are characterized by their sphericity Ψ, defined as the surface area of a volume equivalent sphere divided by the surface area of the particle itself. For $\Psi = 1$ (spheres) $\varphi = 0.64$ as expected, and for decreasing Ψ the packing fraction decreases almost linearly, reaching a very low packing fraction of $\varphi = 0.08$ at $\Psi = 0.4$. Interestingly the different particle types, which are constructed using 3, 4 and 6 ellipsoids show congruent φ-Ψ-curves.

Gravish et al. [61] experimentally investigated packings of paper staples which they referred to as U-shaped particles and complemented these experiments with numerical simulations in which the staples were assembled from three connected spherocylinders of equal diameter. The central spherocylinder of the U-shaped particles has an aspect ratio (length/diameter) of $\alpha_{scyl} = 14$, while the aspect ratio of the outer arms $\alpha_{scyl,o}$ was varied ($1 \leq \alpha_{scyl,o} \leq 14$) such that it matched the staples. By increasing $\alpha_{scyl,o}$ the sphericity of the particles decreases from $\Psi = 0.52$ to $\Psi = 0.38$ and the packing fraction (vibrated during packing) decreased from $\varphi = 0.28$ to $\varphi = 0.08$. This observation confirmed the finding that the packing fraction decreases with decreasing particle sphericity, which was previously also shown by Malinouskaya et al. [60]. The numerical results of Gravish et al. [61] are matched well by the experimental data

using staples. An interesting feature of the U-shaped particles with long arms is that they entangle and therefore can be used to construct packings in a cylindrical container which do not collapse when the confining cylinder is removed.

The entangling of non-convex particles was also investigated by Murphy et al. [62] for three different particle shapes, each made from three spherocylinders: (1) U-shaped particles similar to the ones of Gravish et al. [61], (2) Z-shaped particles for which one of the outer arms of the U-shaped particles is rotated by 180° around its attachment point to the central spherocylinder, such that the arm points to the opposite direction of the other arm and (3) a particle shape termed Z_{90} for which one of the arms is rotated by 90° compared to the U-shaped particles such that it points upwards. For all of these particle shapes the central spherocylinder is of $\alpha_{scyl} = 12$ and the two outer spherocylinders are of $\alpha_{scyl} = 6$ (therefore all shapes have the same sphericity $\Psi = 0.45$). To investigate the entangling properties of the particles a three-point bending test on unconfined horizontal packing columns was performed. It was found that the Z_{90}-shaped particles performs best, possibly because they are truly three-dimensional which leads to a stronger entangling, whereas the U- and Z-shaped particles are planar. Regarding the packing fraction it was found that the Z-shaped particles had a packing fraction of $\varphi = 0.26$, while for the U- and Z_{90}-shaped particles $\varphi = 0.22$ was found.

In an entirely experimental study Athanassiadis et al. [63] investigated different particle shapes manufactured using 3D printing, which included also non-convex, star-shaped particles (also called jacks). These star-shaped particles are formed by three (sphero-)cylinders, that are all perpendicular to each other, with congruent centers of gravity. The aspect ratio of the

spherocylinders was varied such that the particles have sphericities of $\Psi = 0.87$, $\Psi = 0.81$, $\Psi = 0.67$ and $\Psi = 0.61$. Packings of these star-shaped particles were found to have packing densities of, respectively, $\varphi = 0.54$, $\varphi = 0.52$, $\varphi = 0.46$ and $\varphi = 0.39$, confirming experimentally the finding that that packing fraction decreases with decreasing particle sphericity.

These star-shaped particles, constructed from three intersecting spherocylinders, have also been investigated further in a numerical study by Meng et al. [64]. Here, α_{scyl} was varied from 2 to 11 ($\Psi = 0.86$ to $\Psi = 0.42$) yielding packing fractions decreasing from $\varphi = 0.69$ to $\varphi = 0.28$. Hence, Meng et al. [64] confirmed the monotonic decrease of φ with decreasing Ψ for star-shaped particles as observed by Athanassiadis et al. [63], yet overall higher values for φ were reported. In a follow up study Meng et al. [65] investigated the φ-Ψ-correlations of a variety of particle shapes, including the U- and Z-shaped particles. Unfortunately, only low aspect ratios were modelled. Owing to this limitation, their results for U- and Z-shaped particles cannot be compared quantitatively to the results of the previous studies by Gravish et al. [61] and Murphy et al. [62], respectively. However, qualitatively Meng et al. [65] observed higher packing fractions as expected. A more quantitative comparison is possible with the work of Meng et al. [66], in which star- and Z_{90}-shaped particles, among others, were investigated. Also Meng et al. [66] observed that for $3 \leq \alpha_{scyl} \leq 11$ φ decreases monotonically with increasing α_{scyl} and found that the φ-α_{scyl} curves for all of the investigated particle shapes are congruent. For the Z_{90}-shaped particles with $\Psi = 0.45$ $\varphi = 0.3$, i.e. a value that is higher than the $\varphi = 0.22$ found by Murphy et al. [62] for particles Z_{90}-shaped particles with $\Psi = 0.45$. However, the Z_{90}-shaped particles used in these two studies are not exactly identical, since Meng et al. [66]

15

construct their particles from three spherocylinders of the same length, whereas Murphy et al. [62] construct their particles from spherocylinders with shortened outer arms. An overview of the packing densities found for various particle shapes is shown in Figure 2.

The above literature review leads to the conclusion that for non-convex particles φ generally decreases with decreasing Ψ for Ψ < 0.87. For 1 < Ψ < 0.87 however the φ-Ψ-correlation is not well established and requires more research. Further research is also required to explore how the low φ obtained for low Ψ affects other properties of a packing, such as its structural stability or the transport properties of a fluid in its pore space.
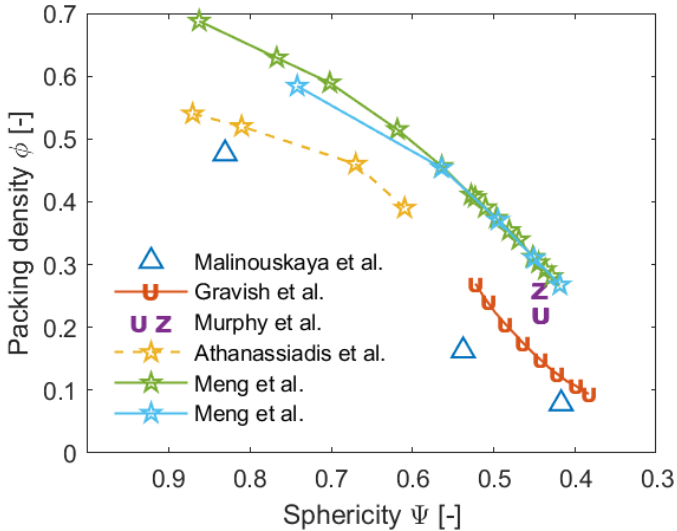

Figure 2: Overview of packing densities for a variety of particle shapes reported in literature: Malinouskaya et al. [60] (spiky particles); Gravish et al. [61] (staples/U-shaped particles); Murphy

et al. [62] *(U- and Z-shaped particles); Athanassiadis et al.* [63] *(stars); Meng et al.* [64] *and Meng et al.* [66] *(stars).*

1.4 Jamming of particle packings

The author of this dissertation considers every particle packing as jammed, because of the previously described definition, that defines any packing as jammed that can transmit a load without any particle rearrangement. If an accumulation of particles is not stable in the presence of gravity, it has to be in the process of rearrangement, i.e. shifting or flowing, and therefore cannot be a packing. Once the flowing accumulation of particles reaches a stable state it returns to being a packing. A good summary of more rigorous definitions of jamming is given by Donev et al. [67] who write: "*Kinematic*. A packing is jammed if none of the particles can be displaced in a nontrivial way without introducing overlap between some particles.

Static. A packing is rigid if it can resolve any externally applied forces through interparticle ones, without changing the packing configuration.

Perturbation. A packing is stable if the structure of the packing changes smoothly for small perturbations of the packing."

These definitions detail the requirements for jamming of an entire packing. The question of how jamming affects the interactions on a particle-to-particle level, however, remains an active field of research. The following paragraphs will not go into detail on all aspects of this field of research, but instead will provide an overview on which an interested reader can base further inquiries.

One aspect pertains to the idea that a jammed packing which transmits loads should be in mechanical equilibrium. Mechanical equilibrium places constraints on the force and torque balance for each particle, requiring D equations for the force balance and $D(D-1)/2$ equations for the torque balance, where D is the dimensionality of the system and the unknowns in the equation are the contact forces [39]. Since a contact force acts between two particles, a system of N particles has $z_{avg}N/2$ contact forces, where z_{avg} is the average number of contacts of a particle. Consequently, a three-dimensional system of frictional particles requires $z \geq 12$ to be able to solve the equation system describing mechanical equilibrium. If $z = 12$ the system is considered to be isostatic, if $z < 12$ the system is called underconstrained or hypostatic and if $z > 12$ the system is called hyperstatic. It is generally accepted that packings of spherical particles tend to pack isostatically [68,69]. For non-spherical particles however no consensus has been reached yet. For example, multiple studies have found packings of ellipsoids to be hypostatic [67,70], but another study has found packings of tetrahedra to be hyperstatic [71].

Another aspect to discuss are force chains, which emerge when a jammed packing is subject to a load. In a disordered packing this load is not distributed homogeneously among the particles [72,73]. Instead, a subset of the particles transmits most of the load to the confining walls. This subset of particles resembles a sparse network in the network of contacting particles [74]. Consequently, some authors have proposed methods adapted from network science to describe the topology of force chain networks [75–77]. Yet, to this date, there is no agreement among the scientific community on how to quantify the structure of force chains such that it can be compared to different packings. As an alternative to describing the contact

force network topology, the probability distribution of the contact forces is often discussed in publications [78,79]. A more detailed description of the contact force distributions can be found in chapter 4.2 of this dissertation.

1.5 Motivation

The literature review has shown that viable aggregate materials are becoming globally scarcer. Several studies have investigated the replacement of virgin aggregates, for example by using demolition waste or by manufacturing artificial aggregates from MSWI ash. All of these studies have yielded irregularly shaped aggregates and it has been suggested that the aggregates' shape, rather than the aggregates material, is what determines the performance of a pavement. Simultaneously studies in the area of soft condensed matter physics have shown that packings of non-convex particles can interlock and form highly porous packings. Both of these properties are beneficial for artificial aggregates and have the potential to improve road pavement and to unlock novel applications for pavements.

The present dissertation is an exploratory investigation of the design and properties of complex non-convex aggregate shapes for their potential use in asphalt pavements.

1.6 Structure of this dissertation

Chapter 2 introduces the discrete element method (DEM) which is often used for the numerical modelling of granular systems, such as particle packings. Chapter 2.2 gives a detailed description of a newly developed DEM for the modelling of non-convex particles. This DEM was developed during this dissertation and was used for the numerical studies presented in the subsequent chapters.

In Chapter 3 it is shown how the use of non-convex aggregate shapes can improve the properties of packings. To this end, numerical packings with non-convex particle shapes are generated, which are compared to experimentally constructed packings of polymer aggregates of the same shapes, that have been manufactured via injection molding. Subsequently, these numerical and experimental packings are evaluated regarding their porosity, tortuosity, and water permeability.

Chapter 4 investigates the physics of granular materials and describes how the distribution of the inter-particle contact forces and intra-particle stresses is affected when non-convex particles, with low sphericity, are used to construct a packing that is subject to an external load.

Chapter 5 covers the manufacturing of artificial aggregates by showing that complex aggregate shapes made of ceramics can be manufactured via additive manufacturing using consumer-grade 3D printers.

Finally, chapter 6 summarizes the conclusions of this dissertation and outlines some remaining research challenges. In addition, this chapter points to future research that would help to advance the technology readiness level of non-convex artificial aggregates for the use in road pavements.

2 Development of a discrete element method for non-spherical particles

Some sections of this chapter are also part of chapter 3.4.2, which is intended for subsequent publication as part of:

2.1 The discrete element method (DEM)

The DEM is a simulation method that models discrete elements, here called particles or aggregates, moving freely in space. Originally developed by Cundall & Strack [80] for spherical particles, the DEM has since been extended to model non-spherical particles [81]. To calculate the positions and velocities of the particles their acceleration (linear and rotational) is integrated with respect to time. The acceleration in turn is calculated from Newton's second law of motion based on the collisional and external forces acting on a particle. The method resolves collisions between particles, collisions between particles and walls as well as external forces, such as gravity, acting on the particles.

2.2 The DEM in this work

In the initial phases of the development of artificial aggregates it was decided that one possibly beneficial shape to investigate is the tetrapod shape (see Figure 3a), which is used in coastal protection. Since a simple DEM representation using combined spheres (see Figure 3b) gives an inadequate representation of the tetrapod shape, an effort was made to explore a better suited DEM representation of such highly non-convex geometries. A comprehensive overview on the advances of non-spherical DEM and available techniques and non-spherical particle geometries was written by Lu et al. [81]. The non-spherical particle geometries include ellipsoids, super-quadrics, polygons and other non-geometric particles created from a combination of simpler geometric shapes, such as a tetrapod made from combining spheres shown in Figure 3b. Polygons are arguably the most versatile of these approaches, as they can be used to model any imaginable particle shape. However,

polygons are computationally expensive because contact detection between polygons is non-trivial.

A rather simple particle shape is the so called spherocylinder (see Figure 3c), which is a cylinder with hemispherically capped ends. What makes this shape so simple is that every point on its surface has the same distance from its central axis. Hence, the spherocylinder particle shape was implemented in a new DEM developed within the scope of this work. By combining multiple spherocylinders, a close approximation of a tetrapod shape can be achieved (see Figure 3d), without significantly increasing the computational load. In the following, particles made by combining multiple spherocylinders are also called spherocylinder clusters.
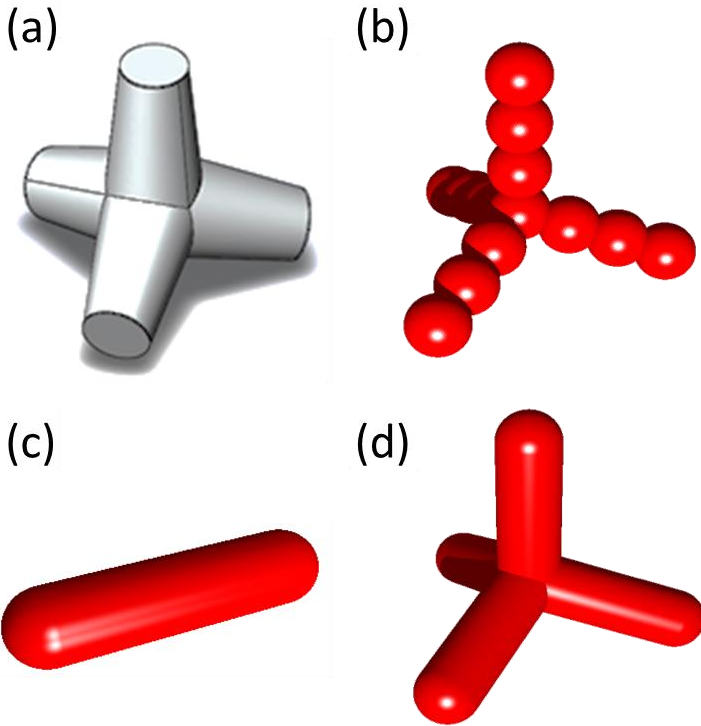
Figure 3: (a) Non-convex tetrapod shape used in coastal protection. (b) Tetrapod made by combining multiple spheres. (c) Spherocylinder particle. (d) Tetrapod particle made by combining four spherocylinders.

The method developed for this work is an extension to the "PONG 3D" DEM framework developed by Dr. Stuart Scott, Dr. Christoph Müller, and Dr. James Third at the University of Cambridge [82]. PONG 3D supports spherical particles, non-spherical particles made from combining multiple spheres as well as infinite planar walls and infinitely long cylinders. Thus,

to construct a closed cylindrical container in PONG 3D an infinitely long cylinder is intersected with two infinite planar walls.

All original elements of PONG 3D are preserved in the framework, all extensions for spherocylinders are added in separate subroutines and functions. This chapter will only describe the modelling of spherocylinders and spherocylinder clusters and where necessary the connection to the original parts of the PONG 3D DEM framework.

2.2.1   Creating a spherocylinder cluster particle

A DEM simulation usually starts by populating the simulation domain with particles, often with random positions and in the case of non-spherical particles with random orientation. In this work the particles are frequently created with a random velocity additional to the random orientation. Creating a spherocylinder cluster particle starts with the creation of the individual spherocylinders that make up the spherocylinder cluster. The major step in creating a spherocylinder is the calculation of the moment of inertia tensor for this particle relative to the global coordinate system. In the body fixed coordinate system (superscript b) where the first axis corresponds to the axis of the spherocylinder the moment of inertia tensor can be calculated geometrically:

$$\bar{\bar{I}}_{i,0}^{b} = \begin{bmatrix} \frac{1}{2}m_{cyl}r_p{}^2 + \frac{4}{5}m_{hemi}r_p{}^2 & 0 & 0 \\ 0 & I_{22} & 0 \\ 0 & 0 & I_{33} \end{bmatrix} \qquad (2.1)$$

With

$$I_{22} = I_{33} = \frac{1}{4} m_{cyl} r_p{}^2 + \frac{1}{12} m_{cyl} l_{cyl}{}^2 +$$

$$2 \left[\frac{83}{120} m_{hemi} r_p{}^2 + m_{hemi} \left(l_{cyl} + \frac{3}{8} r_p \right)^2 \right] \qquad (2.2)$$

In Eq. (2.1) and Eq. (2.2) r_p is the radius of the spherocylinder and l_{cyl} is the length of the cylindrical section of the spherocylinder, i.e. the length of the spherocylinder excluding the hemispherical end caps. m_{cyl} and m_{hemi} are the mass of the cylindrical section of the spherocylinder and a hemispherical end cap, respectively, which are calculate according to:

$$m_{cyl} = \pi l_{cyl} r_p{}^2 \rho \qquad (2.3)$$

and

$$m_{hemi} = \frac{2}{3} \pi r_p{}^3 \rho \qquad (2.4)$$

Here ρ is the density of the spherocylinder.

The next step is to determine the orientation of the spherocylinder relative to the global coordinate system for which the present work employs quaternions, which are also used in the original PONG 3D framework. Quaternions can be thought of as vector, with one real and three complex elements, that can be used to encode rotations:

$$q_0 + q_1 i + q_2 j + q_3 k \qquad (2.5)$$

While Euler angles may provide a conceptually simpler approach to compute rotations, compared to quaternions, they have limitations. The limitations arise from the fact that the rotation matrix based on Euler angles has singularities, a problem also known as gimbal lock. Determining the

orientation of the randomly oriented particle relative to the global coordinate system can be executed via two approaches; Either rotating the quaternion which describes the orientation of the particle relative to the global coordinate system to describe the random initial orientation of the particle, or rotating the body fixed moment of inertia tensor such that the body fixed coordinate system is initially congruent with the global coordinate system. The present work employs the second approach and rotates the moment of inertia tensor such that it is congruent with the global coordinate system and consequently also with the quaternion (1,0,0,0). To rotate the moment of inertia tensor one needs to construct the rotation matrix $\bar{\bar{A}}^{b \to g}$, where the superscript g denotes the global coordinate system. Since a rotation matrix is a linear map, it is known that columns of the rotation matrix are given by the unit vectors that span the body fixed coordinate system, but expressed in the global coordinate system:

$$\bar{\bar{A}}^{b \to g} = \begin{bmatrix} \bar{e}_1^{b \to g} & \bar{e}_2^{b \to g} & \bar{e}_3^{b \to g} \end{bmatrix} \qquad (2.6)$$

The first unit vector corresponds to the central axis of the spherocylinder, because this is how the body fixed coordinate system was defined for the calculation of the body fixed moment of inertia tensor $(\bar{\bar{I}}_{i,0}^b)$. The first unit vector can therefore be calculated by normalizing the vector that corresponds to the central axis of the spherocylinder $(\bar{a}_{cyl})$:

$$\bar{e}_1^{b \to g} = \bar{a}_{cyl}/l_{cyl} \qquad (2.7)$$

Due to the rotational symmetry of a spherocylinder, the second unit vector is any unit vector that is orthogonal to the first unit vector and can be found by computing the cross product ($\otimes$) of the first unit vector with any arbitrary vector. Here we

choose the x-axis of the global coordinate system as the arbitrary vector:

$$\bar{e}_2^{b \to g} = \bar{e}_1^{b \to g} \otimes \begin{bmatrix} 1 \\ 0 \\ 0 \end{bmatrix} \qquad (2.8)$$

A sanity check has to be performed to rule out that the resulting vector is the zero vector, which would happen if the axis of the spherocylinder is collinear with the x-axis of the global coordinate system. If the sanity check fails, one simply has to choose any arbitrary vector that is not collinear with (1,0,0), in the present work the vector (0,1,0) is used. To make $\bar{e}_2^{b \to g}$ a unit vector it has to be normalized by its length. The third unit vector has to be orthogonal to the first two and is computed as:

$$\bar{e}_3^{b \to g} = \bar{e}_1^{b \to g} \otimes \bar{e}_2^{b \to g} \qquad (2.9)$$

and also normalized. Finally, the moment of inertia tensor can be rotated to be congruent with the global coordinate system using the rotation matrix:

$$\bar{\bar{I}}_{i,0}^g = \bar{\bar{A}}^{b \to g} \times \bar{\bar{I}}_{i,0}^b \times \bar{\bar{A}}^{b \to g^\mathrm{T}} \qquad (2.10)$$

Combining spherocylinders to a spherocylinder cluster requires two major steps, viz. computing the center of mass and the combined moment of inertia tensor of the cluster. The center of mass of the cluster ($\bar{x}_{com}$) is calculated according to:

$$\bar{x}_{com} = \frac{1}{\sum_i m_i} \sum_i \bar{x}_{com,i} \, m_i \qquad (2.11)$$

Where the index i refers to all spherocylinders that make up the cluster, $\bar{x}_{com,i}$ is the center of mass of each constituent spherocylinder and m_i the mass of each spherocylinder.

The combined moment of inertia tensor of a spherocylinder cluster can be computed by summing up the moment of inertia tensor of each constituent spherocylinder with the help of Steiner's theorem, which moves the moment of inertia tensor of each constituent spherocylinder into the center of mass of the cluster. For the summation with Steiner's theorem to be valid it has to be computed after the creation of the constituent spherocylinders, such that their moment of inertia tensors are all aligned with the global coordinate system. First, the vector pointing from the center of mass of the cluster ($\bar{x}_{com}$) to the center of mass of each constituent spherocylinder is computed ($\bar{x}_{com,i}$):

$$\bar{s}_i = \bar{x}_{com,i} - \bar{x}_{com} = \begin{bmatrix} s_{1,i} \\ s_{2,i} \\ s_{3,i} \end{bmatrix} \tag{2.12}$$

The combined moment of inertia tensor of the cluster at timestep 0 is congruent with the global coordinate system ($\bar{\bar{I}}^g_{clust,0}$) and is given as:

$$\bar{\bar{I}}^g_{clust,0} = \sum_i \bar{\bar{I}}^g_{i,0} +$$

$$\sum_i m_i \begin{bmatrix} s_{2,i}^2 + s_{3,i}^2 & -s_{1,i}s_{2,i} & -s_{1,i}s_{3,i} \\ -s_{1,i}s_{2,i} & s_{1,i}^2 + s_{3,i}^2 & -s_{2,i}s_{3,i} \\ -s_{1,i}s_{3,i} & -s_{2,i}s_{3,i} & s_{1,i}^2 + s_{2,i}^2 \end{bmatrix} \tag{2.13}$$

For every timestep after the creating of a spherocylinder (cluster) it can no longer be guaranteed that the body fixed coordinate system is congruent with the global coordinate

system and therefore the moment of inertia tensor has to be considered body fixed (superscript *b*).

2.2.2 Searching for particle contacts

Checking for contacts between particles is computationally expensive, independent of the simulated particle shapes and the method used to compute the distance between particles to determine whether the particles are in contact [83]. The reason for the large computational effort is that checking for a contact between all N particles in a simulation requires at maximum N^2 computations of the (overlap-)distance between particles. To reduce the computational effort various methods have been developed to eliminate the need to check for contacts between all particles in a simulation. These methods include grid subdivision, the octree method and linked lists [84,85]. The original PONG 3D framework uses a grid subdivision approach ("boxing"), i.e. the simulation domain is subdivided into boxes and particles are sorted into certain boxes based on their position. Only particles that share a box are then checked for mutual contact, which means the computational effort grows linearly with the number of particles. The extension to spherocylinders also employs the boxing method from the original framework without any changes. Nevertheless, an explanation of the original boxing method for spherical particles is given below.

For the boxing the simulation domain is subdivided into cubic boxes with edges of length B (see Figure 4), which have the same orientation as the global coordinate system. To determine in which box(es) a spherical particle with radius r_p belongs to, an imaginary cube is projected around the particle. This cube is centered on the particle, is aligned with the global coordinate

system and has an edge length $B = 2(r_p + c_{sph})$, where c_{sph} is the so-called contact tolerance for spherical particles. A particle is considered to be part of every box, where one of the vertices of the imaginary cube is positioned in (for a three-dimensional system there are up to eight boxes per particle). The sorting is done based on the vertices of the imaginary cube, since computing the corresponding box of one of the vertices is a computationally efficient problem. Sorting a particle into boxes based on the vertices of its imaginary cube poses puts a limit on the minimal size for the boxes, viz:

$$B > 2(r_p + c_{sph}) \qquad (2.14)$$

If Eq. (2.14) is not considered, the vertices of the imaginary cube around a particle could be in two different boxes, neither of which contains the center point of the particle, which is shown for the particle in Figure 4 that has the contact tolerance c_{wrong}.

31
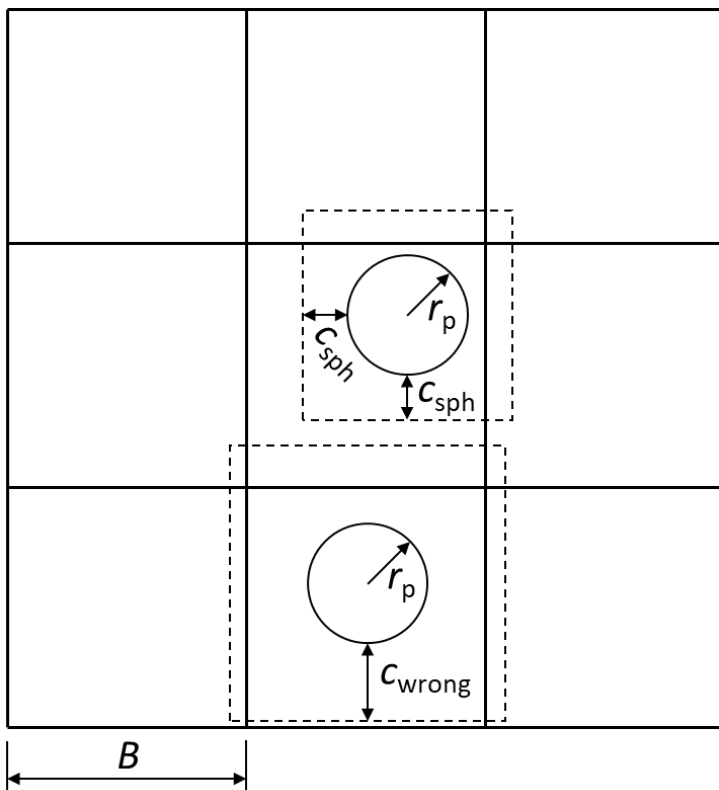
Figure 4: Two-dimensional schematic of the boxing method.

Adding the contact tolerance to the size of the imaginary cube has several computational benefits. First of all, it eliminates an issue that occurs when two particles sit right on the edge of two adjacent boxes and are touching (with zero contact force). These two particles will not be considered for a mutual contact search since both particles are sorted into different boxes. Adding the contact tolerance ensures that these two particles

would be part of the same box(es), even if they are close but not in physical contact (yet). Another computational benefit of adding the contact tolerance to the size of the imaginary cube is that it can be used to reduce the number of boxing operations for a particle, since a particle will note leave its assigned boxes, unless it has moved more than the distance c_{sph}. Consequently, in the present work the boxing operation for a particle is not performed unless a particle has accumulated a displacement of $0.9c_{sph}$. In the PONG 3D framework, particles are checked for contacts with other particles in their boxes immediately after boxing, which can be exploited for yet another computational benefit. The present work considers spherical particles to be in contact when their separation distance is less than $2c_{sph}$, however, no contact forces are acting between the particles unless they are touching. Therefore, if a particle was not touching any particles it can be guaranteed that it will not touch any new particles unless it accumulated a displacement of c_{sph}. Therefore, in the present work the contact search for spherical particles is only started after a particle has been boxed, which only happens once the accumulated displacement is larger $0.9c_{sph}$.

The boxing method described above could be used for spherocylinders without any changes, provided the edge length of the imaginary cube is at least as long as overall length of the spherocylinder (L) plus a contact tolerance. Two equally sized spherocylinders would then be considered in contact (but not touching) if their centers are separated by less than L plus a contact tolerance. According to Eq. (2.14) this would also require large enough boxes, which for granular systems of low density would be largely empty or for granular systems of high density would contain many particles. This makes the boxing method with large boxes, which are required for high aspect

ratio particles such as long spherocylinders, computationally inefficient. The efficiency can be improved by employing an approach proposed by Guo et al. [86], who suggested to subdivide long particles into smaller elements with lower aspect ratio for initial contact detection based on boxing. In the present work the spherocylinders are approximated by spherical particles for the boxing and initial contact detection. These massless spherical particles are termed virtual spheres, have the same diameter as the spherocylinder, always keep their positions within the spherocylinder particle and do not make contact with each other or other particles in the simulation. A visualization of the virtual spheres inside a spherocylinder is given in Figure 5. The first and last virtual sphere in a spherocylinder are congruent with the hemispherical caps of the spherocylinder, while the rest of the spherocylinder is filled equally spaced with N_{fill} virtual spheres, where

$$N_{fill} = FLOOR\left(\frac{L - 2r_p}{2r_p}\right) \qquad (2.15)$$

The FLOOR function rounds a number down to the nearest integer value. This method of filling a spherocylinder with virtual spheres guarantees that there are no gaps between the virtual spheres inside a spherocylinder.
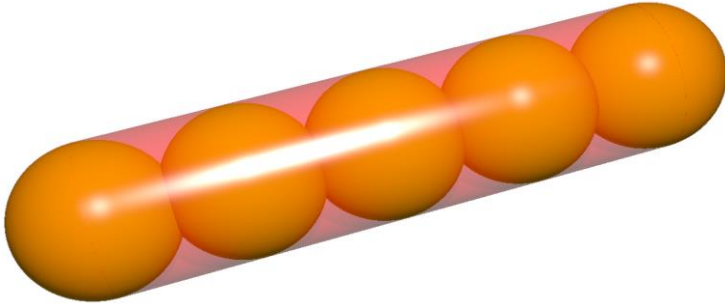
Figure 5: Virtual spheres inside a spherocylinder.

Figure 6a sketches a complication that occurs when using the virtual spheres for the initial contact detection of spherocylinders. If a spherocylinder touches another spherocylinder near the indentation between two virtual spheres, it might not be considered a contact if the contact tolerance for spherical particles c_{sph} is too small. A too small c_{sph} is illustrated in Figure 6a, where the green circle, representing c_{sph} around the first virtual sphere (dashed gray) of the red spherocylinder, does not overlap with any black circles of the blue spherocylinder. Therefore, no contact will be detected, since the separation between any virtual sphere of the red spherocylinder and any virtual sphere of the blue spherocylinder is larger than $2c_{sph}$, although the spherocylinders are touching. The complication outlined above places a lower limit on the contact tolerance for spherical particles c_{sph}. A geometrical representation of this lower limit is shown in Figure 6b, where a separation distance for spherocylinders c_{cyl} is introduced. The two distances a and b in Figure 6b are given as: $a = 2r_p + 2c_{cyl}$ and $b = 2r_p + 2c_{sph.}$ If the requirement for a contact between spherocylinders is a

35

separation distance less than $2c_{cyl}$ then the requirement for c_{sph} is:

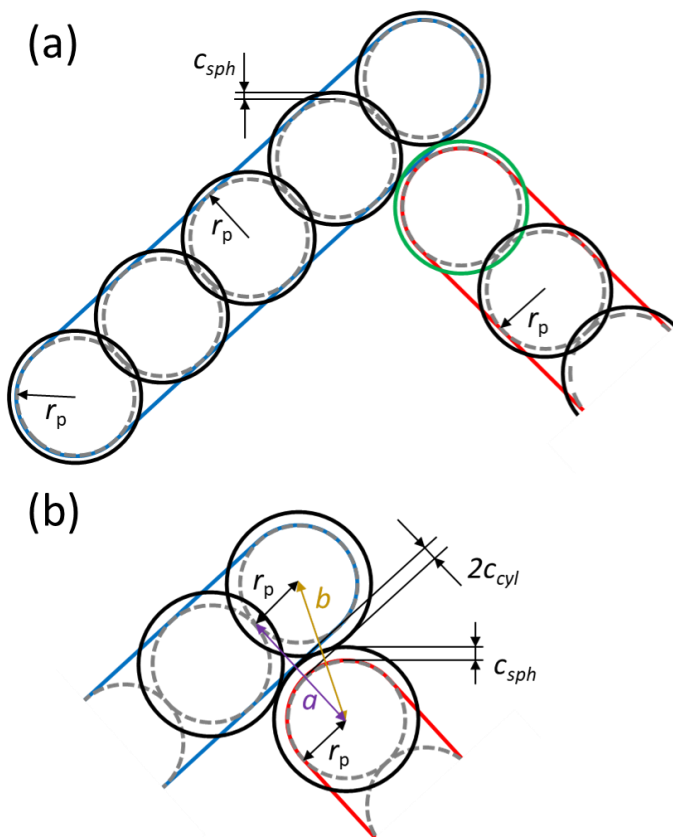$$c_{sph} > \frac{1}{2}\left(\sqrt{r_p{}^2 + \left(c_{cyl} + 2r_p \right)^2} - 2r_p \right) \qquad (2.16)$$

Figure 6: (a) Two spherocylinders are touching but are not recognized as contacting because the contact tolerance for the

spherical particles (c_{sph}) is too small. (b) The contact tolerance c_{sph} for spherical particles has to be chosen large enough such that spherocylinders are recognized as contacting when they are separated by a distance equal to twice the contact tolerance for spherocylinders (c_{cyl}).

Once a contact is found between the virtual spheres of spherocylinders, the two spherocylinders are considered in contact and the separation between the spherocylinders is calculated to determine whether the spherocylinders are touching. The separation between spherocylinders can be calculated by finding the minimal distance between the central axes of the spherocylinders, which in the present framework is done using the algorithm proposed by Lumelsky [87]. If the distance between the two central axes of the spherocylinder is less than the sum of the spherocylinder radii, the spherocylinders are touching. An illustration of spherocylinders in contact is given in Figure 7. The contact point between two spherocylinders is the middle point of the shortest line between the central axes of two contacting spherocylinders. In this contact point act the contact force between the spherocylinders (green arrows in Figure 7). If the central axes of two contacting spherocylinders share a parallel segment, as seen in Figure 7b, there is no single shortest line between the two central axes. In this case the contact point is the middle point of the line which is in the center of the parallel segment.
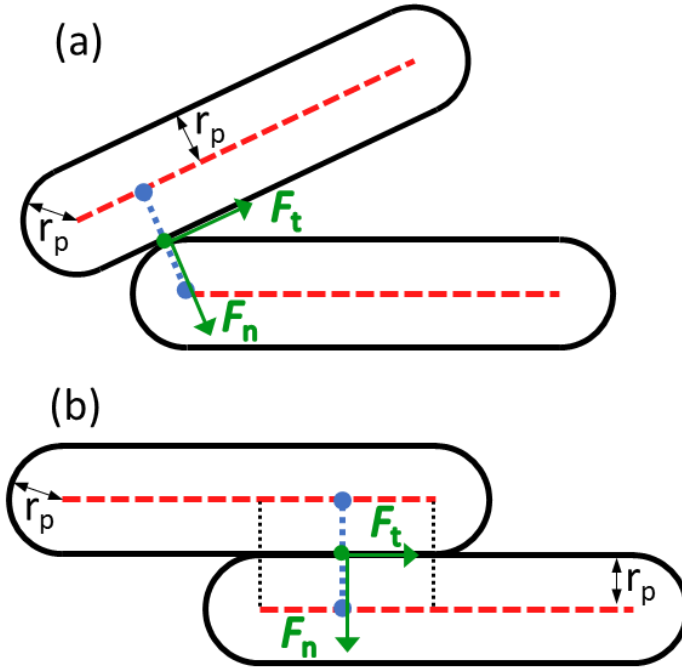
Figure 7: Schematic of two contacting spherocylinders: a) contact between a cylindrical section and a hemispherical end cap, b) parallel contact between spherocylinders. The red dashed lines denote the central axis of each spherocylinder. The blue line depicts the shortest distance between the central axis of the two spherocylinders and the contact point is the green middle point of the blue dotted line.

2.2.3 Contact forces

The contact force models are left unchanged from the original PONG 3D framework and the equations are repeated here for the sake of completeness. In PONG 3D the contact force in the normal direction is modelled by a linear spring-dashpot, i.e. a

Hookean spring. One could argue that a non-linear Hertzian contact model is more appropriate for contacts in granular materials. Other works however have shown that using the more complicated non-linear model over a linear model does not affect the probability distribution of the contact forces in packings of spherocylinders [88]. A benefit of the simpler linear contact model is that it yields a coefficient of restitution that is constant, i.e. independent of the relative velocity of the contacting particles [82]. It has also been argued that the material stiffness should increase with increasing contact area, e.g. in the case of a parallel contact between two spherocylinders (Figure 7b) [89–91]. However, a recent study has shown that varying the contact stiffness in the case of parallel contacts has little influence on the force distribution and the structure in packings of spherocylinders [88]. Consequently, in this work, the normal and tangential stiffness are assumed to be constant, regardless of the geometry of the contact.

To calculate the contact forces between particles the positions of the particles in contact as well as their relative velocity has to be known. From the positions the overlap (δ_n) between the particles is calculated according to:

$$\delta_n = r_{p,i} + r_{p,j} - d_{axes} \qquad (2.17)$$

In Eq. (2.17) $r_{p,i}$ and $r_{p,j}$ are the radii of the contacting spherocylinders $\underline{i}$ and j and d_{axes} is the minimal distance between their central axes. The relative velocity between particles is calculated by considering the translational velocity ($\bar{v}_i$ and $\bar{v}_j$) as well as the rotational velocity for the two contacting spherocylinders ($\bar{\omega}_i$ and $\bar{\omega}_j$):

$$\bar{v}_{rel} = \bar{v}_i - \bar{v}_j + \bar{r}_{i,c} \otimes \bar{\omega}_i - \bar{r}_{j,c} \otimes \bar{\omega}_j \qquad (2.18)$$

$\bar{r}_{i,c}$ and $\bar{r}_{j,c}$ are the vectors pointing from the center of particle i and j, respectively to the contact point. The normal component of the relative velocity is the component of the relative velocity projected onto the normal vector ($\odot$ is the dot product):

$$\bar{v}_n = (\bar{v}_{rel} \odot \bar{n})\bar{n} \qquad (2.19)$$

And the tangential component of the relative velocity can be found by subtracting the normal component from the total relative velocity:

$$\bar{v}_t = \bar{v}_{rel} - \bar{v}_n \qquad (2.20)$$

To find the relative displacement in the tangential direction the relative velocity is integrated over time:

$$\bar{\delta}_t = \int \bar{v}_t \, dt \qquad (2.21)$$

With the information calculated above one can calculate the contact forces. The contact force in in the normal direction between particles i and j is given as:

$$F_n = \max\left(0, \quad \frac{k_n}{2}\delta_n - \eta_n \sqrt{2m_{ij}k_n v_n}\right) \qquad (2.22)$$

Here v_n is the magnitude, i.e. the Euclidian norm, of the normal component of the relative velocity, k_n is the normal stiffness of the particles and η_n is the normal damping factor. The so-called effective mass of the particles in contact m_{ij} is calculated from the mass of the individual particles:

$$m_{ij} = \frac{m_i m_j}{m_i + m_j} \qquad (2.23)$$

This normal contact force can be negative for particles which are in contact but with a negative relative velocity which indicates that the particles are separating from each other. This would yield an unphysical attractive normal contact force which has to be prevented, thus the normal contact force is set to zero if the above calculation yields a negative force.

The contact force in the tangential direction acts in the opposite direction of the relative tangential velocity and is limited in magnitude by Coulomb's friction law:

$$F_t = \min\left(\mu \frac{k_n}{2}\delta_n, \quad \frac{k_t}{2}\delta_t - \eta_t\sqrt{2m_{ij}k_t}v_t\right) \quad (2.24)$$

Here μ is the coefficient of friction, η_t is the tangential damping factor, k_t is the tangential stiffness and v_t is the magnitude of the tangential component of the relative velocity between the particles.

2.2.4 Calculating the acceleration via Newton's third law

Once all contact forces acting on a particle i have been calculated they are summed up and the resulting force $F_{sum,i}$ yields the acceleration of the particle in the next timestep as per Newton's second law of motion:

$$\bar{a}_i(t + \Delta t) = \frac{\bar{F}_{sum,i}}{m_i} \quad (2.25)$$

For non-spherical particles all contact forces also induce a momentum M_i:

$$\bar{M}_i(t + \Delta t) = \sum_c \bar{r}_c \otimes (\bar{F}_{n,c} + \bar{F}_{t,c}) \quad (2.26)$$

where the index c loops over all contacts of particle i and r_c is the vector pointing from the center of gravity of the particle to the contact point.

2.2.5 Updating positions and velocities

The velocity of a particle i is found by the numerical integration of the acceleration $\bar{a}(t)$ acting on the particle:

$$\bar{v}_i(t) = \bar{v}_i(t - \Delta t) +$$
$$\frac{\Delta t}{12}[23\bar{a}_i(t - \Delta t) - 16\bar{a}_i(t - 2\Delta t) + 5\bar{a}_i(t - 3\Delta t)] \quad (2.27)$$

The position is updated in similar fashion:

$$\bar{x}_i(t) = \bar{x}_i(t - \Delta t) +$$
$$\frac{\Delta t}{12}[23\bar{v}_i(t - \Delta t) - 16\bar{v}_i(t - 2\Delta t) + 5\bar{v}_i(t - 3\Delta t)] \quad (2.28)$$

Modelling non-spherical particles additionally necessitates keeping track of the particle orientation, angular velocity $\bar{\omega}(t)$, and angular momentum $\bar{J}(t)$. The angular momentum of particle i at timestep t is found by integrating the net torque $\bar{M}(t)$ acting on the particle due to the off-center forces. For the integration the present framework employs a third order Adams-Bashforth scheme:

$$\bar{J}_i(t) = \bar{J}_i(t - \Delta t) +$$
$$\frac{\Delta t}{12}[23\bar{M}_i(t - \Delta t) - 16\bar{M}_i(t - 2\Delta t) + 5\bar{M}_i(t - 3\Delta t)] \quad (2.29)$$

Subsequently, the quaternion is updated to the current timestep by integrating the past quaternion derivatives:

$$\bar{q}_i(t) = \bar{q}_i(t - \Delta t) +$$

$$\frac{\Delta t}{12}[23\dot{\bar{q}}_i(t - \Delta t) - 16\dot{\bar{q}}_i(t - 2\Delta t) + 5\dot{\bar{q}}_i(t - 3\Delta t)] \quad (2.30)$$

Where:

$$\bar{q}_i(t) = \begin{bmatrix} q_0 \\ q_1 \\ q_2 \\ q_3 \end{bmatrix} \quad (2.31)$$

To find the angular velocity, the angular momentum is divided by the moment of inertia tensor $\bar{\bar{I}}_i^b$ of the particle. As described in section 2.2.1, the moment of inertia tensor is given in the body fixed coordinate system, albeit congruent with the global coordinate system at the timestep of the particle creation. The angular momentum and angular velocity however are in the global coordinate system. Therefore, the moment of inertia tensor needs to be rotated from the body fixed to the global coordinate system for the calculation of the angular velocity. Quaternions are used to construct the rotation matrix from the global to the body fixed coordinate system ($\bar{\bar{A}}^{g \to b}$):

$$\bar{\bar{A}}^{g \to b} = [\bar{A}_1 \quad \bar{A}_2 \quad \bar{A}_3] \quad (2.32a)$$

with:

$$\bar{A}_1 = \begin{bmatrix} q_0{}^2 + q_1{}^2 - q_2{}^2 - q_3{}^2 \\ 2(q_1 q_2 - q_0 q_3) \\ 2(q_1 q_3 + q_0 q_2) \end{bmatrix} \quad (2.32b)$$

$$\bar{A}_2 = \begin{bmatrix} 2(q_1 q_2 + q_0 q_3) \\ q_0{}^2 - q_1{}^2 + q_2{}^2 - q_3{}^2 \\ 2(q_2 q_3 - q_0 q_1) \end{bmatrix} \quad (2.32c)$$

$$\bar{A}_3 = \begin{bmatrix} 2(q_1 q_3 - q_0 q_2) \\ 2(q_2 q_3 + q_0 q_1) \\ q_0{}^2 - q_1{}^2 - q_2{}^2 + q_3{}^2 \end{bmatrix} \qquad (2.32d)$$

The rotation matrix is then used to rotate the angular momentum to the body fixed coordinate system:

$$\bar{J}_i^b(t) = \bar{\bar{A}}^{g \to b} \times \bar{J}_i^g(t) \times \bar{\bar{A}}^{g \to b^T}$$

which can then be used to calculate the angular velocity in the body fixed coordinate system:

$$\bar{\omega}_i^b(t) = \bar{I}_i^{b^{-1}} \times \bar{J}_i^b(t) \qquad (2.33)$$

Finally, the body fixed angular velocity is used to find the quaternion derivative of the current timestep:

$$\dot{\bar{q}}_i(t) = \begin{bmatrix} \dot{q}_1(t) \\ \dot{q}_2(t) \\ \dot{q}_3(t) \\ \dot{q}_4(t) \end{bmatrix} =$$

$$\frac{1}{2} \begin{bmatrix} q_1(t) & -q_2(t) & -q_3(t) & -q_4(t) \\ q_2(t) & q_1(t) & -q_4(t) & q_3(t) \\ q_3(t) & q_4(t) & q_1(t) & -q_2(t) \\ q_4(t) & -q_3(t) & q_2(t) & q_1(t) \end{bmatrix} \begin{bmatrix} 0 \\ \omega_{i,x}^b(t) \\ \omega_{i,y}^b(t) \\ \omega_{i,z}^b(t) \end{bmatrix} \qquad (2.34)$$

3 Effect of artificial aggregate shapes on the porosity, tortuosity, and permeability of their packings

Adapted from:

N.A. Conzelmann, M.N. Partl, F.J. Clemens, C.R. Müller, L.D. Poulikakos, Effect of artificial aggregate shapes on the porosity, tortuosity, and permeability of their packings, Powder Technol. 397 (2022). doi:10.1016/j.powtec.2021.11.063.

3.1 Abstract

Natural aggregates such as gravel are used in many construction applications for which porous structures are needed, for example to allow water drainage. However, the range of attainable porosities is limited due to the irregular shapes of natural aggregates. Here we investigate artificial aggregates of engineered shapes, which allow structures with porosities exceeding 0.7. In this study packings of a variety of artificial aggregate shapes are examined by both numerical and experimental techniques. We can establish a correlation between the porosity of a packing and the sphericity of the aggregates. Furthermore, we confirm that the Carman-Kozeny correlation can be used to predict accurately the permeability of a packing for a wide range of porosities (0.33 – 0.78). Establishment of this basic relationship between the porosity and permeability of a packing is critical for the design of artificial aggregates for novel applications such as energy harvesting from pavements.

3.2 Introduction

Aggregates in the form of sand, gravel or crushed rock are the basis of many construction and building materials such as concrete and asphalt in which the aggregates are compounded with a binder. Other construction applications, such as subsurface drainage systems employ unbound aggregates which are poured or mechanically compacted to form rigid structures [92], so-called aggregate packings [93,94]. One specific application of a bound permeable material is porous asphalt concrete. However, due to the relatively low open porosity ε of $0.15 < \varepsilon < 0.25$ and the relatively small size of its pores, porous asphalt for road pavements is prone to clogging

[95–97]. Increasing the porosity of asphalt concrete would not only reduce the clogging problem but also enable applications such as energy harvesting from roads. To harvest energy from pavements, one approach proposes to embed air filled tubes into the pavement [98]. With increasing pavement temperature, the air expands and drives a turbine to generate electricity. A positive side effect of this technology is the alleviation of urban heat islands in modern cities, through cooling of the pavement [99–101]. However, introducing tubes into the asphalt pavement complicates the recycling of the pavement material. A pavement material that is highly porous and permeable to air and water but does not contain foreign objects such as tubes could enable energy harvesting while retaining its recyclability. Another drawback of porous asphalt with conventional aggregates is that the pavement durability decreases with increasing porosity [102]. The durability could potentially be improved by engineered interlocking aggregates that form a rigid yet porous packing.

An associated challenge is the accurate determination of the water permeability of construction materials that are composed of packings of aggregates. Studies correlating the packing porosity and permeability are thus far limited by the narrow range of porosities that can be achieved with conventional aggregates. The earliest method to determine the permeability of an aggregate packing was proposed by Darcy [103] in 1856 by relating the water flux q through a packing with its permeability k and the pressure gradient $\frac{\partial p}{\partial x}$ over the packing, viz:

$$q = -\frac{k}{v_w \rho_w} \frac{dp}{dx} \qquad (3.1)$$

where v_w and ρ_w are the kinematic viscosity and density of water. However, measuring simultaneously the flux and pressure drop can be challenging. For Reynolds numbers (Re) < 1, an empirical correlation to determine the permeability of a packing based on ε and the aggregate sphericity Ψ and diameter d_p, was proposed by Kozeny in 1927 [104], and later refined by Carman [105,106]:

$$k = \frac{\Psi^2 d_p^2 \varepsilon^3}{150(1-\varepsilon)^2} \qquad (3.2)$$

The original equation of Kozeny incorporates tortuosity τ, a parameter that gives the mean path length of a fluid particle when percolating through the packing. In the revised version of Carman, tortuosity is incorporated in the scaling constant (150) using experimental data. To this day, the validity of the Carman-Kozeny correlation [Eq. (3.2)] has been confirmed by a vast number of studies [107–110]. However, the physical packings studied in these works usually covered only a small range of ε, e.g. for pervious concrete [110] and fiber mats [108] porosities in the range of, respectively, $0.1 < \varepsilon < 0.35$ and $0.5 < \varepsilon < 0.8$ were typically encountered. Other studies have investigated wider ranges of ε, but considered non-physical packings such as randomly placed obstacles [107,111], or fractal geometries [109]. A critical evaluation of the validity of the Carman-Kozeny correlation over a wide range of ε for physical packings is missing thus far.

Above we have outlined two current challenges: (i) the requirement of aggregate packings to accommodate a large porosity to enable novel applications such as energy harvesting from pavements, without reducing their durability, and (ii) the open validation of the Carman-Kozeny correlation for physical packings covering a wide range of ε. Both challenges persist

because current methods for aggregate production yield irregularly shaped aggregates, which in the case of crushed rock and gravel are approximately cubical [112]. The use of irregularly, cubically, shaped aggregates, however, limits the range of attainable packing porosities, as cubes form relatively dense packings compared to other shapes [48,59,63]. Despite the practical importance of aggregates as construction materials, they are commonly used in their "natural state" and their shape is not specifically designed to optimize the aggregate packing for certain properties. Yet, recently a new type of artificial aggregate with engineered shapes, such as stars, tetrapods, and dolosse has been proposed [63,113,114]. Indeed such shapes have been also used in marine engineering to construct breakwaters, since shapes such as tetrapods and dolosse have been shown to form porous yet stable packings [115]. Advances in 3D printing have unlocked the manufacturing capabilities of such artificial aggregates using polymers [113], or even ceramics [116]. Additionally, aggregate shapes can be designed to be geometrically interlocking, enabling freestanding loadbearing structures of unbound aggregates [62,114,117,118]. This loadbearing property makes the construction of unbound building facades possible, for example in urban canyons, allowing the porosity to be optimized for noise absorption in addition to the mitigation of heat islands as discussed above [119]. Simultaneously, however, the interlocking property reduces the compactibility and workability of the material, as evidenced by an increase of the shear strength with decreasing aggregate sphericity [120].

Here we investigate artificial aggregates of different shapes and quantify their packing properties such as porosity, tortuosity, and water permeability, and in doing so assess the validity of

the Carman-Kozeny correlation for physical packings covering a wide range of porosities for $Re = 0.56$. Packings are constructed both experimentally from model polymer aggregates in an unbound configuration and numerically using the discrete element method (DEM). Subsequently, the permeability is computed numerically using the lattice Boltzmann method (LBM) and validated experimentally using the falling pressure head method.

3.3   Materials and Methods

Figure 8 gives an overview of the materials and methods employed in this work which are divided into a numerical and experimental part. In the numerical part, the DEM is used to create packings composed of three different types of non-spherical aggregate shapes, viz. tetrapods, dolosse and tetrahedra (see Figure 9). Since the full 3D geometrical information is known for the packings generated with the DEM, the porosity of these packings can be determined with high accuracy. Computing the tortuosity requires an intermediate step in which the 3D geometric information is converted into binary data sets, that distinguish between aggregate matter and voids and are stored as images that slice the packing horizontally. To compute the permeability of water in a given numerical packing, the geometrical information is converted into a stereolithographic (STL) file which requires triangular tessellation of the aggregate surfaces. Subsequently, the STL file is used to construct the geometry to compute the permeability via LBM simulations.

In the experimental part of this work, aggregates of two different tetrapod shapes are constructed from acrylonitrile butadiene styrene (ABS) polymer via injection molding. These

aggregates are poured into a container to construct packings, which are then used to determine the packing porosity from the weight of water filling the voids. The packings are further used to determine their water permeability via the falling pressure head method. One of the constructed packings, i.e. using tetrapods with sphericity $\Psi = 0.53$, is imaged using X-ray computed tomography (CT) to obtain identical, full 3D geometry information as from the DEM simulations. This experimentally obtained 3D geometry of the packing is used to compute the porosity, tortuosity and permeability of the packing utilizing the same numerical methods as for the DEM packings.
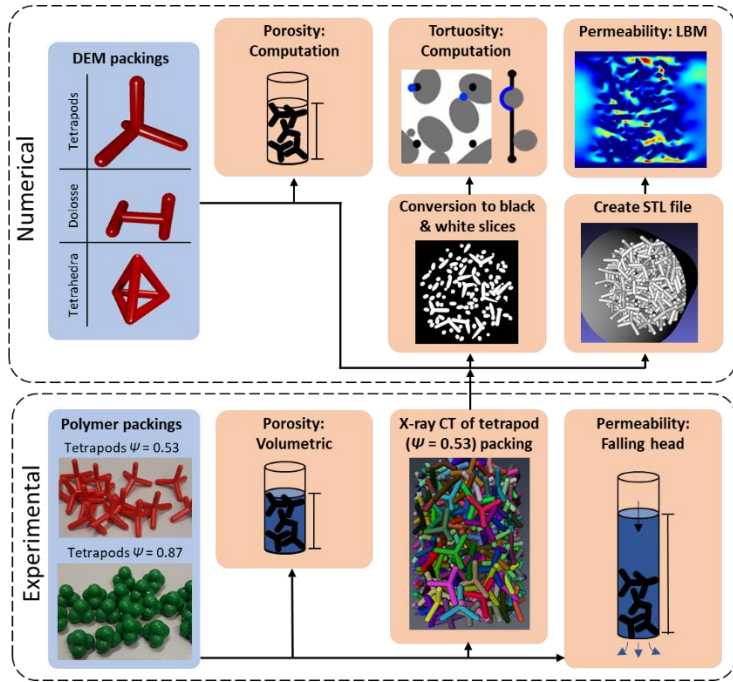
Figure 8: Overview of the materials and methods applied in the numerical and experimental parts.

3.4 Numerical materials and methods

3.4.1 Aggregate shapes

The aggregate shapes studied here are constructed by intersecting identical spherocylinders, i.e. cylinders with hemispherically capped ends. In doing so, three different types of artificial aggregate shapes are constructed, viz. tetrapods, dolosse and tetrahedra. The aggregate shapes are visualized in Figure 9.

A tetrapod is constructed from four spherocylinders, which extend from the center of gravity of a regular tetrahedron to the four vertices of the tetrahedron. The hemispherical endcaps of the spherocylinders in the center of gravity are congruent with a sphere around the center of gravity of the tetrahedron.

Dolosse are constructed by combining three spherocylinders such that they form a H. The base point of each hemispherical endcap of the central spherocylinder lies exactly at the center of the central axis of an outer spherocylinder. To complete a dolos, one of the outer spherocylinders is then rotated by 90° to be perpendicular to the other two spherocylinders.

Tetrahedra are constructed from six spherocylinders each lying on one of the six edges of a tetrahedron. The hemispherical endcaps of the spherocylinders are congruent in the four vertices of the tetrahedron.

For each type of aggregate, a variety of aggregates of varying sphericity (Ψ) are constructed by changing the length and diameter of the constituent spherocylinders. Here the sphericity is defined as the surface area of a sphere with the same volume as the non-spherical aggregate divided by the surface area of the non-spherical aggregate. A visual representation for this is shown in Figure 10, where the sphere (blue) that has the same volume as the red tetrapod. All aggregates considered in this study have the same volume of 733 mm^3. The diameters and aspect ratios of all of the simulated aggregate shapes can be found in the Table 1-Table 3, where the aspect ratio is defined as a spherocylinders length divided by its diameter. An infinite number of aggregate shapes could be constructed by varying the diameters and aspect ratios of the intersecting spherocylinders, which would lead to arbitrarily complex packings. The reason for using identical spherocylinders to

53

construct an aggregate is to reduce complexity. For the same reason, packings are created by using only aggregates of identical type and sphericity.

In addition to sphericity (Ψ), the shape of the aggregates is also described quantitatively by their convexity (Ω). The convexity is defined as the volume of the aggregate divided by the volume of the convex hull enveloping the aggregate. The convex hull is the smallest convex polygon which completely envelopes the aggregate. A more figurative description of the convex hull is this: Imagine wrapping an aggregate with a cloth and pulling the cloth as tight as possible. The cloth will then have the same shape as the convex hull. A visualization of the convex hull for a tetrapod with $\Psi = 0.53$ (AR = 3.5) is shown in Figure 11. Coincidentally, the convex hull for all of the three aggregate types investigated here, viz. tetrapods, dolosse and tetrahedra takes the shape of a tetrahedron, albeit an irregular-shaped tetrahedron for dolosse.
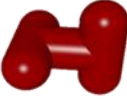
Tetrapods		Dolosse		Tetrahedra	
$\Psi = 0.87$	$\Omega = 0.86$	$\Psi = 0.85$	$\Omega = 0.86$	$\Psi = 0.97$	$\Omega = 1$
$\Psi = 0.67$	$\Omega = 0.47$	$\Psi = 0.73$	$\Omega = 0.65$	$\Psi = 0.74$	$\Omega = 0.93$
$\Psi = 0.53$	$\Omega = 0.19$	$\Psi = 0.55$	$\Omega = 0.28$	$\Psi = 0.43$	$\Omega = 0.40$

Figure 9: The different artificial aggregate types and aggregate sphericities that are investigated in this work.
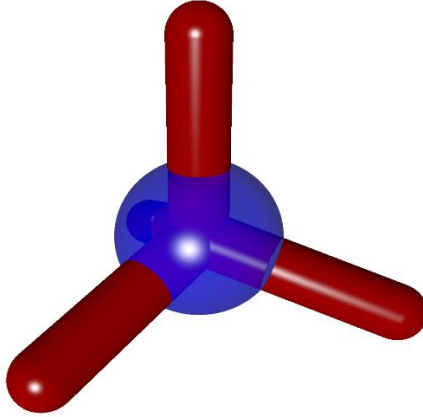
Figure 10: Tetrapod with Ψ = 0.53 (red) and sphere of the same volume as the tetrapod (transparent blue).

Table 1: Shape parameters for tetrapods and number of aggregates used to construct the respective packings.

Sphericity	AR	dp [mm]	Number of aggregates
0.99	1.1	9.8	2470
0.94	1.3	8.11	2520
0.86	1.5	7.15	2470
0.80	1.75	6.41	2300
0.75	2	5.9	2160
0.67	2.5	5.22	1920
0.62	3	4.78	1690
0.58	3.5	4.46	1490
0.55	4	4.205	1350
0.53	4.5	4	1350

0.51	5	3.835	1330
0.47	6	3.568	1100

Table 2: Shape parameters for dolosse and number of aggregates used to construct the respective packings.

Sphericity	AR	dp [mm]	Number of aggregates
1.00	1.1	10.068	3000
0.95	1.4	8.15	3000
0.92	1.5	7.73	3000
0.85	1.8	6.838	2900
0.81	2	6.425	2800
0.73	2.5	5.705	2700
0.68	3	5.228	2600
0.60	4	4.61	2200
0.55	5	4.206	2000
0.52	6	3.917	1650
0.49	7	3.692	1550

Table 3: Shape parameter for tetrahedra and number of aggregates used to construct the respective packings.

Sphericity	AR	dp [mm]	Number of aggregates
0.99	1.1	10.28	3000
0.97	1.5	7.94	3000
0.93	2	6.32	3000
0.87	2.5	5.312	3000
0.81	2.75	4.95	3300
0.74	3	4.67	3600
0.65	3.5	4.25	3300

0.58	4	3.947	2800
0.51	5	3.525	2400
0.43	7	3.04	1600
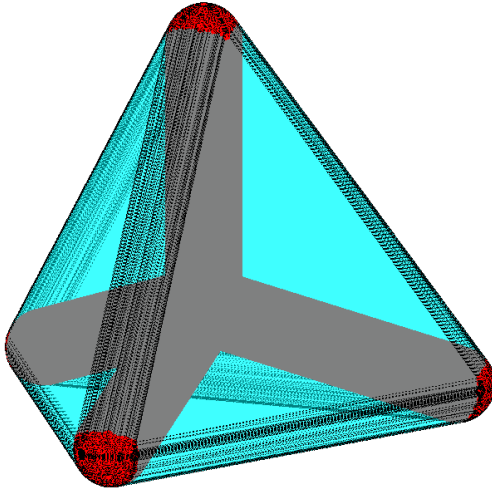
Figure 11: Visualization of the convex hull (cyan) enveloping a tetrapod with Ψ = 0.53 (red).

3.4.2 Discrete element method (DEM)

The DEM was originally developed by Cundall & Strack [80] for spherical particles, and has been extended to model non-spherical particles [81,121–123]. In this work, an in-house DEM framework is used which models non-convex aggregates by combining multiple intersecting spherocylinders to form the aggregates shown in Figure 9.

The DEM treats each aggregate as a discrete element moving freely in space. In the DEM time is advanced by performing the

following operations in a timestep: (i) based on the known position of the particles, $x(t)$, determine whether contacts exist, (ii) calculate the contact forces, (iii) determine the acceleration acting on the individual aggregates via Newton's second law of motion and (iv) update the new position of the aggregated, $x(t+\Delta t)$ through Eq. (3.3) and (3.4).

The velocity v_i of an aggregate i at timestep t is calculated through a third-order Adams-Bashforth scheme:

$$v_i(t) = v_i(t - \Delta t) + \frac{\Delta t}{12}[23a_i(t - \Delta t) \\ -16a_i(t - 2\Delta t) + 5a_i(t - 3\Delta t)] \qquad (3.3)$$

where $a_i(t)$ is the acceleration of aggregate i. The new position x_i of the aggregate is then obtained via:

$$x_i(t) = x_i(t - \Delta t) + \frac{\Delta t}{12}[23v_i(t - \Delta t) \\ -16v_i(t - 2\Delta t) + 5v_i(t - 3\Delta t)] \qquad (3.4)$$

Modelling non-spherical aggregates requires information on the aggregate orientation, angular velocity $\omega(t)$, and angular momentum $J(t)$. The angular momentum of aggregate i is found by integrating the net torque M acting on the aggregate:

$$J_i(t) = J_i(t - \Delta t) + \frac{\Delta t}{12}[23M_i(t - \Delta t) \\ -16M_i(t - 2\Delta t) + 5M_i(t - 3\Delta t)] \qquad (3.5)$$

To obtain the angular velocity ω_i the angular momentum is divided by the moment of inertia matrix I of the aggregate:

$$\omega_i(t) = \frac{J_i(t)}{I_i} = J_i(t)I_i^{-1} \qquad (3.6)$$

The orientation of the aggregate can be described by a rotation matrix based on Euler angles. However, this rotation matrix has

the disadvantage of having singularities. To circumvent this limitation, the DEM commonly employs quaternions [81]. The rotation matrix which describes the aggregate orientation can be calculated from the quaternion q, while the quaternion is calculated for each timestep by integration:

$$q_i(t) = q_i(t - \Delta t) + \frac{\Delta t}{12}[23\dot{q}_i(t - \Delta t)$$
$$-16\dot{q}_i(t - 2\Delta t) + 5\dot{q}_i(t - 3\Delta t)] \qquad (3.7)$$

with

$$\begin{bmatrix} \dot{q}_{i,1}(t) \\ \dot{q}_{i,2}(t) \\ \dot{q}_{i,3}(t) \\ \dot{q}_{i,4}(t) \end{bmatrix} =$$
$$\frac{1}{2}\begin{bmatrix} q_{i,1}(t) & -q_{i,2}(t) & -q_{i,3}(t) & -q_{i,4}(t) \\ q_{i,2}(t) & q_{i,1}(t) & -q_{i,4}(t) & q_{i,3}(t) \\ q_{i,3}(t) & q_{i,4}(t) & q_{i,1}(t) & -q_{i,2}(t) \\ q_{i,4}(t) & -q_{i,3}(t) & q_{i,2}(t) & q_{i,1}(t) \end{bmatrix}\begin{bmatrix} 0 \\ \omega_{i,x}(t) \\ \omega_{i,y}(t) \\ \omega_{i,z}(t) \end{bmatrix} \qquad (3.8)$$

Once the new positions, orientations, and (angular) velocities of all aggregates have been updated a new contact search starts.

Detecting contacts between spherocylinders requires the calculation of the distance between the central axes of neighboring spherocylinder (shown in red in Figure 12). If the distance between the central axes of two spherocylinders is smaller than two times the spherocylinder radius r the aggregates are in contact. In the present DEM framework, finding the distance between two line segments (i.e. central axes) is solved using the algorithm proposed by Lumelsky [87]. The contact point between two spherocylinders is the middle point of the shortest line between the central axes of two

contacting spherocylinders (see green line in Figure 12a). The contact forces (blue arrows in Figure 12) act at the contact point between two spherocylinders. If the central axes of two contacting spherocylinders share a parallel segment, as seen in Figure 12b, there is no single shortest line between the two central axes. In this case the contact point is the middle point of the line which is in the center of the parallel segment.

The contact force acting at the contact point can be decomposed into a normal contact force F_n and, assuming a non-zero friction coefficient, a tangential contact force F_t. Both contact forces are modelled by a linear spring dashpot which yields a constant coefficient of restitution. The contact force in the normal direction between aggregate i and j is given as:

$$F_n = \max\left(0, \quad \frac{s_n}{2}\delta_n - \eta_n\sqrt{2m_{ij}s_n v_n}\right) \qquad (3.9)$$

where s_n is the normal stiffness of the aggregate, δ_n is the overlap between the contacting spherocylinders, η_n is the normal damping factor, v_n is the normal component of the relative velocity between the aggregates at the contact point and m_{ij} is the effective inertial mass of aggregates i and j which is given by:

$$m_{ij} = \frac{m_i m_j}{m_i + m_j} \qquad (3.10)$$

In the tangential direction the contact force is modelled following Coulomb's law of friction:

$$F_t = \min\left(\mu\frac{s_n}{2}\delta_n, \quad \frac{s_t}{2}\delta_t - \eta_t\sqrt{2m_{ij}s_t v_t}\right) \qquad (3.11)$$

where μ is the coefficient of friction, η_t is the tangential damping factor, s_t is the tangential stiffness and v_t is the tangential component of the relative velocity between the aggregates at the point of contact. The accumulated tangential displacement at the contact point is calculated as $\delta_t = \int v_t \, dt$.
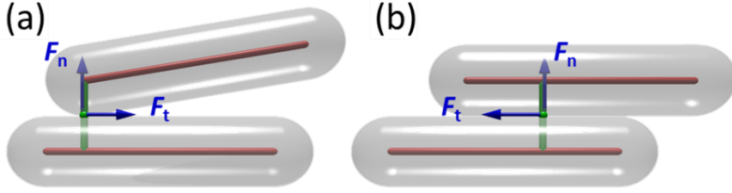
Figure 12: Sketch depicting two contacting spherocylinders. (a) Oblique contact. (b) Parallel contact.

Once all contact forces acting on a given aggregate i have been calculated they are summed up and the resulting force $F_{sum,i}$ allows to calculate the acceleration acting on aggregate i:

$$a_i(t + \Delta t) = \frac{F_{sum,i}}{m_i} \qquad (3.12)$$

For non-spherical aggregates contact forces also induce a torque M_i:

$$M_i(t + \Delta t) = \sum_c r_c \times (F_{n,c} + F_{t,c}) \qquad (3.13)$$

where the index c loops over all contacts of aggregate i and r_c is the vector pointing from the center of gravity of the aggregate to the contact point.

The values of the parameters used in the DEM simulations were chosen to model the properties of ABS aggregates [124]. The

61

parameters are listed in Table 4. It is worth noting that the DEM values chosen to describe the stiffness of the aggregates are commonly much lower than the physical values to allow for larger time steps as the time step size is typically ~20 times the collision time t_{col} which is given by [125]:

$$t_{col} = \frac{\pi}{\sqrt{\frac{s_n}{m_{ij}}(1 - \eta_n^2)}} \qquad (3.14)$$

In the present work, as it has been shown that the magnitude of the stiffness has negligible effects on the packing properties, a value of 10'000 N/m was chosen for the normal stiffness, which allows for a Δt of 10^{-5} s, [126]. The value for the tangential stiffness was chosen as half the normal stiffness in accordance with previous studies [118,121,127].

Table 4: Parameters used for DEM simulations.

Parameter	Symbol	Value
Density	ρ	1000 kg/m^3
Normal stiffness	s_n	10'000 N/m
Tangential stiffness	s_t	5'000 N/m
Coefficient of restitution	e	0.3
Normal damping factor	η_n	0.35
Tangential damping factor	η_t	0.3
Coefficient of friction	μ	0.35
Wall friction coefficient	μ_w	0.1
Time step	Δt	10^{-5} s

All aggregate packings are modelled in a cylindrical simulation domain with a diameter of 100 mm and a height of 700 mm, which matches the acrylic cylinder used for the physical experiments. The DEM domain is filled by creating aggregates

at a height of 600 mm in batches of 3 by 3 aggregates. Between each aggregate, there is a gap of the same size as the diameter of the constituent spherocylinders of the aggregate. Additionally, each aggregate is given a random orientation and a random initial velocity in both horizontal directions of v_{ini} (-0.5 m/s $< v_{ini} <$ 0.5 m/s). Immediately upon their creation, the aggregates fall to the bottom of the cylinder domain and after 0.11 s a new 3 by 3 batch of aggregates is created. This step is repeated until a sufficient number of aggregates has been created to yield a packing height of at least 350 mm. The number of aggregates used to model each packing is given in Table 1-Table 3. Once all aggregates are created, the packing obtains its equilibrium position within one second and the simulation is stopped.

The DEM data is exported as a stack of black and white (binary) images that represent horizontal slices through the packing. These slices are rendered using the ray tracing software POV-Ray [128]. An extended description of the rendering of the slices is given in chapter 3.4.5. The porosity ε of the DEM packings is determined by:

$$\varepsilon = \frac{1 - V_{agg}}{V_{domain}} \qquad (3.15)$$

where V_{agg} is the total volume of all aggregates and V_{domain} is the volume of the cylindrical domain, i.e. from the bottom to the highest point of the aggregate packing. For each type of aggregate, a fourth-order polynomial was fitted to the ε versus Ψ data points to yield an ε-Ψ relationship which can be used to evaluate the Carman-Kozeny equation. To construct the fluid domain for the LBM simulations, the geometrical information of the DEM packings is converted into STL files. An explanation of this conversion process is given in chapter 3.4.6.

3.4.3   Computing the tortuosity of a packing

The tortuosity is defined as the length of the shortest path through the pore space of a packing divided by the length of a straight line through the packing. In the present work the goal is to compute the tortuosity solely based on geometric information of the packing, i.e. the so-called geometric tortuosity [129]. Alternative methods to calculate the tortuosity, e.g. the hydraulic tortuosity which can be computed e.g. through the method proposed by Duda et al. [130], require also information on the fluid velocity in the porous medium. A separate investigation described in section E of the supplemental material shows that the method by Duda et al. [130] is a less suitable measure of the tortuosity of pavements constructed of artificial aggregates compared to the geometric tortuosity. Hence, a method to calculate the geometric tortuosity of packings was developed in this work. This method relies on the binary horizontal slices through the packing. Neighboring slices have a vertical separation of 0.2 mm. For all DEM packings investigated, the top and bottom 30 mm are ignored for the tortuosity analysis due to wall and free-surface effects.

The tortuosity calculation starts with the top slice of the central section of the packing. A grid of dots spaced 5 mm is drawn on this slice, see black dots in Figure 13. These black dots are drawn in the same positions on all slices. If a black dot lies inside an aggregate, the closest point not lying inside the aggregate is found (blue dots in Figure 13). For each blue dot a line is drawn connecting the blue dot and the associated black dot. The following restriction for finding the blue dots is applied: If the angle between the two lines connecting the black

dot with its associated blue dots on two subsequent slices is larger than 45° the blue dot on the second slice is rejected. Instead, a new blue dot is found which is closest to the center of the line connecting the black dot and the blue dot on the first of the two neighboring slices. This scheme is illustrated in Figure 13a where one of the black dots has been highlighted in yellow. The closest surface point to the yellow dot in the first slice, Figure 13a, is the red dot. In the following slice, Figure 13b, the closest surface point to the yellow dot is the green dot. The red dot from slice Figure 13a is superimposed on the slice in Figure 13b for demonstration. Since the angle between the line connecting the red and yellow dots and the line connecting the green and yellow dots is larger than 45°, the green dot will be rejected. Instead, a new closest surface point (purple dot) is found for the center of the line connecting the red and yellow dots. In the aggregate packings investigated here less than 0.01% of the dots were rejected. Furthermore, varying the rejection angle between 0° and 90° has no measurable effect on the calculated tortuosity values. However, changing the vertical resolution, i.e. the distance between slices could affect the determined tortuosity values.

Once all slices have been processed, a tortuous path through the packing is obtained by connecting each black dot with the corresponding black dot on the subsequent slice or with the corresponding closest blue dot if the black dot lies inside an aggregate. Such a tortuous path is sketched in Figure 13c. The tortuosity of one path is calculated by dividing the length of the path by the length of a straight line connecting the start and end of the path. To calculate the tortuosity of an entire packing the tortuosity of all paths for the given packing is averaged. Typically, 208 paths per packing are calculated. When varying

the number of paths from 80 to 3500 the computed tortuosity values fluctuate by only $\pm\,2\%$.
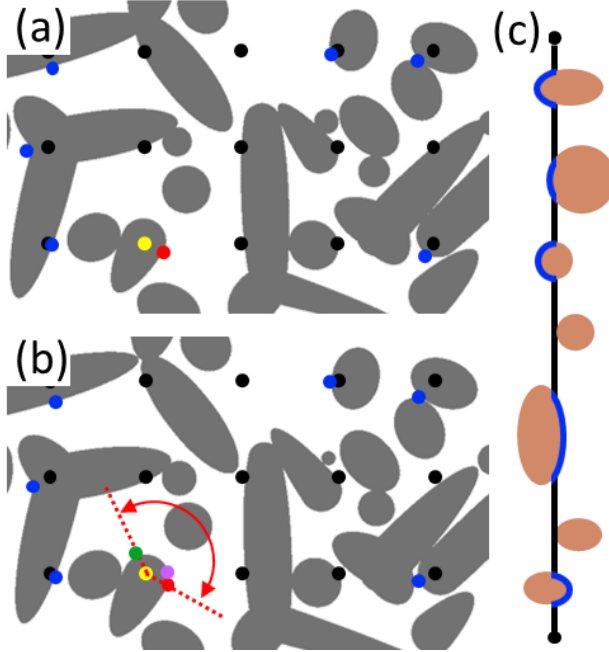
Figure 13: (a) Horizontal slice through a packing of tetrapods with Ψ = 0.53. (b) Horizontal slice that is located 0.2 mm below the slice shown in (a). (c) Illustration of the construction of a tortuous path through the packing.

3.4.4   Lattice Boltzmann method (LBM)

Owing to its high versatility for complex boundary systems, the LBM method is used to calculate the flow field in the aggregate packings. Here we use the open source LBM framework Palabos [131]. To this end the STL files are imported and the

surface of the aggregates is modelled by bounce-back walls. At the inlet a Poiseuille flow profile is prescribed with an average velocity $u = 0.05$ mm/s. This ensures a low Reynolds number laminar flow. Unfortunately, high Reynolds number flows, as encountered in the falling head experiments, cannot be modelled due to stability limitations of the LBM approach. Nonetheless, it is possible to compare the results of the falling head experiments and the simulations, provided that the experiments are evaluated with the Darcy-Forchheimer equation that is appropriate for turbulent flows [Eq. (3.18)], while the simulations are evaluated with the Darcy equation for laminar flows [Eq. (3.17)].

The outlet is modelled with a Neumann boundary condition, i.e. a zero-velocity gradient and a constant pressure equal to the ambient pressure. The modelled fluid is water with a density (ρ_w) of 1000 kg/m^3 and a kinematic viscosity (v_w) of 10^{-6} m^2/s. The LBM solver uses the incompressible Bhatnagar-Gross-Krook (BGK) model [132]. The non-dimensional lattice viscosity v_{lat} is varied between 0.01 and 0.05 to yield optimal convergence. The time step size dt and the lattice viscosity are related through:

$$dt = \frac{v_{lat}}{v_w dx^2} \qquad (3.16)$$

where dx is the lattice spacing. The fluid space is discretized using a D3Q19 lattice with equally spaced nodes in all three directions, i.e. $dx = dy = dz = 133.33$ μm, yielding up to 540 million nodes per simulation, with computations running on 420 CPU cores for approximately 12 hours.

Once the LBM simulations have reached a steady state, the permeability k is determined by applying Darcy's law:

$$k = \frac{L v_w \rho_w u}{\Delta P} \qquad (3.17)$$

where *L* is the height of the packing and ΔP is the pressure drop between the inlet and outlet.

3.4.5   Rendering binary slices from DEM packings

Modelling an aggregate packing with the discrete element method (DEM) yields a full geometric description of the packing. To calculate the tortuosity of this packing the geometric information needs to be presented as binary images of horizontal slices through the packing. In these images a white pixel denotes aggregate matter, whereas a black pixel denotes void space (see Figure 14).

The image slices are rendered using the ray tracing software POV-Ray [128]. The tabulated geometric information obtained from the DEM modelling is translated into a scene file for each slice using a python script. Scene files contain all information needed by POV-Ray to generate an image, such as the positions and dimension of all aggregates, as well was the position of the camera and light sources. The scene is set up such that an orthographic camera observes the packing form above with the light sources above/behind the camera and a black background. The aggregates are represented in the scene file as white objects, which are intersected by a flat rectangular box of 0.2 mm height to extract a slice. For subsequent slices this flat box is offset vertically by 0.2 mm.
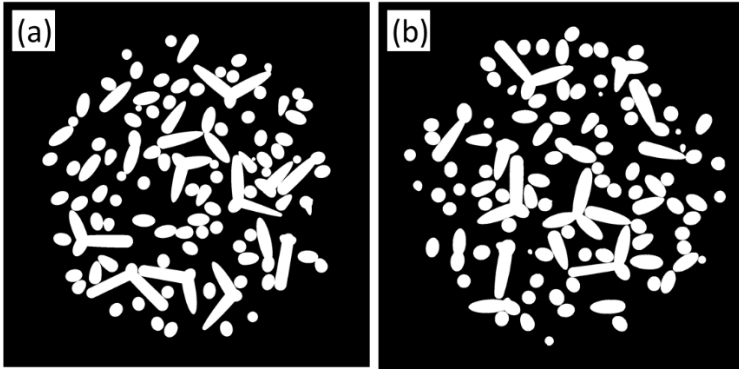
Figure 14: Horizontal binary slices of 0.2 mm height through a packing of tetrapods with Ψ = 0.53. (a) DEM packing with the slice being generated by ray tracing using the software POV-ray. (b) Physical packing imaged by X-ray CT. The software Avizo is used to post-process the data and to export the slice.

3.4.6 Creating the surface geometry of DEM packings

A DEM simulation yields the positions and orientations of the aggregates in a packing. From such a packing a 120 mm high central section is extracted. To be able to use the geometry data of this packing section as an input for the LBM simulations, the data needs to be converted into STL files. This is done via a python script using the package trimesh [133]. The script converts the position of each constituent spherocylinder of an aggregate into a trimesh object with the same position and orientation as the spherocylinder, representing the surface of a spherocylinder composed of triangles (see Figure 15a). When the objects corresponding to the aggregate-forming spherocylinders are combined, the resulting object has internal walls, as shown in the transparent view in Figure 15b. Such an object with internal walls is called non-manifold and is

69

generally undesired in STL files. Using a non-manifold STL file would lead to computational errors in the LBM simulations. To remove internal walls, the software trimesh computes the boolean union of the object shapes and generates the surface of the aggregate composed of triangles (see Figure 15c).

The only variable parameter in this process is the number of triangular facets used to represent a surface. Decreasing the number of facets would make a round surface to become more angular. For the cylindrical surfaces used here it was found that 32 facets along the length of a spherocylinder are sufficient to resolve the curvature of the surface. Increasing the number of facets further does not affect the results of the permeability simulations. Finally, the complete 120 mm high packing section is placed centrally into a 150 mm long cylinder with diameter 100 mm. This cylinder represents the fluid domain considered for the permeability computations. Additional simulations confirmed that increasing the cylinder length beyond 150 mm does not affect the permeability values obtained. A visualization of the STL surface of a packing section (tetrapods $\Psi = 0.53$) is given in Figure 15d.
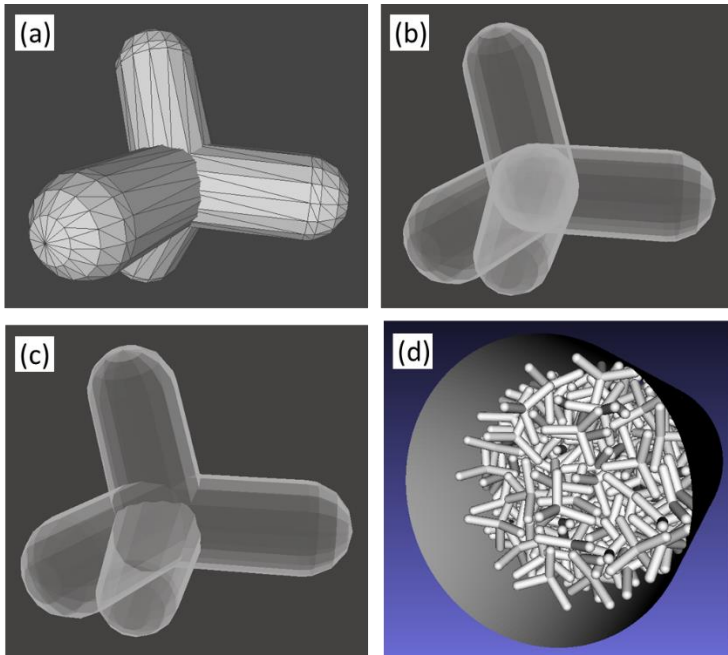
Figure 15: (a) Four objects which correspond to the triangulated surfaces of the spherocylinders of a tetrapod (Ψ = 0.67). (b) Transparent view of the tetrapod showing internal walls. (c) Boolean union of the four objects of a tetrapod which removes internal walls. (d) Visualization of a tetrapod (Ψ = 0.53) packing section.

3.5 Experimental materials and methods

3.5.1 Polymer aggregates

To verify the numerical results experimentally, physical tetrapods of two different sphericities ($\Psi = 0.87$ and $\Psi = 0.53$) are used. These physical aggregates are manufactured from an ABS polymer via injection molding with identical geometries as the numerical aggregates. Images of the physical aggregates

can be found in Figure 16. These two tetrapod shapes are chosen to cover the wide range of tetrapod sphericities that were investigated numerically ($0.99 \leq \Psi \leq 0.47$). Since initial comparisons of the experimentally and numerically determined porosity showed good agreement it was deemed unnecessary to manufacture additional shapes for validation.
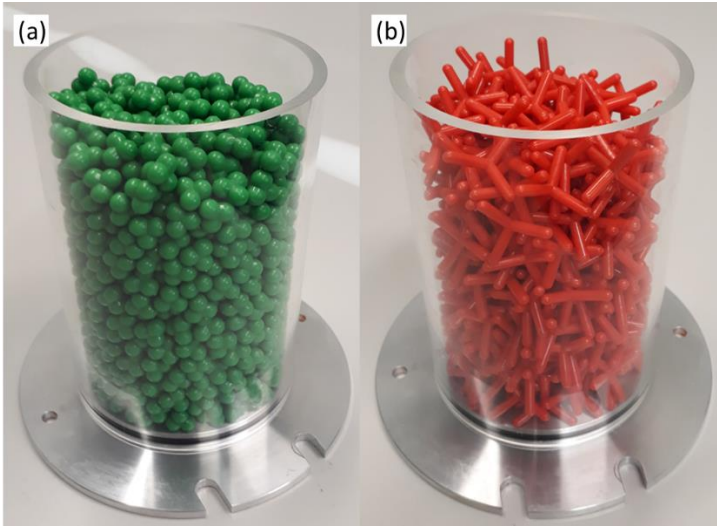
Figure 16: Physical tetrapods of different sphericities packed into an acrylic pipe with 100 mm diameter, the sphericities of the tetrapods are: (a) $\Psi = 0.87$ and (b) $\Psi = 0.53$.

3.5.2   Volumetric porosity determination

To create the packings, the injection molded aggregates are poured into an acrylic cylinder of inner diameter 100 mm and a height of 140 mm. While pouring, it is ensured that the resulting packing is random, for example by not vibrating the packing, which could reduce randomness by aligning

aggregates and potentially increasing the packings load-bearing capacity. Ensuring randomness can lead to large voids in packings of low sphericity (e.g. tetrapods with $\Psi = 0.53$), due to arching of the aggregates. Such large voids are tolerated and are considered part of the statistical variations in the packings. The porosity of these packings is measured by filling the interstitial void space between the aggregates with water such that the aggregates are fully submerged. The porosity is given by the weight of the water divided by the density of water and the volume of the pipe containing the aggregates. Since the aggregates are buoyant in water the packing is weighed down by a wire mesh placed on top.

3.5.3   Permeability using the falling head method

The permeability of the packings is determined using the so-called falling head method, a schematic of the experimental setup is shown in Figure 17. An acrylic cylinder with 100 mm inner diameter and a height of 1.8 m is covered at the bottom with a wire mesh with a mesh size of 8 mm. Aggregates are poured onto this wire mesh to create a packing with a height of 120 mm. For aggregates that are small enough to fall through this wire mesh a second layer of wire mesh is added, rotated by 45°. The packing is kept in place against buoyance by a weighted wire mesh placed on top, which also prevents a rearrangement of the aggregates due to turbulences during an experiment. For a typical experiment a plate is pushed against the bottom of the cylinder to seal it, and the cylinder is filled with water to a height of 1.6 m above the sample. While filling the cylinder it was ensured that the water jet does not impinge on the packing, to prevent any disturbance of the packing. If a rearrangement of the aggregates is observed while filling the

cylinder with water or during an experiment, the experiment is repeated with a freshly prepared packing. An experiment is started by removing the sealing-plate abruptly. The water level is recorded using a Canon EOS 77D camera at 50 frames per second. For the evaluation of the permeability the water level decrease from 1.6 m to 1.3 m is disregarded to ensure the water column is not subject to inertial effects. The recording is stopped once the water level drops to 0.1 m above the packing sample. Hence, the water level from 1.3 m to 0.1 m above the sample is used to determine the permeability of the packing.
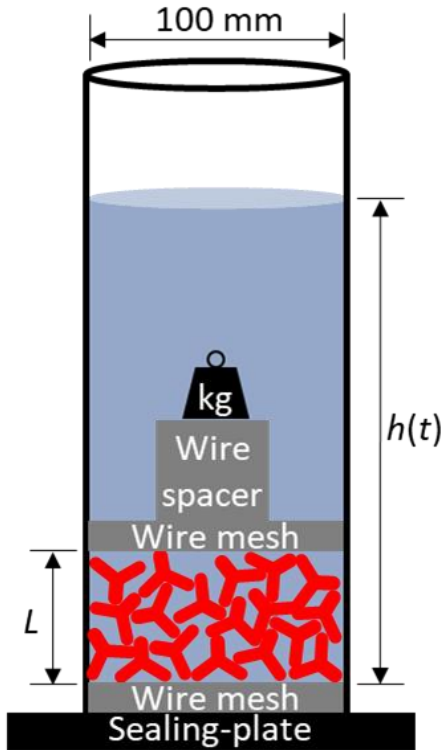

Figure 17: Schematic of the setup for the falling head experiments.

During a falling head experiment the decrease of the water level h is recorded as a function of time, yielding $h(t)$-curves which are plotted in Figure 18. For each of the tetrapod shapes [(a) Ψ = 0.87 and (b) Ψ = 0.53] three different packings were constructed and for each of these samples three falling head experiments were performed, yielding 9 $h(t)$-curves for each tetrapod shape, which agree very well with each other. A second order polynomial was fitted to each $h(t)$-curve to allow for a smooth, differentiable function. These $h(t)$-curves are used to determine the permeability of the packing via the Darcy-Forchheimer equation for turbulent flows through porous media, viz.

$$-\frac{dp}{dx} = -\frac{\rho_w g (h(t) + L)}{L} = \frac{v_w \rho_w}{k}\frac{dh}{dt} + \frac{\rho_w}{k_{in}}\left|\frac{dh}{dt}\right|\frac{dh}{dt} \quad (3.18)$$

Here, $\frac{\partial p}{\partial x}$ is the pressure drop across the height of the sample L which is equal to the hydrostatic pressure of the water column, ρ_w is the density of water, v_w is the kinematic viscosity of water and g is the acceleration due to gravity. As the experiments are performed at room temperature the values at 20°C are used for ρ_w and v_w, varying these values between 5°C and 40°C has negligible effects on the results. Using the Darcy-Forchheimer equation [Eq. (3.18)] for turbulent flow instead of the Darcy equation [Eq. (3.17)] for laminar flow ($Re < 1$) is necessary since high flow velocities with $Re > 9000$ are observed in the experiments.

To calculate the permeability k and the inertial permeability k_{in}, a system of two Darcy-Forchheimer equations is constructed:

$$
\begin{bmatrix}
v_w \rho_w \dfrac{d}{dt} h(t_1) & \rho_w \left|\dfrac{d}{dt} h(t_1)\right| \dfrac{d}{dt} h(t_1) \\
v_w \rho_w \dfrac{d}{dt} h(t_2) & \rho_w \left|\dfrac{d}{dt} h(t_2)\right| \dfrac{d}{dt} h(t_2)
\end{bmatrix}
\begin{bmatrix}
\dfrac{1}{k} \\
\dfrac{1}{k_{in}}
\end{bmatrix}
$$

$$
= \begin{bmatrix}
-\dfrac{\rho_w g (h(t_1) + L)}{L} \\
-\dfrac{\rho_w g (h(t_2) + L)}{L}
\end{bmatrix}
\tag{3.19}
$$

This system of equations is solved for each $h(t)$-curve in intervals of 0.1 s and with $t_2 = t_1 + 0.1$ s. The results of this evaluation are shown in Figure 19 which plots the permeability k as a function of the water level h. This approach yields permeabilities that decrease with decreasing water level, although one would expect k to be independent of the water level (and flow velocity). The reason for these varying values of k are most likely flow-rate dependent pressure losses in the falling head setup that are not accounted for in Eq. (3.19). To correct for this, k_{in} which also varies with h, is fixed to the mean k_{in}-value that is obtained from an initial evaluation of each curve where k_{in} is allowed to vary. Fixing k_{in} leads to fairly stables values of k that show little variation with h. In a final step the k values obtained from the re-evaluation of the h(t)-curves are averaged over the whole range of h and subsequently also averaged over all of the 9 curves that were acquired for each of the two tetrapod shapes. The error-bars give one standard deviation of the 9 k values obtained from the final averaging step.
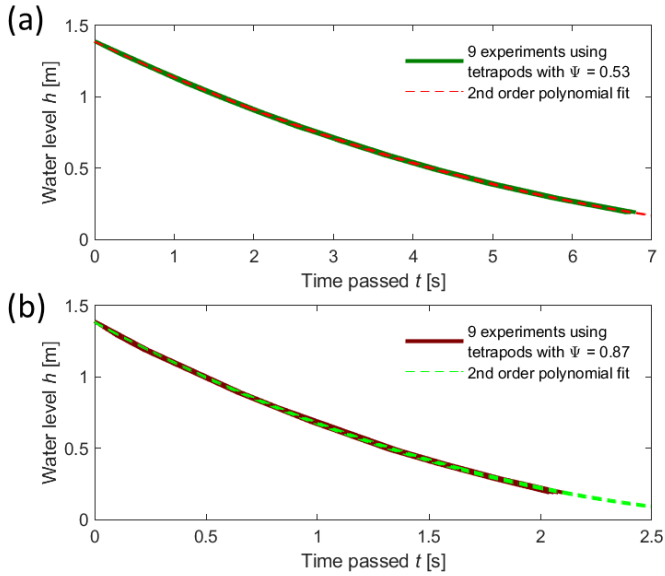
Figure 18: h(t)-curves acquired during falling head experiments for packings of tetrapods with (a) Ψ = 0.87 and (b) Ψ = 0.53. The dashed lines show the polynomials fitted to each h(t)-curves.
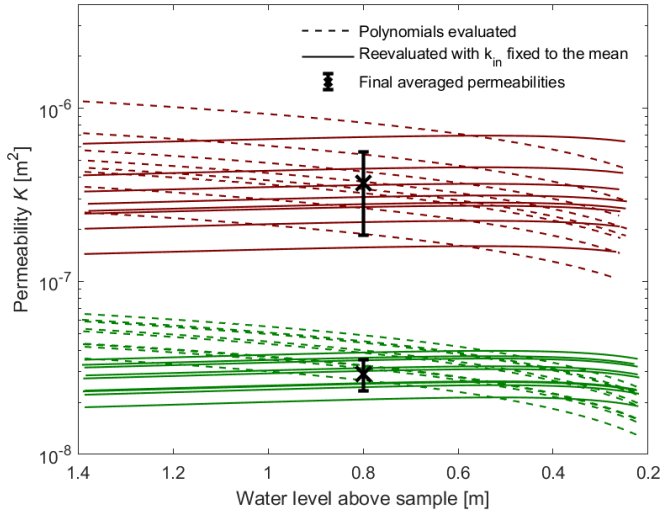
Figure 19: Permeabilities obtained by evaluating the h(t)-curves shown in Figure 18 using two different approaches. The green and red curves show the results for tetrapods with $\Psi = 0.87$ and $\Psi = 0.53$, respectively.

3.5.4   X-ray computed tomography

The full, 3D structure of the physical packings of tetrapods with $\Psi = 0.53$ (see Figure 9 and Figure 16b) is recorded using X-ray computed tomography (CT). Due to the effort required to prepare a CT it was decided not to image also the second experimental tetrapod type ($\Psi = 0.87$). A packing of height 400 mm was poured into an acrylic cylinder (100 mm inner diameter), ensuring randomness and making this packing equal to the experimental packings used for the porosity and permeability investigations. The different height of the packing used for CT and other experimental packings does not affect

the packing structure, which was confirmed by numerical simulations. From the packing of 400 mm height a central section of 150 mm height (120 mm diameter) was recorded. The height of this central section is limited by the field of view of the X-ray setup. The X-ray CT setup consisted of an X-ray source (Viscom XT9160) operated at 70kV and 140 µA, a digital detector with 2048x2048 pixels (XRD 1621 CN3 ES, Perkin Elmer) and a CsI(Tl) scintillator yielding a high spatial resolution of $66.41 \times 66.41 \times 66.41$ µm3 per voxel.

The CT data is post-processed in multiple steps using the software Avizo v9.7 (Thermo Fisher Scientific). In the first step the grayscale data is thresholded to separate voxels that contain polymer aggregates from the voxels containing air. The thresholding value was found to have a negligible influence on the total aggregate volume in the CT data due to the large difference in the X-ray absorption between the ABS polymer and air, consequently a thresholding value of 0.2 was chosen (on a range from 0 to 1). The injection molding process produces holes within the aggregates that arise when ABS shrinks during cooling. In a post-processing step these holes are filled digitally such that they do not contribute to the porosity of the packings. Subsequently, a water-shedding algorithm is used to identify the individual aggregates in the CT data. At the top and bottom of the recorded 150 mm high section some aggregates are incomplete as they are not fully inside the imaged section. Digital sieving is used to remove incomplete aggregates such that only complete aggregates are used for further analysis.

To be able to use the CT data for LBM simulations the post-processed data is exported as a stereolithography (STL) file using Avizo. The STL file describes the surface of the

79

aggregates through triangular facets. The CT data is also exported as a stack of binary images that represent horizontal slices (thickness 0.2 mm) through the packing. These binary images allow to distinguish pixels that are aggregate matter or void. An example of such a binary slice is shown in Figure 14.

3.6 Results and Discussion

3.6.1 Convexity

Figure 20 plots the convexity (Ω) as a function of sphericity. For all three aggregate shapes studied here, Ω decreases monotonically with decreasing Ψ. For tetrapods and dolosse the slope of the Ω-Ψ-curves increases for $\Psi < 0.85$. The reason for this change in slope is that for $\Psi > 0.85$ the cylindrical section of one (or more) of the constituent spherocylinders is completely or partially concealed. This can be seen for example in Figure 9 for dolosse with $\Psi = 0.85$. Here the central spherocylinder is completely concealed by the two outer spherocylinders. If the sphericity is decreased, e.g. dolosse with $\Psi = 0.73$ (Figure 9), the third (central) spherocylinder becomes exposed, leading to an increasing reduction in Ω with decreasing Ψ. For tetrahedra there is a change in the slope of the Ω-Ψ-curve for $\Psi < 0.7$. The reason is similar as discussed for the other two shapes, i.e. for tetrahedra with $\Psi > 0.7$ parts of the cylindrical surface of the constituent spherocylinders are concealed in the core of the aggregate. For $\Psi < 0.7$ the core of the aggregate is exposed fully to the outside and the previously concealed cylindrical surface sections contribute to the surface area of the aggregate, hence decreasing Ω.
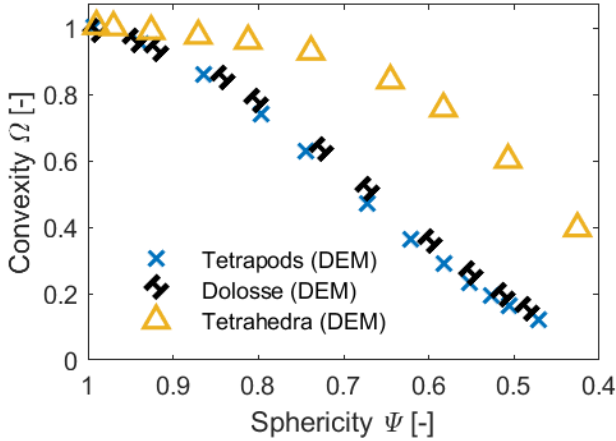
Figure 20: Convexity of the aggregates studied here as function of the sphericity.

3.6.2 Porosity

Combining Darcy's law, Eq. (3.1), with the Carman-Kozeny equation, Eq. (3.2), predicts that the permeability of a packing increases with increasing aggregate sphericity Ψ and increasing packing porosity ε.

Figure 21 plots the porosity of a packing as a function of the sphericity of the packing-forming aggregates. The data in Figure 21 contains both porosity data from DEM simulations and porosity data obtained experimentally by either volumetric methods or the analysis of X-ray CT data. Comparing the numerical DEM data of tetrapods (blue crosses) with the results of the experimental packing of tetrapods (green and red crosses) shows excellent agreement, confirming that DEM is a viable numerical approach to investigate packings of complex-

shaped aggregates. The excellent agreement also shows, that despite differences in the experimental and numerical pouring protocol, similar packings are created, because both pouring protocols ensure a high degree of randomness. The experimental tetrapod ($\Psi = 0.53$) packing with an X-ray CT determined porosity (red plus) of $\varepsilon = 0.685$ is lower than the porosity derived by DEM ($\varepsilon = 0.7$). This is due to the fact that the CT shows a denser-packed central section of the sample, while the DEM packing also includes aggregates in the porosity determination that are located at the bottom of the packing where the porosity is higher due to wall effects. Further evidence for the predictive nature of the DEM simulations is provided by the porosities determined for packings of almost spherical aggregates ($\Psi = 0.99$) which lie in the range $0.368 < \varepsilon < 0.399$. These porosity values are close to the established value for a random packing of spheres of $\varepsilon = 0.366$ [68].

It is worthwhile to mention that for all three aggregate types there is a minimum in the packing porosity for $\Psi \approx 0.92$. Such a minimum in the porosity of packings that are composed of slightly non-spherical shapes, i.e. $0.99 > \Psi > 0.9$, is well established and has also been reported for other particle types such as ellipsoids or spherocylinders [37,41,45,134]. Generally, for $\Psi < 0.92$, the porosity of a packing increases with decreasing sphericity. While the behaviour of tetrapods and dolosse overlaps, the porosity of packings of tetrahedra increases to a lesser extend with decreasing sphericity. This finding shows that for non-spherical particles, the sphericity of an aggregate is not the only parameter affecting the porosity of a packing [135]. This observation is re-affirmed by Figure 20 which shows that the convexity of tetrahedra can differ from the convexity of tetrapods by up to 0.47 for an equal sphericity. Nevertheless, for $\Psi < 0.92$ the monotonic increase of packing

porosity with decreasing sphericity holds for all aggregate shapes and shows that it is possible to construct packings of very high porosity when using aggregates of low sphericity, e.g. tetrapods with $\Psi = 0.47$ have $\varepsilon = 0.78$. Packings with such high porosities have the potential to enable novel applications such as energy harvesting from recyclable pavements. However, with regards to novel applications it has to be considered that variations in the sphericity of the aggregates also affects the structural properties of the aggregate packing such as stress distribution [118]. To be able to withstand the high inter-particle stresses found in packings of low sphericity aggregates requires material with sufficient mechanical strength. For the use in pavements tetrahedra with $\Psi \approx 0.5$ might offer a good compromise between high porosity and a high compressive strength, due to their convex shape. While lower sphericity tetrahedra would pack in a more porous way, tetrahedra with $\Psi < 0.5$ become so slender that their corners can penetrate into the core of other tetrahedra aggregates which would lead to interlocking and hence reduce the workability of the packing. Conversely, if a packing is required that can interlock, e.g. for freestanding structures, dolosse might be favorable since they have opposing faces.

In the following we will utilize the observation that by varying aggregate sphericity, packings with a wide range of porosities can be constructed to assess the validity of the Carman-Kozeny correlation for differently shaped aggregates and a wide range of packing porosities.
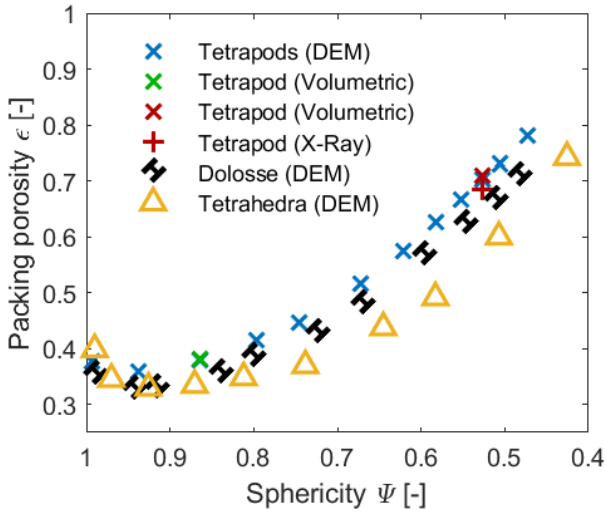
Figure 21: Packing porosity ε as a function of the sphericity of the packing-forming aggregates Ψ. Each packing was constructed of aggregates of a single shape.

3.6.3 Tortuosity

Figure 21 has demonstrated that the packing porosity depends on the aggregate sphericity Ψ, as well as the aggregate convexity, and that aggregates of different shapes but similar sphericity do not necessarily form packings with the same porosity. However, there is a second question to be addressed: Do packings of aggregates of different shapes but similar sphericity form pore spaces of similar morphology? Answering this question requires a descriptor for the morphology of the pore space. In the following we will use the tortuosity τ as a descriptor for morphology of the pore space. Figure 22a plots the variation of τ with aggregate sphericity Ψ for the three

different aggregate shapes studied, we observe a convex-shaped trend of τ with Ψ with a maximum in τ at $\Psi \approx 0.92$ for tetrapods and dolosse. The overall behavior of tetrahedra is similar with a maximum in τ located at $\Psi = 0.81$.

For tetrapods and dolosse the relationship between τ and Ψ (Figure 22a) shows a similar trend as the relationship between ε and Ψ (Figure 21), albeit mirrored along the Ψ axis. Both ε and τ have an extremum at $\Psi \approx 0.92$. The tortuosity of the tetrapod packing ($\Psi = 0.53$) as determined by X-ray CT is $\tau = 1.61$, agrees well with the DEM derived tortuosity of the same packing which is $\tau = 1.58$. The fact that for packings of tetrapods and dolosse of low Ψ we obtain high values of ε and low values of τ would suggest that these packings would feature a high permeability.

Packings of tetrahedra show some differences to the tortuosity of packings of tetrapods and dolosse, viz. the tortuosity of packings of tetrahedra increases for $\Psi > 0.81$ with increasing Ψ, but drops sharply to $\tau = 2.4$ at $\Psi = 0.74$. The reason for this drop is that at $\Psi = 0.81$ the inside space of the tetrahedron is closed and inaccessible from the outside, similar to the example shown for $\Psi = 0.97$ in Figure 9. The shortest path through a packing is a curve around the (outer) surface of the entire tetrahedron, leading to a long path length. Additionally, closed tetrahedra tend to align face to face leaving no void space between the aggregates, increasing the path length further. However, for $\Psi \leq 0.74$ tetrahedra have an open structure, e.g. as shown for $\Psi = 0.43$ in Figure 9. For such an open tetrahedron the inside of the aggregate becomes accessible, offering a shortcut through the aggregate resulting in turn in a shorter path through a packing. For $\Psi < 0.74$, τ decreases with decreasing sphericity in a similar fashion as for tetrapods and dolosse, yet

for a given sphericity, the value of τ for packings of tetrahedra is higher than for tetrapods and dolosse. The results above show that aggregates of different shapes but similar sphericity do not necessarily form packings of similar pore space morphology. However, for all particle shapes we find overall similar trends between τ and Ψ and between ε and Ψ which hint towards a correlation between τ and ε.

Figure 22b shows that there is a linear correlation between τ and ε for $\varepsilon > 0.35$ that can be approximated by:

$$\tau = -2.4\,\varepsilon + 3.27 \qquad\qquad (3.20)$$

If this linear correlation is extended to higher values of ε, it gives $\tau \to 1$ for $\varepsilon \to 1$. Indeed, a value of $\tau = 1$ at $\varepsilon = 1$ is expected since a tortuous path through a volume without any aggregates is a simple straight path. However, for $\varepsilon < 0.35$ we observe a non-linear increase of τ with decreasing porosity for packings of tetrahedra. Packings with such high tortuosity values (i.e. $\tau > 2.5$) correspond to the previously discussed packings of closed tetrahedra which align face to face.

In the past, a large number of correlations relating τ to ε have been proposed [136–138]. However, similar to the Carman-Kozeny correlation, these functions have typically not been tested for porous structures covering a wide range of values for ε, but rather packings of very specific particle shapes such as spherical packings ranging from the random-close to random-loose packing limit ($\varepsilon = 0.366 – 0.46$) [139] or random packings of fibers ($\varepsilon = 0.9 – 0.96$) [140]. In other works the τ-ε correlations have been tested over a wider range of values for ε, but for artificial structures such as fractals or randomly placed obstacles [130,141]. Thus, in the following, the packings of aggregates model by DEM, which cover a wide

range of porosity values and that have been validated by physical experiments, are used to establish a τ-ε relationship, viz:

$$\tau = 1 - p\,ln(\varepsilon)\quad with\,p = 1.5 \qquad (3.21)$$

However, it is worth noting that Eq. (3.21) cannot capture the non-linear behavior of tetrahedra for $\tau > 2.5$. The reason is that Eq. (3.21), as most other τ-ε correlations, is developed for random isotropic porous structures. As tetrahedra tend to align face to face (and with the walls) for $0.97 \leq \Psi \leq 0.81$ ($\varepsilon < 0.35$) such packings cannot be considered fully random.

The linear correlation between τ and ε (when excluding particular aggregate structures), indicates that tortuosity might not be required as an additional parameter to determine the permeability of a packing, instead tortuosity can be capture by porosity through a scaling factor.
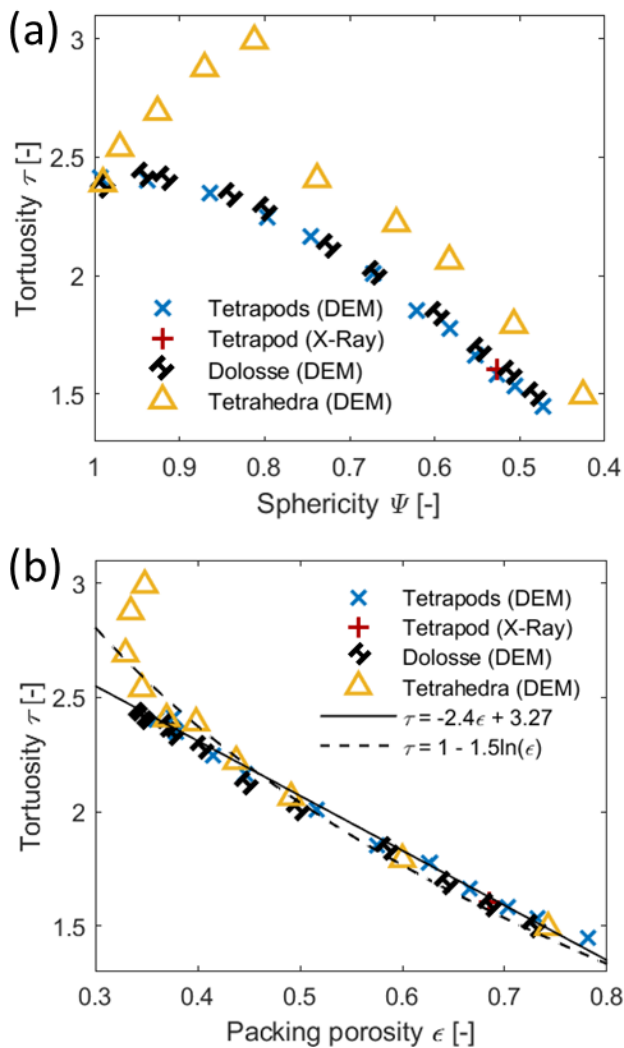
Figure 22: (a) Tortuosity of a packing as a function of the sphericity of an aggregate Ψ. (b) Tortuosity of a packing as a function of the packing porosity ε.

3.6.4 Comparing geometric and hydraulic tortuosity

The previous section describes the method that was established in this work to compute the geometric tortuosity. There exist alternative methods to compute the tortuosity of a packing that, however, require e.g. information on the fluid velocity in the pore space (hydraulic tortuosity) [129]. One established method to compute the hydraulic tortuosity is the method proposed by Duda et al. [130] that can be reduced to the formula:

$$\tau_{hyd} = \frac{\langle u \rangle}{\langle u_x \rangle} \tag{3.22}$$

where u denotes the magnitude of the fluid velocity and u_x denotes the velocity in the main flow direction, i.e. in the axial direction of the cylinder containing the aggregate packing and $\langle \rangle$ denotes the spatial average over all points of the fluid domain. The fluid velocities can be obtained from the Lattice Boltzmann method (LBM) simulations that are described in section 3.4.4.

Figure 23 plots a comparison between the geometric tortuosity and the hydraulic tortuosity computed via Eq. (3.22). The results of the geometric tortuosity are represented by

$$\tau = 1 - 1.5 \, ln(\varepsilon) \tag{3.23}$$

Figure 22 confirms that Eq. (3.23) is a good fit for the geometric tortuosity of aggregate packings. Figure 23 shows that the values of the (geometric) tortuosity represented by Eq. (3.23) are up to 200% higher compared to the values of the (hydraulic) tortuosity obtained for the same packings using Eq. (3.22). There are several reasons for this difference. Firstly, the differences in determining the tortuosity, while Eq. (3.23)

89

represents the geometric tortuosity using possible paths through a packing that contact with and curve around aggregates (see Figure 13), the paths used to calculate the hydraulic tortuosity, Eq. (3.22), follow streamlines of fluid elements. Such streamlines "cut" corners as they follow smoother and hence shorter paths compared to the paths that are considered for the geometric tortuosity. Secondly, the values of the geometric tortuosity consider all sections of the fluid domain equally, since they are calculated for paths originating from seed points that are evenly spaced over the cross-section of an aggregate packing. Conversely, when calculating the hydraulic tortuosity, spatial averaging leads to a dominance of higher velocities. In packings such as the ones investigated here a considerable fraction of the fluid bypasses the packing by flowing close to the cylindrical walls where the porosity approaches 1. Due to the high porosity in this annular region, the streamlines in this bypassing flow are also oriented predominantly in the main flow direction. Consequently, the hydraulic tortuosity is dominated by the high velocity bypass flow which coincidentally is also where the shortest streamlines are found, yielding in turn lower values for the (hydraulic) tortuosity.

Figure 23 also plots the tortuosity values obtained by Duda et al. [130]. Duda et al. [130] applied Eq. (3.22) for artificial two-dimensional structures that were created by the random placing of equally sized square-shaped obstacles. The tortuosity values of Duda et al. [130] lie between our values of the geometric and hydraulic tortuosity, which is not unsurprising since the artificial 2D structures investigated by Duda et al. [130] differ significantly from the packing structures (3D) investigated here.

The objective of the present work is to evaluate the permeability of artificial aggregate shapes for use in construction applications, such as porous asphalt concrete pavements. A road pavement can be considered as a semi-infinite structure, with a short vertical dimension but large horizontal dimensions. Since the main flow direction of water through a porous pavement is the vertical direction, the water flow is not subject to wall effects. Consequently, the geometric tortuosity which does not over-represent wall effects, is more representative for the tortuosity of artificial aggregate packings in pavement applications, compared to the hydraulic tortuosity according to Eq. (3.22).
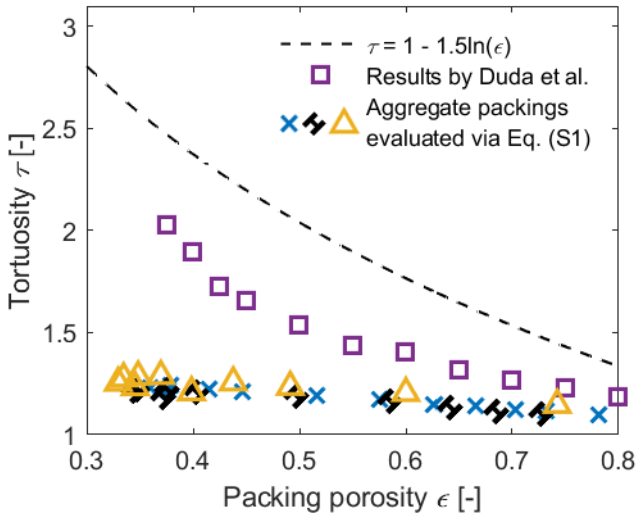

Figure 23: Tortuosity as a function of the packing porosity, comparing the results of the geometric tortuosity of aggregate packings computed via the method used in this work (see section 3.4.3), which are represented by the correlation τ = 1-1.5ln(ε) and the hydraulic tortuosity computed via Eq. (3.22). The results by Duda

et al. [130] *have been obtained for artificial two-dimensional structures.*

3.6.5 Permeability

Figure 21 has shown that the packing porosity increases with decreasing particle sphericity (for $\Psi < 0.92$); similarly, also the packing tortuosity decreases with decreasing permeability (Figure 22), except for tetrahedra for $\varepsilon < 0.35$. Both findings suggest that the packing permeability increases with decreasing particle sphericity. To test this hypothesis and to test the validity of the Carman-Kozeny correlation for packings of complex-shaped aggregates, the permeability of packings was investigated numerically via LBM simulations and experimentally using the falling head method. Figure 24a plots numerically and experimentally determined permeabilities k as a function of the particle sphericity Ψ.

The k-Ψ data plotted in Figure 24a show a similar trend as the ε-Ψ data given in Figure 21, i.e. also the permeability has a minimum at $\Psi \approx 0.9$ and for $\Psi < 0.9$ the permeability increases monotonically with decreasing Ψ. Note that the k-Ψ data is plotted, as it is typically done, on a semilogarithmic scale. The strong similarity of the k-Ψ and ε-Ψ trends suggest a direct correlation between k and ε (see below). When comparing the numerically determined permeabilities with the predictions of the Carman-Kozeny correlation [Eq. (3.2)] a good agreement is obtained. Since the Carman-Kozeny correlation only depends on Ψ, ε and the (equivalent) aggregate diameter, this indicates that the tortuosity is not required to predict accurately the permeability of a packing. For tetrapods with $\Psi = 0.87$ and $\Psi = 0.53$, the permeability was also determined experimentally using the falling head method (green and red crosses in Figure 24a with the error bars providing the standard deviation based

on nine measurements). The experimental results deviate from the LBM results by a factor of 2.3 and 2.8 for $\Psi = 0.87$ and $\Psi = 0.53$, respectively. An explanation for this deviation lies presumably in the particularities of the experimental setup, e.g. the wire mesh that is required to keep the packing in position introduces an additional pressure drop. Nevertheless, also the experimental results follow the trend of the k-Ψ behaviour of tetrapods as predicted by the Carman-Kozeny correlation and the LBM results. The values of the permeability computed by LBM for a packing of tetrapods with $\Psi = 0.53$ using the packing structure determined either by X-ray CT or DEM differs only by 9%. This excellent agreement indicates that the differences in the permeability obtained from the falling head method and LBM simulations are due to the falling head method instead of differences between the experimental and numerically generated packing structures. Especially for tetrapods with $\Psi = 0.53$ it could be observed during the experiments that the aggregates fall into the mesh with their "arms" sticking out, leading to a local alignment of the aggregates which could increase the packing fraction and therefore increase the pressure drop and in turn decrease the permeability. One way to reduce the differences between the LBM simulations and the permeability experiments could be to including the wire mesh in the numerical simulations to model the additional pressure drop of the mesh itself as well as the influence of the mesh on the packing structure. Modelling the mesh was omitted in this work as it would be associated with great complexity.

Furthermore, Figure 24b plots k as a function of ε to investigate the correlation between k and ε as suggested by the similarity of the k-Ψ and ε-Ψ curves. We find that the k-ε data can be correlated well ($R^2 = 0.968$) by the function:

$$k = 5.3^9 \, e^{7.3\varepsilon} \qquad\qquad (3.24)$$

Eq. (3.24) covers a wide range of porosities, shapes and sphericities and is believed to be useful to determine the permeability of packings of aggregates of a known porosity, for aggregates with equivalent diameters similar to the ones studied here. Importantly, Eq. (3.24) covers both concave and convex particle shapes.
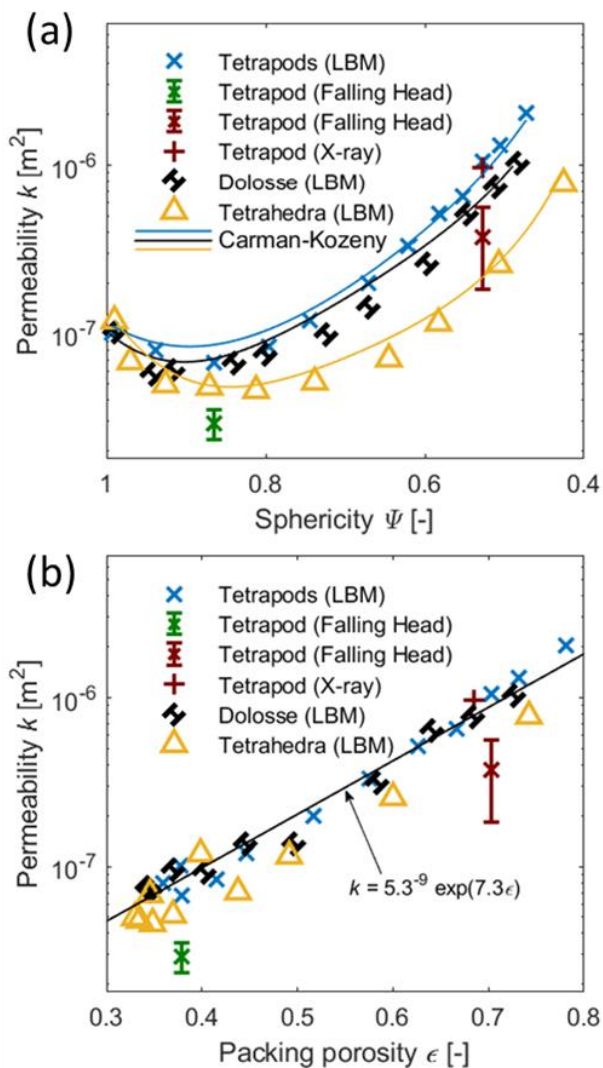
Figure 24: (a) Permeability of aggregate packings as function of the aggregate sphericity. (b) Permeability as a function of the packing porosity.

3.6.6 Permeability for varying LBM simulation Reynolds number

In the following we will investigate whether the numerically obtained results for the permeability k vary with the Reynolds number (Re). To this end, simulations were performed with the inlet velocity u varying from $5 \cdot 10^{-5}$ m/s to $5 \cdot 10^{-2}$ m/s, which corresponds to $5 \leq Re \leq 5000$ when choosing the cylinder diameter of 0.1 m as the relevant length scale. In comparison, all simulations discussed in the previous section were performed with $Re = 5$, while in the falling head experiments using tetrapods of $\Psi = 0.87$ or $\Psi = 0.53$ the Reynolds number was in the range of, respectively $10'000 \leq Re \leq 28'000$ and $33'000 \leq Re \leq 80'000$. An overview of the LBM simulations of varying Re is given in Table 5. To ensure numerical stability for $Re > 50$ the Smagorinsky model [142] was employed. The accuracy of the Smagorinsky model was validated by comparing its results for low Re flows with the predictions of the classic Bhatnagar-Gross-Krook (BGK) model (simulations #1 and #6 in Table 5). The pressure gradient obtained from these two simulations is identical, confirming that at low Re the simulation results are unaffected when changing between the two LBM models. However, even changing to the Smagorinsky model did not allow to perform simulations for $Re \geq 10'000$ due to numerical instability and therefore the simulations listed in Table 5 are limited to Re $\leq 5'000$. Due to their slow convergence and high computational cost, these higher Re simulations were only performed for packings of tetrapods with $\Psi = 0.87$.

Table 5: LBM simulations of varying Reynolds number for a packing of tetrapods with $\Psi = 0.87$.

#	Inlet velocity u [m/s]	Reynolds number	LBM model	Resulting pressure gradient [Pa/m]
1	$5 \cdot 10^{-5}$	5	BGK	0.750
2	$5 \cdot 10^{-4}$	50	BGK	7.839
3	$5 \cdot 10^{-3}$	500	Smagorinsky	132.617
4	$4.9 \cdot 10^{-2}$	4900	Smagorinsky	6897.632
5	$5 \cdot 10^{-2}$	5000	Smagorinsky	7168.178
6	$5 \cdot 10^{-4}$	50	Smagorinsky	7.839

To determine the permeability from the simulations listed in Table 5 the Darcy-Forchheimer equation [Eq. (3.25)] was used to account for pressure losses due to turbulence which is captured by the quadratic term (k_{in}).

$$-\frac{dp}{dx} = \frac{v_w \rho_w}{k} u + \frac{\rho_w}{k_{in}} u^2 \qquad (3.25)$$

Here, $\frac{\partial p}{\partial x}$ is the pressure drop across the packing sample, ρ_w is the density of water, v_w is the kinematic viscosity of water. To determine the two unknowns k and k_{in} in Eq. (3.25) a system of linear equations is constructed:

$$\begin{bmatrix} v_w \rho_w u_1 & \rho_w u_1^2 \\ \vdots & \vdots \\ v_w \rho_w u_N & \rho_w u_N^2 \end{bmatrix} \begin{bmatrix} \frac{1}{k} \\ \frac{1}{k_{in}} \end{bmatrix} = \begin{bmatrix} -\frac{dp}{dx_1} \\ \vdots \\ -\frac{dp}{dx_N} \end{bmatrix} \qquad (3.26)$$

To test whether the permeability is independent of the Reynolds number, systems of equations [Eq. (3.26)] were constructed for all possible combinations (two or more) of simulations #1 to #5 listed in Table 5. This yielded 26 different linear equation systems. In case the systems were constructed from more than two equations, they were solved using the least squares method. The mean permeability calculated from these 26 linear equation systems is included in Figure 25 (error bar gives one standard deviation). Overall, there is an excellent agreement between the results of the LBM simulation for $Re = 5$ (discussed in section 3.6.5) and the result obtained for varying Re. Hence, the permeabilities k obtained numerically are independent of the Reynolds number, at least for the Re range investigated here.
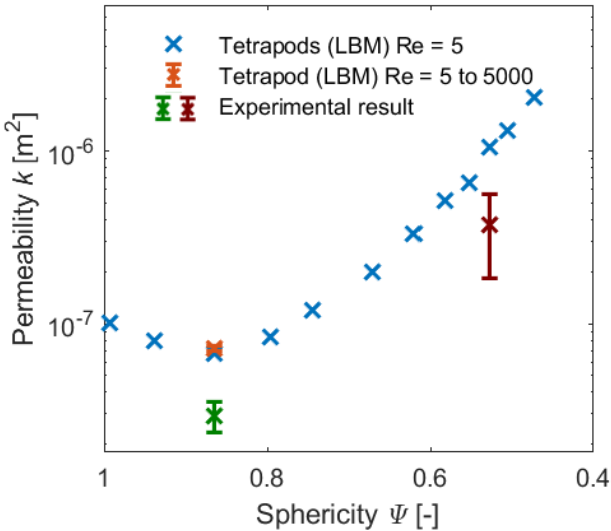

Figure 25: Permeability of packings of tetrapods of different sphericity. The orange cross gives the mean permeability of tetrapod

3.7   Conclusions

This work investigates packings of aggregates spanning a wide range of porosities, i.e. porosities $0.33 < \varepsilon < 0.78$. Three types of aggregates structures that is tetrapods, dolosse and tetrahedra are investigated numerically and validated experimentally using two types of tetrapods. The porosity of the packings was determined experimentally and by DEM revealing excellent agreement and providing further evidence for the predictive capabilities of DEM simulations. Importantly, our results show that the packing porosity cannot be predicted directly from the sphericity of the aggregates only, but it also depends on the convexity of the aggregates. The convexity of an aggregate was found to decrease monotonically with decreasing aggregate sphericity for all of the aggregate shapes investigated here. However, the rate of this monotonic decrease depends on the specific aggregate shape.

To investigate whether the aggregate shape affects the morphology of the pore structure, the tortuosity of the packing was determined. We observe that packings of aggregates of different shapes but similar sphericity do not form packings with a similar pore space morphology, as evidenced by a lack of a correlation between the aggregate sphericity and the tortuosity of the packings. Instead, for $\varepsilon > 0.35$ a linear correlation was found between the packing porosity and the tortuosity. For $\varepsilon < 0.35$ packings of tetrahedra were found to have very high tortuosity, when compared to tetrapods and dolosse. This was attributed to a face-to-face alignment of the closed tetrahedra aggregates. The linear correlation between

the tortuosity and the porosity, however, indicates that it is not required to introduce the tortuosity as an additional parameter to determine the permeability of a packing.

Finally, the permeability of the packing was investigated using the LBM and via falling pressure head experiments. The permeability values obtained agree well with the predictions of the Carman-Kozeny correlation, confirming its validity for a wide range of porosities. Since the Carman-Kozeny correlation only depends on the aggregate sphericity Ψ, ε and the aggregate diameter, information of a packing's tortuosity is not required to predict its permeability. Furthermore, we propose a correlation that relates the permeability of a packing directly to its porosity. This exponential correlation can be used to determine the permeability of packings of aggregates that are of similar equivalent diameter to the aggregates investigated here. It is hoped that the new insight into the packing of aggregates obtained through this work will pave the way for the development of noise absorbing facades, high permeability pavements for energy harvesting or the mitigation of local heat islands. Regarding the use of artificial aggregates for pavements, future work should consider also the compressive strength as well as the compactibility and workability of aggregate shapes.

4 Link between packing morphology and the distribution of contact forces and stresses in packings of highly nonconvex particles

Adapted from:

4.1 Abstract

An external load on a particle packing is distributed internally through a heterogeneous network of particle contacts. This contact force distribution determines the stability of the particle packing and the resulting structure. Here, we investigate the homogeneity of the contact force distribution in packings of highly non-convex particles both in two-dimensional (2D) and three-dimensional (3D) packings. A newly developed discrete element method is used to model packings of non-convex particles of varying sphericity. Our results establish that in 3D packings the distribution of the contact forces in the normal direction becomes increasingly heterogeneous with decreasing particle sphericity. However, in 2D packings the contact force distribution is independent of particle sphericity, indicating that results obtained in 2D packings cannot be extrapolated readily to 3D packings. Radial distribution functions (RDFs) show that the crystallinity in 3D packings decreases with decreasing particle sphericity. We link the decreasing homogeneity of the contact force distributions to the decreasing crystallinity of 3D packings. These findings are complementary to the previously observed link between the heterogeneity of the contact force distribution and a decreasing packing crystallinity due to an increasing polydispersity of spherical particles.

4.2 Introduction

Densely packed granular materials are frequently encountered in every-day life, for example, in civil engineering applications such as railway track ballast or porous asphalt pavements [143,144]. Such packings often undergo compaction either by forced compression or due to the material's own weight [145,146]. It has been well established that internal forces in

packed granular materials are not distributed homogeneously [74,147], but instead, forces are transmitted within the material through a network of so-called force chains. This force chain network traverses through the whole particle packing, but transmits forces through only a subset of the packed particles that are subject to above-average loads [72,148]. When exceeding a critical stress value in a force chain, buckling and/or slipping events can occur which result in large scale rearrangements of the packing [149,150]. Hence, the topology of the force chain network affects critically the structural stability of the packing [151].

Studies on force chains can be largely categorized into studies that consider (i) 2D packings [72,74], i.e. packings comprised of only one particle layer, or 3D packings [78,147] and (ii) packings that are compressed or sheared [72,74,78]. Compressed packings are obtained either by the uniaxial compression of particles in a rigid-walled container via a moving piston [62,78], or by its isotropic compression via two perpendicular walls [74,152]. To shear stress packings, various methods are used. For example placing particles in a rectangular confinement and compressing in one direction while expanding in another direction [74]. Numerically, packings may be sheared by compressing the packing vertically, while introducing a constant horizonal velocity to a frictional top wall and allowing a free horizontal movement of the particles [152,153].

In 2D packings, force chains were first qualitatively and later quantitatively probed by transmitting polarized light through a sheared packing of photoelastic discs, visualizing the stress in the discs in the form of fringes [72,73]. This method was extended by Liu et al. [147] to 3D packings by immersing

photoelastic beads in a liquid with a matching refractive index. It was found that the magnitude of the contact forces is distributed heterogeneously through the packing. To this date, there is no agreement on how to quantify force chains, but commonly the distribution of contact forces is quantified by the probability distributions of the contact forces [78,147,154]. For example, Liu et al. [147] placed carbon paper onto the inner surfaces of a container holding a particle packing. By calibrating the size of the imprints on the carbon paper against a known force they obtained the probability distribution ($P(f)$ with $f = F_n/<F_n>$) of the normal contact forces (F_n) normalized by the mean normal contact force ($<F_n>$). It was found that the probability of finding large normalized forces (i.e. $f > 1$) decays exponentially with increasing force magnitude. To explain this experimental observation, a theoretical model was proposed that assumes that the dominant mechanism which gives rise to force chains is governed by the heterogeneity of the granular packing, causing in turn, an unequal force distribution on the individual particles. It was observed further that $P(f)$ has a peak at $f = 1$ and that $P(f) \rightarrow 0$ for $f \rightarrow 0$. The shape of the observed probability distribution function of the contact forces resembles a characteristic shape commonly observed for disc- and sphere-shaped particles [62,78,147,153,154]. This characteristic shape is shown schematically in Figure 26 and labelled as type A, while the characteristic distribution labelled type B is, for example, observed in sheared packings of non-spherical particles [152,153]. A shortcoming of the carbon paper method is the difficulty to distinguish between beads that do not transmit a force and voids. This aspect was studied further by Mueth et al. [78] determining the fraction of contacts in compressed 3D packings that transmit forces that are sufficiently low to not leave an imprint on the carbon paper. Incorporating this additional information, Mueth et al. [78]

found that $P(f)$ has a saddle point at $f = 1$ and $P(f)$ increases for $f \to 0$ instead of approaching zero as proposed by Liu et al. [147]. Hence, for $f > 0.5$ the $P(f)$ as observed by Mueth et al. [78] has a concave shape that is characteristic of a distribution of type A, but combined with an increasing probability for $f \to 0$, that is characteristic for a type B distribution (Figure 26). The previous observation of Liu et al. [147] that $P(f)$ decays exponentially for $f > 1$ was confirmed by Mueth et al. [78].

Currently, there is no agreement on the mathematical function that describes $P(f)$ best. While some authors have argued that in a packing of spheres (type A shown in Figure 26) $P(f)$ can be fitted best by a Gaussian distribution [62,155], Mueth et al. [78] proposed Eq. (4.1) since a saddle point rather than a peak (at $f \approx 1$) was observed.

$$P(f) = a(1 - be^{-f^2})e^{-\beta f} \qquad (4.1)$$

In this equation a, b and β are fitting parameters. However, as shown in Figure 26, neither a Gaussian function nor Eq. (4.1) describe force distributions that have a type B shape. Nonetheless, it is generally agreed that for $f > 1$, $P(f)$ decays exponentially, independent of the domain dimensionality and particle sphericity. This observation motivated Azéma and Radjai [153] to propose the following fit to the tail ($f > 1$) of $P(f)$:

$$P(f) = e^{-kf}, \qquad f > 1 \qquad (4.2)$$

Here, the exponent k is a fitting parameter that will be used to quantify the length of the exponential tail of $P(f)$.

Majmudar and Behringer [74] further improved the quantification of the magnitude of contact forces by using photoelastic discs and acquiring high-resolution photographs

105

of 2D packings, allowing them to distinguish the individual interference fringes in the discs. Solving an inverse problem, which relates the number of fringes observed in a disk to the magnitude of the contact forces, the normal and tangential contact forces at each contact point were determined. Using this improved experimental technique, it was observed that in sheared packings fewer particles transmit large forces compared to compressed packings leading to more distinct force chains. Furthermore, it was shown that $P(f)$ in sheared and compressed packings of discs resembles a type A distribution with a peak at $f \approx 1$. However, the coefficient k of the exponential decay is smaller for sheared packings when compared to compressed packings.

Despite the continuous development and improvement of experimental techniques to visualize and quantify contact forces, it remains challenging to extract quantitative information of contact forces, in particular in 3D packings that are of high practical relevance. To address these challenges, the discrete element method (DEM) has established itself as an alternative to experimental approaches [156], providing detailed information on force networks in granular systems [80]. For example, Luding [154] used the DEM to investigate how the spatial stress distribution changes if polydispersity is introduced into packings of discs organized in a perfectly hexagonal lattice. For exactly monodisperse particle packings, particle stresses are distributed uniformly, in agreement with the hypothesis of Liu et al. [147]. However, as soon as polydispersity is introduced by varying the diameter (as little as ±0.33% of the mean diameter) a heterogeneous stress distribution, i.e. the occurrence of force chains, was observed [154]. Both experimental and numerical works [147,154] have established a link between the packing morphology and the

contact force distribution in packings of spherical particles. However, thus far, this link has not been investigated for non-spherical particles.

Among the non-spherical particle packings studied, those composed of highly non-convex particles are particularly interesting as non-convex particles can interlock, forming packings that may sustain compressive and tensile forces despite containing purely non-cohesive particles [62,120,157]. Owing to these particular characteristics, packings of highly non-convex, interlocking particles may find practical relevance, for example in architecture by enabling novel construction concepts such as aleatory construction [113,114,157,158]. However, despite their intriguing characteristics, so far, only a few studies have investigated the distribution of contact forces, $P(f)$, in packings composed of non-spherical particles. For example, Gan et al. [79] performed 3D DEM simulations of packings of oblate ellipsoids with their sphericity (Ψ) varying between 1 to 0.7. Interestingly, the $P(f)$ for ellipsoids was similar to the distribution of spheres, i.e. $P(f)$ peaks close to $f = 1$ and for $f > 1$ $P(f)$ decays exponentially (type A distribution). The exponential decay was fitted by Eq. (4.2) with k ranging between 1.2 and 1.4 depending on particle sphericity. However, there did not seem to be a clear correlation between the sphericity of the particles and the exponent k characterizing the decay. Similar results were reported by Saint-Cyr et al. [152] who simulated compressed packings of particle clusters composed of three discs glued together in a triangular arrangement (trimers). The sphericity of the trimer particles was varied between 1 and 0.76 by varying the overlap of the trimer particles. A key finding of their work was that in compressed packings of trimers, $P(f)$ resembles the distribution of spheres (type A) with an exponential decay (for $f > 1$) with

$k = 1.7$, independent of the particle sphericity, hence confirming the results of Gan et al. [79]. When the compressed trimer particles were also sheared (instead of only compressed), k decreased with decreasing sphericity (Ψ), i.e. k reduces from 1.7 to 1 for Ψ decreasing from 1 to 0.76. The behaviour of the reference case (discs with $\Psi = 1$) was different in that $P(f)$ was not affected by the addition of shear. Furthermore, Saint-Cyr et al. [152] showed that in sheared packings of spheres, the shape of $P(f)$ is concave and resembles a type A distribution. However, for non-spherical particles with $\Psi < 0.96$, $P(f)$ increases for $f \rightarrow 0$, leading to a type B distribution without a peak. Further, it was found that $\lim_{f \to 0} P(f)$ increased with decreasing sphericity. The decreasing value of k for decreasing particle sphericity and the absence of a peak at $f \approx 1$ leads to the key conclusion that in sheared packings $P(f)$ becomes increasingly heterogeneous for decreasing sphericity. The results of Saint-Cyr et al. were confirmed by Azéma and Radjai [153] in 2D simulations of sheared, half-disc-capped rectangular particles which resemble 2D spherocylinders. Azéma and Radjai [153] varied the sphericity of the particles from 1 to 0.82 and found the exponent k in $P(f) = e^{-kf}$ to decreases from 1.8 to 0.85, respectively. Moreover, they could also confirm that for particles with $\Psi < 0.99$ $P(f)$ resembles a type B distribution where $\lim_{f \to 0} P(f)$ increased for decreasing Ψ.

Highly non-convex particles of very low sphericity ($\Psi = 0.45$) (and spheres as a reference case) were studied by Murphy et al. [62]. The objective of their work was to find particle shapes that can form free-standing, externally unconfined, packings that can support load (i.e. searching for packings of interlocking particles that can sustain compressive and tensile stresses). Particles of low sphericity were modeled by gluing together multiple spheres to yield Z-shaped particles. For the

reference case, a 3D compressed packing of spheres, the well-established type A contact force distribution was observed, with a decay exponent of $k = 1.4$. However, compressed 3D packings of Z-shaped particles have a force distribution of type B, similar to the distributions observed by Saint-Cyr et al. [152] and Azéma and Radjai [153] in 2D sheared packings of non-spherical particles ($0.96 > \Psi > 0.76$). Additionally, the contact force distribution of Z-shaped particles ($\Psi = 0.45$) had a very long exponential tail with an exponent k ranging between 0.56 and 0.76 depending on the specific Z-shape.

From the above, one can conclude that in sheared 2D packings the exponential tail of the contact force distribution, $P(f)$, becomes longer with increasing particle non-sphericity, i.e. k decreases with decreasing Ψ. In addition the shape of $P(f)$ transitions from type A shape to a type B upon shearing [152,153]. However, in compressed 2D packings a decrease of k, as well as a change from a type A to type B distribution, with increasing particle non-sphericity does not occur for particles with $\Psi > 0.76$. Conversely, in compressed 3D packings of particles with $\Psi = 0.45$ a type B force distribution with $k \leq 0.76$ was observed. Hence, it remains still unclear whether (i) contact force distributions of type A prevail in compressed 2D packings of particles of low sphericity ($\Psi < 0.76$) and (ii) the contact force distribution of low sphericity particles ($\Psi < 0.76$) changes from a type A to type B distribution when transitioning from 2D to 3D packings.

In this work we address these two questions to establish a general correlation between particle sphericity and the shape of the contact force distribution in compressed 2D and 3D packings of non-spherical particles. While 2D packings do not occur in nature they are frequently studied, in particular

109

experimentally. To allow a comparison between the results of this work and previous experimental 2D and numerical 3D studies, packings of various dimensionality are studied here. In addition, we probe whether the conclusion drawn by Liu et al. [147] and Luding [154] for spherical particles, viz. that a more heterogeneous packing morphology leads to a longer exponential tail in the distribution function of the contact force, can be extended to non-spherical particle packings.
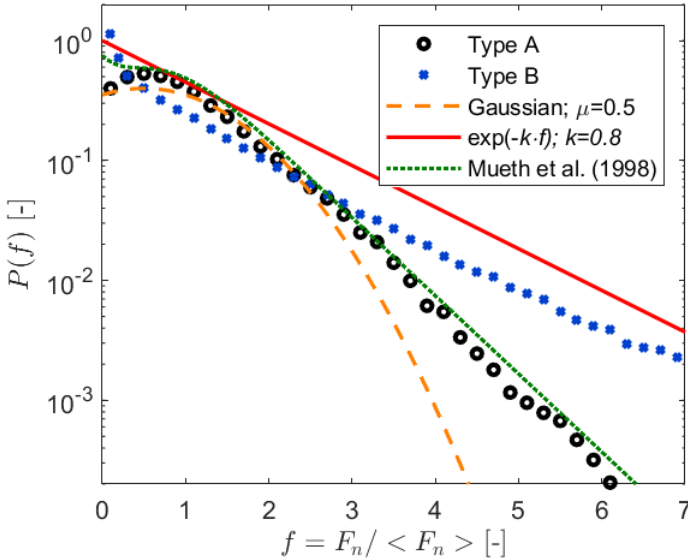
Figure 26: Probability distributions of f, i.e. the normal contact force (F_n) normalized by the mean normal contact force ($<F_n>$). Distributions of type A and B represent characteristic shapes that have been observed in various particle packings. The type A and type B distributions were obtained for 3D packings studied in this work. Specifically, a type A distribution was obtained for spheres and a type B distribution for star-shaped particles with a sphericity (Ψ) equal to 0.419.

4.3 Methods

The DEM algorithm used in this study is a modification of the original concept proposed by Cundall and Strack which was developed for disc-shaped particles [80]. The present work considers particles that are created by combining multiple spherocylinders (cylinders with hemispherically capped ends), analogous to the commonly applied glued-sphere approach [81]. A spherocylinder is a computationally benevolent particle shape since all points on its surface have the same distance from the central axis (see Figure 27). The general concept used in the DEM to track particles and particle contacts has been well documented in the literature [80,81,86,121,123,159,160]. Hence, the following will only describe the contact model and the contact detection algorithm between spherocylinders.

4.3.1 Particle contacts

Since all points on the surface of a spherocylinder have the same distance from the central axis (red dashed line in Figure 27), the contact detection for spherocylinders can be reduced to the task of finding the closest points between two line segments. We solve this task using the algorithm proposed by Lumelsky [87]. The point at which the contact forces act is called the contact point and corresponds to the center point (green point in Figure 27) of the line that connects the two closest points on each of the central axes (blue line in Figure 27). The normal contact force (F_n in Figure 27) acts perpendicular to the surface of the particle, while the tangential force (F_t), resulting from friction, acts parallel to the surface. The direction in which the tangential force acts depends on the

relative velocity of the particles at the contact point and the accumulated displacement between the particles.

If the angle between the central axes of the two contacting spherocylinders is less than two degrees, the contact is treated as a parallel contact (Figure 27b). The value of 2° is chosen as a feasible and efficient cut-off value based on additional numerical experiments. These experiments demonstrated that varying the cut-off angle between 0.01° and 5° does not affect the packing density nor the particle orientations. For a parallel contact, the middle of the parallel sections that align is chosen as the contact point (Figure 27b).
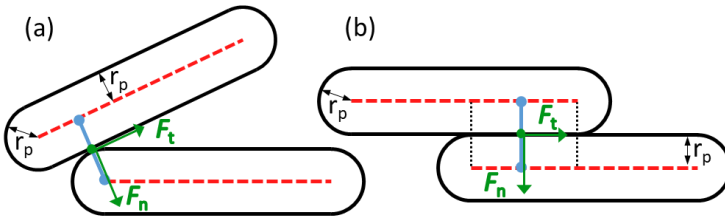

Figure 27: Schematic of two contacting spherocylinders. The red dashed lines denote the central axis of each spherocylinder. The spherocylinder radius is labelled r_p. The blue line depicts the shortest distance between the central axis of the two spherocylinders. F_n and F_t depict the normal and tangential forces acting at the contact point (green): a) contact between a cylindrical section and a hemispherical end cap, b) parallel contact between spherocylinders.

The contact between two particles is modeled by a linear spring-dashpot. The linear spring-dashpot model leads to a constant coefficient of restitution, independent of the collision velocity [161]. A linear model instead of a more realistic non-linear Hertzian model is justified as previous works have shown that packings of spherocylinders, when using either

linear or Hertzian contact models, did not differ in the probability distribution of the contact forces [88]. It has also been argued that the material stiffness should increase with increasing contact area, e.g. in the case of a parallel contact between two spherocylinders (Figure 27b) [89–91]. However, a recent study has shown that varying the contact stiffness in the case of parallel contacts has little influence on the force distribution and structure in packings of spherocylinders [88]. Consequently, in this work, the normal and tangential stiffness are assumed to be constant, regardless of the geometry of the contact.

The contact force in the normal direction, F_n, between two contacting particles i and j is:

$$F_n = \max\left(0, \quad \frac{k_n}{2}\delta_n - \eta_n\sqrt{2m_{ij}k_n v_n}\right) \qquad (4.3)$$

Here k_n is the normal stiffness of the particles, δ_n is the overlap between the contacting particles, η_n is the damping factor in the normal direction and v_n is the normal component of the relative velocity between the particles at the point of contact. The effective inertial mass m_{ij} is calculated by:

$$m_{ij} = \frac{m_i * m_j}{m_i + m_j} \qquad (4.4)$$

In the tangential direction (subscript t), the maximal contact force is limited by Coulomb's law of friction and is calculated by:

$$F_t = \min\left(\mu\frac{k_n}{2}\delta_n, \quad \frac{k_t}{2}\delta_t - \eta_t\sqrt{2m_{ij}k_t v_t}\right) \qquad (4.5)$$

where μ is the coefficient of friction, η_t is the tangential damping factor, k_t is the tangential stiffness and v_t is the tangential component of the relative velocity between the particles at the point of contact. The accumulated tangential displacement at the contact is calculated as $\delta_t = \int v_t\, dt$.

4.3.2 Simulation parameters

The density of the particles is fixed to $\rho = 1000$ kg/m^3 which is close to the density of many plastics, e.g. polyethylene (PE) or acrylonitrile butadiene styrene (ABS). Such plastics are commonly used in manufacturing techniques such as injection molding or fused deposition modelling, which can be employed to manufacture non-spherical particles. To choose a value for the normal particle stiffness k_n two competing factors have to be considered: One factor is that a decreasing k_n leads to a larger time step dt which decreases the computational time. As a rule of thumb dt should be at least 20 times smaller than the duration of a collision t_{col} which can be approximated by a damped harmonic oscillator [125]:

$$t_{col} = \frac{\pi}{\sqrt{\dfrac{k_n}{m_{ij}}(1 - \eta_n{}^2)}} \qquad (4.6)$$

Furthermore, particles in a packing experience the weight of the particles above them which can lead to a vertical gradient of the magnitude of the contact forces. The influence of this gradient on the contact force probability distribution needs to be considered. Some researchers have eliminated the influence of this gradient by normalizing the contact forces by the weight of the particles above a given depth in the packing [147]. In our

work a different approach is used to eliminate the effect of the vertical gradient in the magnitude of the contact forces that is by exerting an additional vertical load onto the packing through a forced compression at the top. If the contact forces due to the external compression are sufficiently high, the influence of the vertical gradient can be neglected. However, increasing the contact force between particles, without changing the stiffness, increases the overlap δ_n between the particles which can lead to computational stability problems. Hence, a sufficiently high k_n is desired to be able to neglect the vertical gradient in the magnitude of the contact forces. For the given particle density of $\rho = 1000$ kg/m^3 an external compression force of 500 N was found, through simulations, to be sufficient to eliminate the influence of the vertical gradient in the magnitude of the contact forces. For an external compression force of 500 N a normal particle stiffness k_n of 100'000 N/m is required to limit the particle overlaps to $\delta_n < 0.05 \times d_p$, where d_p is the spherocylinder diameter. Additional simulation results show that increasing k_n by an order of magnitude does not influence the contact force distributions; decreasing k_n by an order of magnitude while keeping the compression force constant leads to unstable simulations. In conclusion, any set of values for the parameters ρ, k_n, dt and the compression force can be chosen, without affecting the results, as long as the set satisfies the conditions outlined above.

The damping factor in the normal direction η_n is assumed to be constant and is related to the coefficient of restitution e via:

$$e = exp \left(\frac{-\pi \eta_n}{\sqrt{1 - \eta_n^2}} \right) \qquad (4.7)$$

In this work, $e = 0.53$ ($\eta_n = 0.2$) is chosen as previous studies have shown that varying e in the range $0.2 - 0.9$ has little influence on the behaviour of dynamic granular systems such as rotating drums and flows down an inclined plane [82,162]. We expect the influence of e on the results of a static granular packing to be even less significant than for dynamic systems. For the tangential stiffness $k_t = 0.5 \times k_n$ is chosen in accordance with previous works [121,160,163], while for the friction coefficient a value of $\mu = 0.5$ is chosen. A discussion about the influence of particle friction on the contact force probability distribution can be found in chapter 4.4.3.

Friction at the domain walls is neglected by setting the coefficient of friction between particles and the domain walls to $\mu_w = 0$, as some authors [164] have argued that friction between particles and the domain wall leads to a more heterogeneous particle packing. The influence of a frictional wall on a packing is most pronounced close to the wall. In the work reported here, the dimensionality of the domain is varied. Hence, to isolate the effect of dimensionality on a particle packing, the effect of wall friction has to be eliminated. Furthermore, other numerical works on non-spherical particles [62,152] have also chosen to neglect wall friction. For these reasons wall friction is also neglected in this work. Of course, frictionless walls are typically not observed in experiments. To aid comparison with experimental work the influence of the wall friction on the particle packing is discussed in chapter 4.4.4.

Table 6 summarizes the values of the parameters used in the simulations. The value of the parameters of the confining walls are identical to those of the particles, except for the friction coefficient.

Table 6: Material parameters used in the simulations

Parameter	Symbol	Value
Density	ρ	1000 kg/m^3
Normal stiffness	k_n	100'000 N/m
Tangential stiffness	k_t	50'000 N/m
Coefficient of restitution	e	0.53
Normal damping factor	η_n	0.2
Tangential damping factor	η_t	0.2
Coefficient of friction	μ	0.5
Wall friction coefficient	μ_w	0
Spherocylinder diameter	d_p	0.005 m
Time step	dt	$2 \cdot 10^{-6}$ 1/s

4.3.3 Cluster particles

The combination of several spherocylinders to spherocylinder-cluster particles, analogous to the glued sphere approach [81,90], does not require additional contact detection routines [81]. The contact between two cluster particles can be treated as a contact between individual spherocylinders. The contact forces acting on the different spherocylinders belonging to a cluster are summed up and act on the center of gravity of the cluster.

In this study, two different types of cluster particles are investigated. In 2D packings, cross-shaped particles are used (Figure 28a-e). Cross-shaped particles are formed by intersecting two perpendicular spherocylinders of equal length in their centers. In simulations of pseudo-2D and 3D packings, star-shaped particles (also referred to as jacks or hexapods) are used. Such particles are formed by intersecting a cross-shaped particle with a third spherocylinder (of the same length) perpendicular to both spherocylinders that form the cross

(Figure 28f). These particle shapes are chosen as they model non-convex geometries with a high order of symmetry and are easy to construct.

The non-convexity of cross- and star-shaped particles increases with decreasing sphericity (Ψ). Various definitions for sphericity have been proposed [60,65,127], whereby the most common definition is the ratio of the surface area of a sphere to the surface area of a non-spherical particle with the same volume as the sphere [60,165,166]. The present work uses this definition and thus for a sphere $\Psi = 1$ and for non-convex particles $\Psi < 1$. The sphericity of the particle shapes modeled in this work ranges from $\Psi = 0.99$ to 0.42, hence covering a broad range of shapes from almost sphere-like to very slender highly non-convex shapes (Figure 28e).

Some authors [45,135] have argued that several parameters, such as sphericity, blockiness and convexity, have to be specified to distinguish between different non-spherical particle shapes. We agree with the general rationale behind this proposal, however, this work investigates only two different shapes of particles, i.e. cross-shaped and star-shaped particles. For these two particle shapes any non-sphericity-describing parameter, e.g. blockiness or convexity, scales monotonically with (non-)sphericity. We believe that due to this monotonic scaling, the introduction of a second non-sphericity parameter would be redundant, provided that particles of one shape are compared only to particles of the same shape (as is the case of this study). An exception is made for the particle aspect ratio (defined as the ratio of the overall length of a particle L to the diameter of the protruding arms d_p (Figure 28)) which was used by other works [120,157] to describe star-shaped particles. To aid the comparison between our work and works [120,157] the

relationship between the particle aspect ratio and the particle sphericity is given in Table 7.
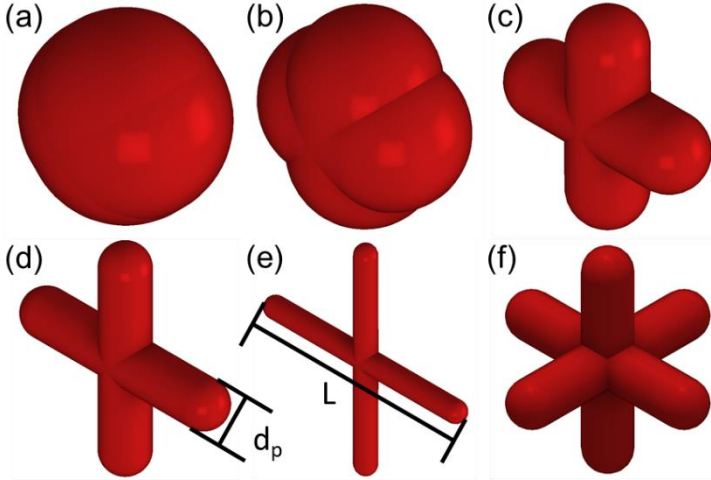

Figure 28: Selection of cross- and star-shaped particle geometries with varying sphericities (Ψ): a) Cross-shaped particle with $\Psi=0.99$, b) cross-shaped particle with $\Psi=0.96$, c) cross-shaped particle with $\Psi=0.75$, d) cross-shaped particle with $\Psi=0.59$, e) cross-shaped particle with $\Psi=0.47$ and f) star-shaped particle with $\Psi=0.53$.

Table 7: Relationship between the particle aspect ratio and the particle sphericity. The particle aspect ratio is defined as the overall length of a particle (L) and the diameter of the protruding arms (d_p).

Particle aspect ratio (L/d_p)	Sphericity cross-shape (2D)	Sphericity star-shape (3D)
1.1	0.995	0.995
1.7	0.933	0.933

2.25	0.842	0.809
3	0.754	0.702
4	0.677	0.619
6	0.585	0.526
8.5	0.518	0.462
11	0.473	0.419

4.3.4 Simulation domains

Four different domain configurations (defined by the confining walls) are assessed in this work: (i) 2D simulations in which cross-shaped particles cannot move in the z-direction (coordinate system shown in Figure 29). In these 2D simulations the domain width W_{dom} (x-direction) is equal to 30 times the particle length L. Therefore, W_{dom} changes with particle shape Ψ; (ii) Pseudo-2D simulations in a cuboidal domain with a transverse thickness T (z-direction) equal to L. As in the 2D simulations, $W_{dom} = 30 \times L$; (iii) Pseudo-2D simulations in a cuboidal domain with $T = 2 \times L$ and $W_{dom} = 30 \times L$ and (iv) 3D simulations in a cylindrical domain of diameter $D_d = 10 \times L$. A visualization of the pseudo-2D simulation with $T = 2 \times L$ is given in Figure 29a.

For 3D domains two diameters D_d are investigated, i.e. $D_d = 6 \times L$ and $D_d = 10 \times L$; for these two domain sizes very similar results are obtained for the contact force distributions. To have a larger data set for the contact force distributions, the results of the larger 3D domain ($D_d = 10 \times L$) are presented in the following. For the pseudo-2D domain, a transverse thickness of $T = L$ is chosen; this thickness is as close as possible to a 2D domain while still allowing rotations around any given axis of the star-shaped particles. To investigate how a change in the transverse thickness affects the structure of the packing and

transmission of contact forces, pseudo-2D domains with $T = 2 \times L$ are simulated. As the results of the pseudo-2D domains with $T = 2 \times L$ are similar to the 3D results, T is not increased further.

To initialize a simulation, the domain is filled by placing all of the particles on a regular lattice with a space of $1.5 \times d_p$ between each particle. The height of the simulation domain (y-direction) is chosen just large enough to accommodate all of the particles in the initialization lattice. The particles are initialized with a random rotational orientation and a random velocity v (-0.25 m/s $< v <$ 0.25 m/s) in the y- and z-directions (2D and $T = L$ cases) or a random velocity in all three directions (3D and $T = 2 \times L$ cases). The particles are allowed to settle for a time $t_{settle} = 3 * \sqrt{2h/g}$, where g is the acceleration due to gravity and h is the domain height. After time t_{settle}, the particles have come to rest as the average displacement of the particles per time-step approaches numeric precision. Once the particles have settled, the domain is compressed by moving a planar wall from the top downwards with a speed of 0.25 m/s until the packing exerts the external compression force of 500 N onto the top wall. This procedure simulates the uniaxial compression of a granular material in a container with rigid walls.

The number of particles in each simulation N is such that the height of the packing (after compression) is at least twice as high as W_{dom} (or in the case of a cylindrical domain the diameter of the cylinder). In the different configurations N ranges from 1800 to 34500.

To avoid crystallization at low values of Ψ, a particle size distribution, is introduced. In 2D simulations, the polydispersity factor (by which the particle size is scaled) is

± 0.3 for $\Psi > 0.88$, and ± 0.15 for $0.88 \geq \Psi > 0.75$. For pseudo-2D and 3D simulations, the polydispersity factor is ± 0.2 for $\Psi > 0.86$. As reference cases, packings of spherical particles (diameter $d_p = 0.005$ m, polydispersity factor ± 0.2) in a 2D domain with $W_{dom} = 30 \times d_p$ and in a cylindrical domain with a cylinder diameter of $10 \times d_p$ are simulated.

4.3.5 Data analysis: Contact forces, stress analysis and packing structure

Previous studies using spherical particles typically focused on the normal component of the contact force [62,78,152]. Thus, we likewise report here the distribution of the normal contact forces. For the computation of the probability distribution of the contact forces, $P(f)$, the normalized forces f are sorted into 50 bins of size 0.2 (range 0-10).

Particle stresses are obtained by calculating first the stress tensor of the individual particles according to [167]:

$$\bar{\bar{\sigma}} = \frac{1}{V}\begin{bmatrix} \sigma_{xx} & \sigma_{xy} & \sigma_{xz} \\ \sigma_{yx} & \sigma_{yy} & \sigma_{yz} \\ \sigma_{zx} & \sigma_{zy} & \sigma_{zz} \end{bmatrix} = \frac{1}{V}\sum_c \bar{F}_{n+t}^c \bar{r}^c \qquad (4.8)$$

where V is the particle volume, c is the number of all particle contacts, $\bar{F}_{n+t}$ is the sum of the normal contact force and the tangential contact force and $\bar{r}$ is the vector pointing from the center of the particle to its contact point. The particle stress tensor is diagonalized to obtain the principal stresses. Additionally, this work reports the sum of the elements of the diagonalized stress matrix (trace) of each particle, i.e. the first stress invariant of the tensor for each particle ($I_{1,i}$). Similar to

the presentation of the contact forces $I_{1,i}$ is normalized by its mean $(< I_1 > = \frac{1}{N}\sum_i^N I_{1,i})$ yielding $i = I_{1,i}/<I_1>$.

The packing morphology is analyzed by calculating the radial distribution function (RDF) which is given by Eq. (4.9). The RDF can be interpreted as the number of particles that are located in a differential volume shell (thickness Δr) with a distance r from the particle center, divided by the expected number of particles based on the particle number density of the whole packing. Here the center of mass of a cross- or star-shaped particle is considered as the particle center. The RDF plots show $G(r)$ over r/L, where r has been normalized by the respective particle length L.

$$G(r) = \frac{N_{RDF}(r)}{4r^2 \Delta r N \rho_N} \qquad (4.9)$$

In Eq. (4.9) ρ_N is the average number density of the particles (number of particles in the simulation domain divided its volume) and N_{RDF} is the number of particles in the differential volume shell given by:

$$N_{RDF} = \sum_i^{N_{10L}} \sum_{j \neq i}^{N} \delta(r - r_{ij}) \qquad (4.10)$$

where δ is the Dirac delta function, r_{ij} is the distance between the center of particle i to the center of particle j and N_{10L} is the number of particles which have a distance of at least $10 \times L$ from each side wall as well as the top and bottom of the 2D domain. This area is sketched in Figure 29b. In the 3D case, N_{10L} corresponds to the number of particles that have at least a distance of $10 \times L$ from the top and bottom wall and a distance

of $3 \times L$ from the cylinder wall. We exclude particles close to the wall because these particles have no close neighbors outside of the walls.
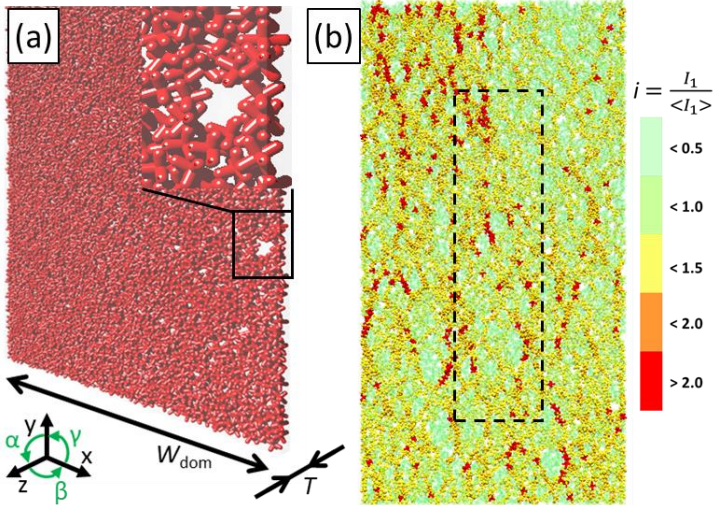

Figure 29: a) Visualization of a pseudo-2D packing of star-shaped particles ($\Psi = 0.619$) with $W_{dom} = 30 \times L$ and $T = L$ (L = particle length). b) Visualization of the normalized, first stress invariant ($i = I_{1,i}/\langle I_1 \rangle$) of the packing shown in (a). The dashed area depicts the area which is used to calculate the radial distribution function (RDF). The results of the RDF are shown in Figure 36.

4.4 Results and discussion

4.4.1 Solid fraction

Particles of low sphericity form packings with a low solid fraction. Figure 30 plots the solid fraction of a packing as a function of Ψ and domain geometry. For 2D packings, we show the area fraction occupied by particles as well as the volume

fraction, assuming that the domain has a transverse thickness that is equal to the particle diameter ($T = d_\mathrm{p}$).

For a packing of non-spherical particles ($\Psi > 0.9$), one observes an increase in solid fraction with decreasing sphericity, with a peak at $\Psi = 0.9$ - 0.95. At this sphericity value, the particle shapes are the closest to a cuboidal shape. Cuboids can be stacked without any gaps. Reducing the sphericity further ($\Psi \leq 0.9$), the particles become increasingly concave with an increased tendency to interlock, which leads to a decreasing solid fraction of the packing. The shape of the solid fraction versus sphericity curves is similar to the trends that have been observed previously simple spherocylinders and ellipsoids [41,168,169].
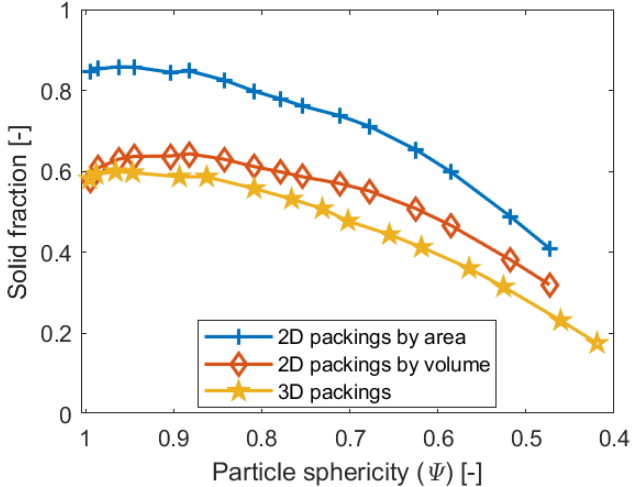

Figure 30: The solid fraction of packings as a function of sphericity and domain geometry.

125

4.4.2   Contact force distributions

As a first approach, we assess whether our simulations support a previously reported trend that the exponential tail of $P(f)$ becomes longer for increasingly non-spherical particles [62,79,152,153]. Currently, it is unclear whether such a trend is limited to a given domain dimensionality (2D vs 3D) and whether compressed packings show the same behavior as sheared systems. Figure 31 plots the probability distributions of the normal contact forces normalized by their mean, $P(f)$, for different particle sphericities and domain configurations.

For 2D domains, the $P(f)$ of cross-shaped particles with the highest investigated sphericity ($\Psi = 0.995$) and spheres are very similar (Figure 31a). In 2D packings, changes in the $P(f)$ when transitioning from packings of spherical particles to slightly non-spherical particles seem to occur gradually. Figure 31a also plots Eq. (4.1), the numerical expression for $P(f)$ proposed by Mueth et al. [78]. Somewhat surprisingly, the empirical Eq. (4.1), although extracted originally from a packing of spheres agrees well with the data for low sphericity cross-shaped particles in 2D, but not with the simulation results of spheres. A possible reason for this deviation might be the fact that Mueth et al. [78] studied 3D packings and only recorded contact forces at the wall. Indeed, the numerical results of a packing of spheres in a 3D domain, Figure 31d, agree very well with Eq. (4.1).

When comparing the contact force distribution, $P(f)$, of cross-shaped particles (2D domain) as a function of their sphericity (Figure 31a), one can observe that the length of the exponential tail of $P(f)$ increases with decreasing Ψ. However, the increase in the length of the exponential tail is limited. Even in packings

of cross-shaped particles with a sphericity of $\Psi = 0.473$ (lowest sphericity modeled) only four individual contact forces (out of 10^5) have a value of $f > 8$. The general type A shape of the distributions, i.e. a peak at $f \approx 1$ and an exponential tail is independent of particle sphericity when the packing is restricted to 2D. Hence, our results confirm the observations by Saint-Cyr et al. [152] who modeled trimers ($1 \geq \Psi \geq 0.76$) and observed that the shape of $P(f)$ and the location of its peak is independent of particle sphericity in compressed 2D packings.

Turning now to pseudo-2D packings of star-shaped particles (Figure 31b and Figure 31c for, respectively, $T = L$ and $T = 2 \times L$), one observes a change in the shape of $P(f)$ from type A to type B with decreasing particle sphericity. Generally, the peak at $f \approx 1$ becomes less pronounced and the length of the exponential tail increases with decreasing sphericity. Only for particles with the highest sphericity ($\Psi = 0.995$) the shape of $P(f)$ in pseudo-2D packings coincides with the shape that is observed in 2D simulations.

When increasing the transverse thickness of the pseudo-2D simulations ($T = 2 \times L$, Figure 31c) and ultimately reaching full 3D simulations, Figure 31d, the shape of $P(f)$ changes further, i.e. the peak of $P(f)$ remains at $f \approx 1$ for high-sphericity particles but is no longer visible for low-sphericity particles ($\Psi = 0.461$ and $\Psi = 0.419$). Furthermore, the length of the exponential tail increases significantly for $\Psi < 0.7$ when increasing the transverse thickess of the domain to $T = 2 \times L$ and 3D. It has been suggested that type A distributions are essentially Gaussian-like (centered around $f \approx 1$, albeit truncated at $f = 0$) which would indicate that the forces are distributed homogeneously [62,155]. The similarity between a type A distribution and a Gaussian-shaped distribution is shown in

Figure 26. One can see that a Gaussian is a good fit for type A distributions for $f < 3$, but the type A distribution has a longer tail. On the other hand, the lack of a peak at $f \approx 1$ and the long exponential tails of type B distributions represent a heterogeneous force distribution with a large number of below-average contact forces but also some contact forces that are ten times above average.
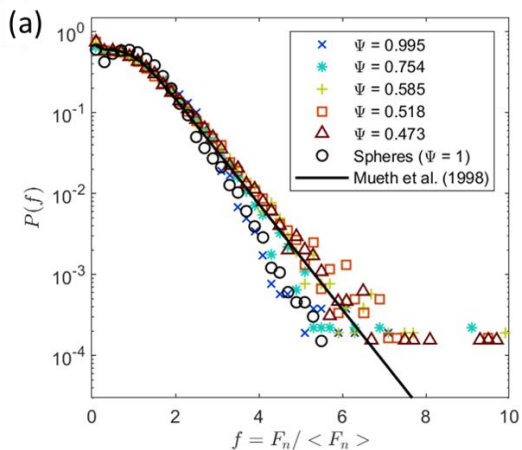
To summarize, our results show that in pseudo-2D and 3D packings the shape of $P(f)$ changes from type A to a type B when the particle sphericity decreases below the critical value $\Psi_{crit} = 0.7$ (but not in 2D packings). The shape change comes with an increasing length of the exponential tail of $P(f)$ and a decreasing prominence of the peak at $f \approx 1$ with decreasing particle sphericity. Our results connect for the first time the observations of several previous studies: Saint-Cyr et al. [152] and Azéma and Radjai [153] who observed exclusively type A distributions in compressed 2D packings of non-spherical particles. On the other hand, Gan et al. [79] who simulated ellipsoids with $\Psi \geq 0.7$ in 3D packings observed type A distributions and Murphy et al. [62] who simulated Z-shaped particles with $\Psi = 0.45$ in 3D packings observed type B distributions.
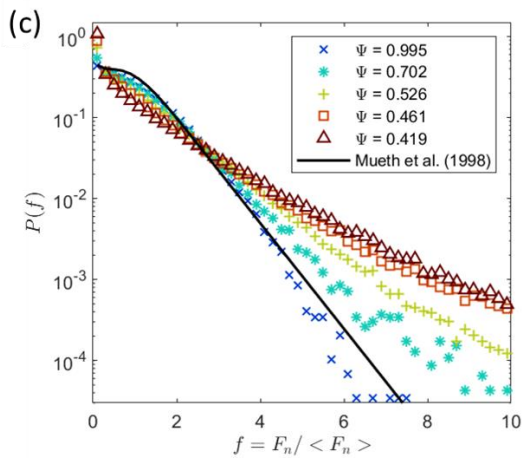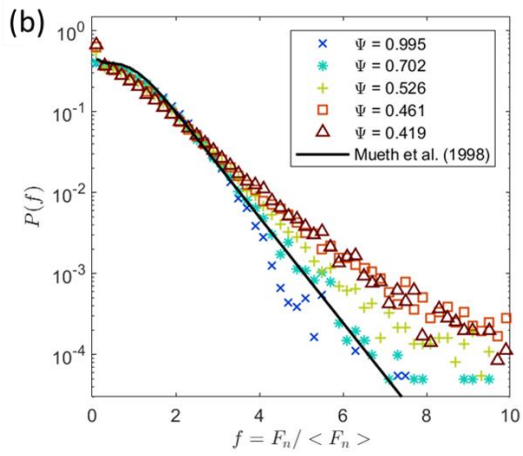
Combing the results of our simulations with previously reported observations allows us to draw the following general conclusion for the shape of $P(f)$ in 2D and 3D packings of compressed non-spherical particles with different shapes and sphericities:

- With decreasing particle sphericity, the contact force distribution of compressed 3D packings becomes more heterogeneous. This is evidenced by the increasing length of the exponential tail of the contact force distribution with

decreasing particle sphericity for $\Psi < \Psi_{crit} = 0.7$, independent of the specific particle shape.

- In compressed 2D packings the length of the exponential tail of the contact force distributions does not depend on particle sphericity.

(a)

Legend:
- $\times$ $\Psi = 0.995$
- $*$ $\Psi = 0.754$
- $+$ $\Psi = 0.585$
- $\square$ $\Psi = 0.518$
- $\triangle$ $\Psi = 0.473$
- $\bigcirc$ Spheres ($\Psi = 1$)
- —— Mueth et al. (1998)
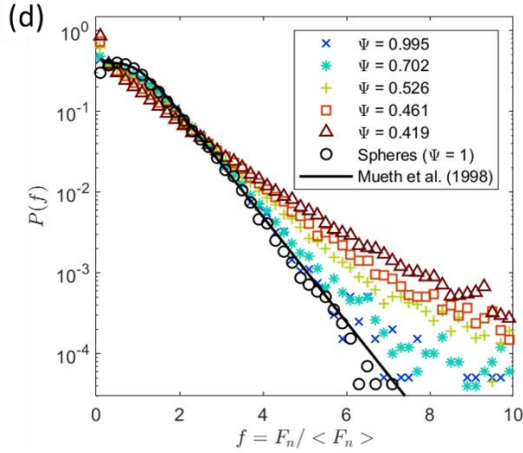
Axis labels: $P(f)$ (vertical), $f = F_n/ < F_n >$ (horizontal)

Figure 31: *Probability distribution functions, P(f), of the normal contact force (Fn) normalized by the mean normal contact force (<(Fn)>) for all four packing domains simulated. In the 2D domain (a) the flat, cross-shaped particles can only translate in the x- and y-directions. In the pseudo-2D domains (b) three-dimensional particles can translate in all three directions, with the transversal domain width T in the z-direction being as large as the particles (T = L). In the second pseudo-2D domain (c) the z-direction is twice as large as the particles (T = 2 × L). The 3D domain (d) is cylindrical with diameter Dd = 10 × L. For each packing configuration the full range of particle sphericities simulated is shown. For reference a 2D simulation of spheres is included in (a) and a 3D simulation of spheres is included in (d). Each panel also plots the probability distribution function predicted by the empirical equation (Eq. (4.1)) of Mueth et al. [78], which was derived from compressed 3D packings of glass spheres.*

4.4.3 Influence of particle friction

The following section discusses the influence of the interparticle friction coefficient μ on the probability

131

distribution of the contact force $P(f)$. Throughout all other parts of chapter 4 of this work $\mu = 0.5$ was used.

Figure 32a plots $P(f)$ for cross-shaped particles with the highest ($\Psi = 0.995$) and lowest ($\Psi = 0.518$) sphericity in a 2D domain for varying μ. For both $\Psi = 0.995$ and $\Psi = 0.518$, P(f) is not affected appreciably by the friction coefficient.

Figure 32b plots $P(f)$ for star-shaped particles in a 3D domain (cylinder with a diameter $D_d = 6 \times L$). For the highest sphericity ($\Psi = 0.995$), P(f) is independent of μ. For the lowest sphericity ($\Psi = 0.461$), the P(f) for $\mu = 0.5$ and $\mu = 0.9$ coincide ($\mu = 0.5$ was used in the throughout chapter 4 of this work). However, for particles with $\Psi = 0.461$ and $\mu = 0.1$, P(f) has a shorter tail compared to P(f) for higher values of μ, indicating that there is a minor influence of μ on $P(f)$. A reason for this observation may be that it is less likely for low friction particles to obtain configurations in rotationally jammed configurations. Instead, such low-friction particles are more likely to arrange themselves into the closest crystalline configuration which would be represented by a shorter exponential tail.
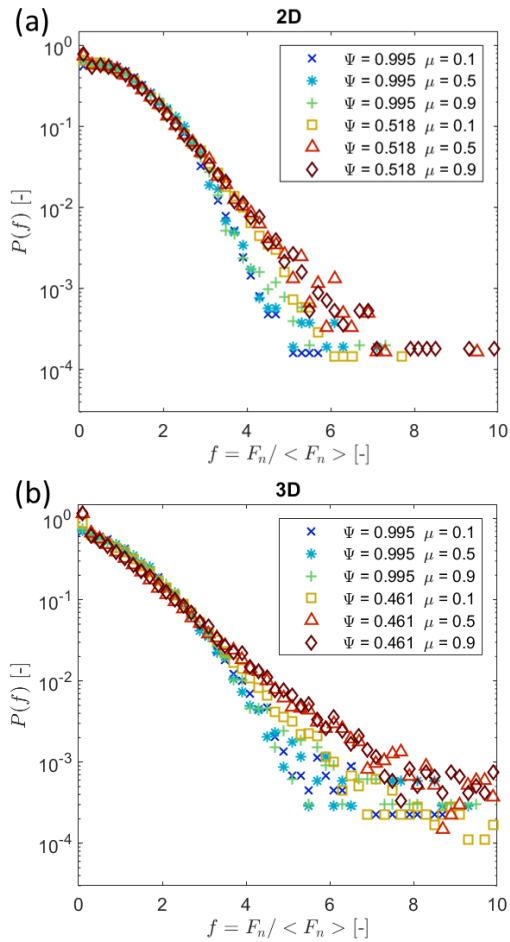
Figure 32: Probability distribution functions, P(f), of the normal contact force (F_n) normalized by the mean normal contact force ($<(F_n)>$) for varying inter-particle friction coefficients μ. The 2D data (a) uses flat cross-shaped particles, the pseudo-2D and 3D data (b) uses star-shaped particles.

Figure 33 probes further the influence of a low friction coefficient ($\mu = 0.1$) on $P(f)$. For star-shaped particles with $\Psi = 0.461$ in a 3D domain, the exponential tail of $P(f)$ is longer than for particles with $\Psi = 0.995$ in a 3D domain or any $P(f)$ in a 2D domain. Hence, the general trends observed throughout chapter 4 of this work are not affected by a varying μ, i.e. in 3D packings the length of the exponential tail increases with decreasing particle sphericity independent of μ.
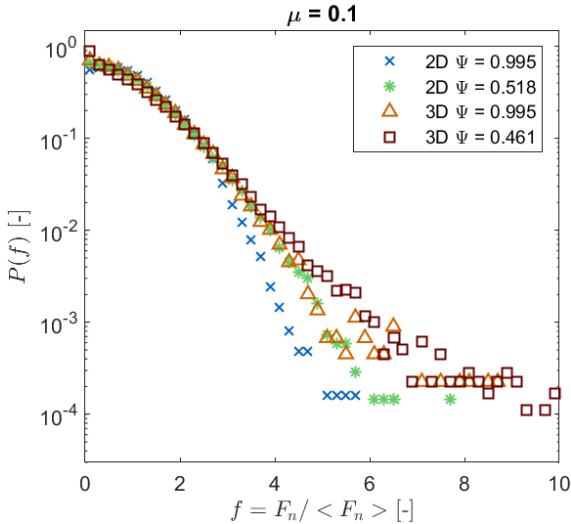

Figure 33: Probability distribution functions, P(f), of the normal contact force (F_n) normalized by the mean normal contact force ($<(F_n)>$) for an inter-particle friction coefficient $\mu = 0.1$. The particle sphericities plotted are the highest and lowest sphericities that have been considered in this work.

4.4.4 Influence of wall friction

Friction between the particles and the domain walls is disregarded in this work to aid comparisons with previously reported numerical works of non-spherical particles [62,152]. In addition, other authors [164] have argued that introducing wall friction leads to more heterogeneous particle packings. In the following the influence of the wall friction coefficient μ_w on the probability distribution function of the normal contact force $P(f)$ is assessed. An understanding of how μ_w influences $P(f)$ will aid the comparison between experimental works and our numerical study.

Figure 34 plots $P(f)$ for varying μ_w for particles with the highest sphericity parameter simulated in this work ($\Psi = 0.995$). For 2D simulations, W_{dom} (x-direction) is equal to 30 times the particle length L; while pseudo-2D and 3D simulations ar executed in smaller domains than the main body of the work to reduce computational time. Figure 34 b plots the results obtained in a cuboidal domain with a transverse thickness T (z-direction) equal to L and $W_{dom} = 16 \times L$ (in the all other parts of chapter 4 $W_{dom} = 30 \times L$). Figure 34c plots the results obtained in pseudo-2D domains with $T = 2 \times L$ and $W_{dom} = 16 \times L$ ($W_{dom} = 30 \times L$ in the main body of this work). Figure 34d plots the results obtained in a 3D cylindrical domain with $D_d = 6 \times L$ ($D_d = 10 \times L$ in the main body of this work).

The results given in Figure 34a show that in a 2D domain $P(f)$ does not vary appreciably with μ_w. This is not unexpected as in a 2D domain particles have only contact with the side walls in the x-direction (comparatively large dimension of the domain in the x-direction with $W_{dom} = 30 \times L$). Hence, the domain width is sufficiently large to ensure frictional walls do not influence the packing. For pseudo-2D domains the shape of $P(f)$ changes;

135

i.e. a longer exponential tail is observed when wall friction is introduced. In a pseudo-2D packing, particles have (frictional) contacts with the side walls in the x-direction ($W_{dom} = 16 \times L$) and in the z-direction; however, the domain size in the z-direction is very small with $T = L$ (Figure 34b) and $T = 2 \times L$ (Figure 34c). Therefore, in pseudo-2D domains with $T = L$ every particle has a contact with at least one frictional wall and for $T = 2 \times L$ the majority of particles has at least one contact with a frictional wall. Due to the additional tangential contact forces between particles and frictional walls, it is more likely that particles become jammed during compression. These jammed particles cannot rearrange to distribute the contact forces more homogeneously. Interestingly, the exponential tails seem to be longer for $T = L$ than for $T = 2 \times L$. This can be explained by the fact that particles can barely move in the z-direction for $T = L$, while in a $T = 2 \times L$ domain two particles fit side-by-side in the z-direction and depending on their orientation a small gap can exist between the two particles into which a particle can wedge from above. Such a configuration would increase the normal forces between particles and the walls and consequently also the (limiting) tangential force that is given by Coulombs law. In a 3D domain (Figure 34d) the influence of frictional walls on P(f) is noticeable that is a longer exponential tail when introducing frictional walls. However, the influence of frictional walls in 3D domains is less pronounced than in pseudo-2D domains, since the diameter of the cylindrical domain is $D_d = 6 \times L$ and therefore less particles are in contact with the frictional wall when compared to the pseudo-2D domains. One can expect that if the diameter of the 3D domain is increased further the influence of the frictional walls on P(f) will decrease further. Additionally, the magnitude of μ_w does not seem to affect P(f) as long as $\mu_w > 0$.
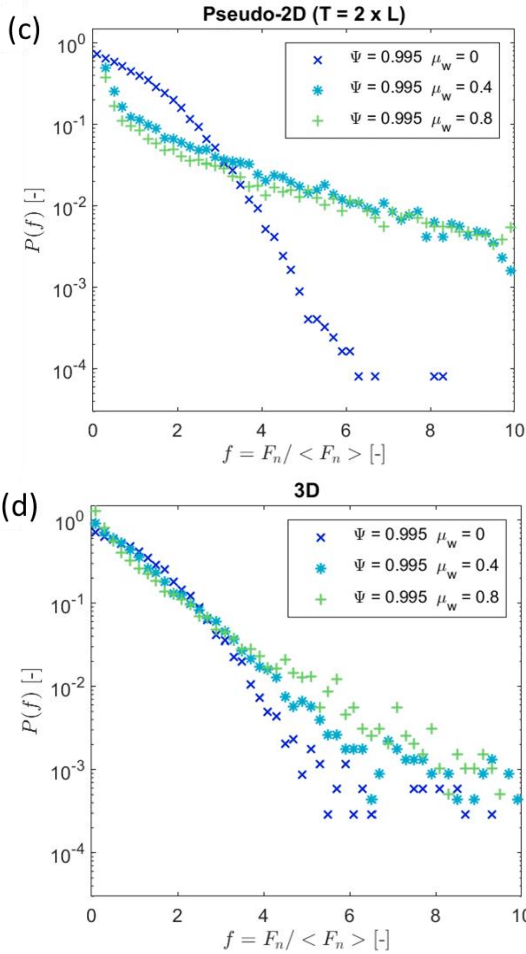
2D

(a)

Pseudo-2D (T = L)

(b)
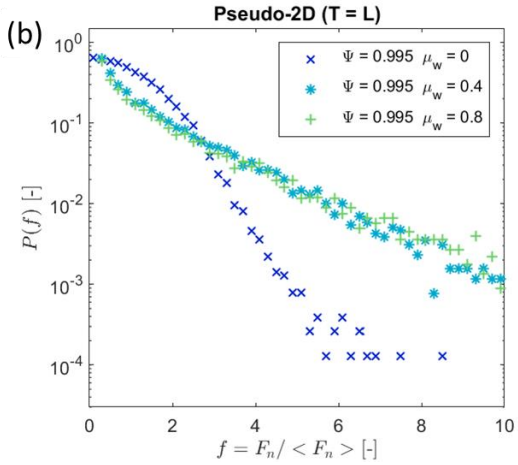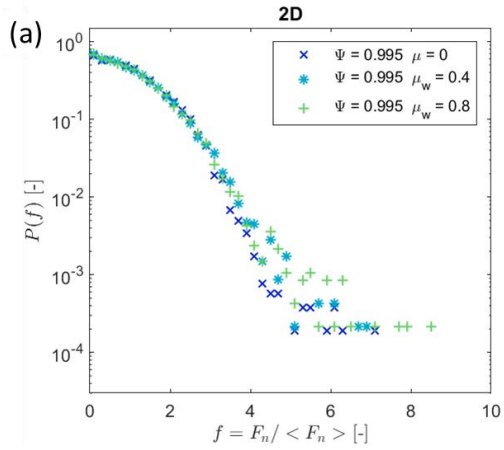
Figure 34: Probability distribution functions of the normal contact force, P(f) normalized by the mean normal contact force (<(F_n)>) as a function of the wall friction coefficient μ_w: (a) 2D domain, (b) pseudo-2D domain (T = L), (c) pseudo 2D domain (T = 2 × L) and (d) 3D domain.

4.4.5 Quantification of the length of the exponential tail

Next, a quantitative description of the length of the exponential tail is explored. In the following, we will focus on the region $f > 1$ of $P(f)$, due to the importance of the large forces which can potentially lead to the fracture of particles and endanger a stable packing.

Figure 35a plots the exponent k as a function of particle sphericity. The exponent k is obtained by fitting the exponential tail ($f > 1$) of the different $P(f)$ (Figure 31) with Eq. (4.2). Error bars are omitted in Figure 35a for clarity (the 95% confidence bounds for k are typically within ± 0.025). Qualitatively the homogeneity of $P(f)$ decreases as the length of the tail increases (i.e. a lower value of k).

For particles of high sphericity ($\Psi = 0.995$), the values obtained for k are in the range $1.28 \geq k \geq 1.47$. These values are in between the values obtained by Mueth et al. [78] (packings of glass spheres in 3D with $k = 1.5$) and Gan et al. [79] (3D packing of spheres with $k = 1.24$).

Turning now to less spherical particles: In 2D packings, k decreases slightly with decreasing Ψ, i.e. $k = 1.42$ for $\Psi = 0.995$ and $k = 1.32$ for $\Psi = 0.47$. In 2D packing the decrease of k with decreasing Ψ can be fitted well by a linear function (dashed black line in Figure 35a). The comparatively high value of $k = 1.32$ for the lowest sphericity values studied ($\Psi = 0.47$) shows that there are relatively few cases of high contact forces in 2D packing of low sphericity particles. Good agreement is also seen when including data for k obtained by other works that have assessed compressed 2D packings (e.g. the data of Saint-Cyr et al. [152] is for trimer particles).

139

In pseudo-2D and 3D packings $k = 1.38\pm0.14$ for $\Psi > \Psi_{\text{crit}} = 0.7$. For $\Psi < \Psi_{\text{crit}}$ k decreases exponentially with decreasing Ψ and reaches a value of $k = 0.87\pm0.13$ for the lowest sphericity investigated, i.e. $\Psi = 0.42$. An exponential fit of k in pseudo-2D ($T = 2 \times L$) packings is shown by a solid line in Figure 35a. Hence, for $\Psi < \Psi_{\text{crit}}$ the probability of finding large contact forces ($f > 8$) increases exponentially and the contact force distributions become increasingly heterogeneous. The critical sphericity value, i.e. $\Psi_{\text{crit}} = 0.75$ for cross-shaped particles (2D) and $\Psi_{\text{crit}} = 0.7$ for star-shaped particles (3D) is the lowest sphericity for which a contact between two particles always involves the hemispherically-capped ends of the particles. This can be explained by the fact that, at this critical sphericity the arms protruding from a particle are exactly twice as long as the particle radius (Figure 35c). For $\Psi > \Psi_{\text{crit}}$, contacts will always involve the end-caps of a particle (Figure 35b), while for $\Psi < \Psi_{\text{crit}}$, contacts can also involve the flat/cylindrical section of the protruding arms (Figure 35c). Particles that only contact each other with the hemispherical end-caps, i.e. star-shaped particles with $\Psi \geq 0.7$, are more likely to slip relative to each other when a load is applied. Conversely, particles with contacts that involve the flat/cylindrical sections of the arms, i.e. star-shaped particles with $\Psi < 0.7$, are less likely to slip relative to each other which means that they are more likely to jam. When a particle jams during compression, the contact forces acting on such a particle can increase substantially (and without the particle unjamming the contact forces cannot relax). These high contact forces give rise to the long exponential tail of $P(f)$ for low sphericity particles, in particular for star-shaped particles with $\Psi < 0.7$. Whereas this rationale explains the transition at $\Psi_{\text{crit}} = 0.7$ for pseudo-2D and 3D packings, it is unclear why such a pronounced transition is absent for 2D packings. We speculate that the reason might lie in the particular spatial

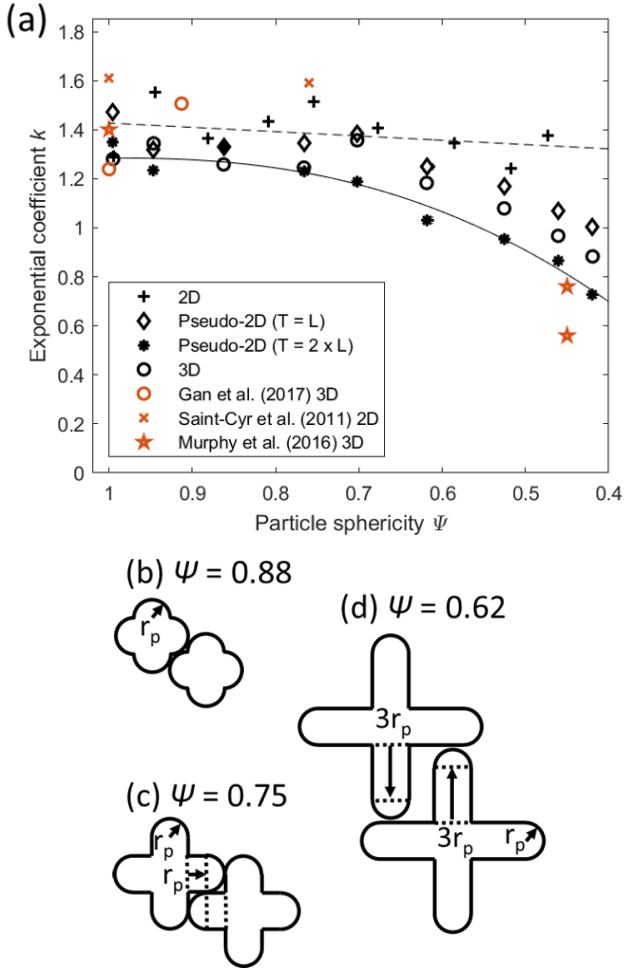distribution (morphology) of the particles which will be investigated in the following.

Figure 35: (a) Exponent k (Eq. (4.2)) obtained by fitting the exponential tail (f > 1) of the contact force distributions. Results of the present work are shown by black markers, while red markers

denote results from previously published studies. The dashed line is a linear fit (k(Ψ) = 0.18(1-Ψ)+1.43) to the values of k obtained in 2D packings (+), while the solid line is an exponential fit (k(Ψ) = -2.03(1-Ψ)$^{2.43}$+1.29) to the values of k obtained in pseudo-2D (T = 2 × L) packings (*). b)-d) Sketches of cross-shaped particles showing how the length of the protruding arms change with sphericity.

4.4.6 Packing morphology

By analyzing the probability distribution of the contact forces, $P(f)$, we found that in compressed pseudo-2D and 3D particle packings the length of the exponential tail of $P(f)$ increases with decreasing particle sphericity. In contrast, in 2D packings, the length of the exponential tail of $P(f)$ does not depend strongly on the particle sphericity. Hence, the question why the behavior of 3D packings differs distinctively from 2D packings remains unanswered. Instead of assessing the structure of a packing by an averaged, global parameter, such as the solid fraction, the morphology of the packings is assessed by calculating their radial distribution functions, RDF (G(r), Figure 36).

Comparing the RDFs in 2D packings as a function of sphericity (Figure 36a), one observes that for cross-shaped particles of low sphericity ($\Psi = 0.75$) the first ($r/L = 0.76$) and second ($r/L = 1.5$) peak, are more prominent compared to the first ($r/L = 1$) and second ($r/L = 1.91$) peak of more spherical particles ($\Psi = 0.995$). These peaks correspond to particle configurations of local crystallinity which are also the closest possible arrangements of interlocking particles. Sketches of such crystalline particle configurations are shown in Figure 36 (and enhanced in Figure 37). More pronounced peaks imply a more frequent occurrence of the respective particle configurations. The distances D_1, D_2, D_3 between the centers of two

interlocking particles, as defined in Figure 36, can be calculated by:

$$D_1 = \sqrt{d_p{}^2 + \left[(L + d_p)/2\right]^2}$$
$$D_2 = 2D_1, \qquad D_3 = 3D_1 \qquad\qquad (4.11)$$

For cross-shaped particles with $\Psi = 0.75$ the values of the first ($r/L = 0.76$) and second ($r/L = 1.5$) peak of the RDF are close to the geometrically determined values of the D_1 and D_2 configurations ($D_1/L = 0.75$ and $D_2/L = 1.49$). This indicates that the peaks in the RDF indeed correspond to the proposed closest crystalline configurations. In the RDF of 2D packings of particles with $\Psi = 0.75$ the peak positions are shifted to lower values of r/L compared to the RDF of 2D packings of more spherical particles ($\Psi = 0.995$). The position of the peaks (D_1/L) shifts to lower values for decreasing Ψ because L increases with decreasing Ψ and $\frac{D_1}{L} \propto \frac{(L+\sqrt{L})}{2L} < 1$. For 2D packings of cross-shaped particles with $\Psi = 0.75$ a small third peak can be seen at $r/L = 2.23$, which corresponds to a similar packing configuration as the one described above (four-particle configuration) with an analytical value of $D_3/L = 2.24$. These first three peaks can also be seen in the RDFs of 2D packings of particles with lower sphericity. The positions of the peaks as well as the analytically obtained positions are shown in Table 8. Since these three peaks are observed even in 2D packings of highly non-spherical particles one can conclude that structures of local crystallinity can be observed in all of these packings.

Ψ	1ST PEAK	D_1/L	2ND PEAK	D_2/L	3RD PEAK	D_3/L
0.473	0.55	0.55	1.12	1.11	1.66	1.66
0.518	0.58	0.57	1.14	1.14	1.73	1.71
0.585	0.62	0.61	1.25	1.21	1.82	1.82
0.754	0.76	0.75	1.50	1.49	2.23	2.24
0.995	1.00	0.98	1.91	1.95	none	2.93

Figure 36b plots the RDFs of star-shaped particles in 3D packings. The RDF of particles with $\Psi = 0.995$ shows a first peak at $r/L = 1$ and a second peak at $r/L = 1.9$. These peaks are at the same positions as in the RDF of 2D packings of cross-shaped particles with $\Psi = 0.995$ because both particle shapes are almost spherical and cannot interlock. In 3D packings of star-shaped particles with $\Psi = 0.702$ the first peak is located at $r/L = 0.7$ and the second peak at $r/L = 1.37$. Compared to 2D packings of cross-shaped particles with similar sphericity, the peaks are shifted to lower r/L values. This observation can be explained by the fact that star-shaped particles in 3D packings have additional degrees of freedom compared to cross-shaped particles in 2D packings allowing closer packing configurations in 3D packings. A sketch of the closest packing of star-shaped particles in 3D is shown in Figure 36b. The closest distance (J_1) between the centers of two star-shaped particles in the packing configuration shown in Figure 36b is:

$$J_1 = \sqrt{3}d_p \qquad (4.12)$$

Hence, in 3D packings of star-shaped particles with $\Psi = 0.702$, the first peak J_1 is expected at $r/L = 0.58$ and the second peak at $r/L = 1.15$. However, the first and second peak are found at $r/L = 0.7$ and $r/L = 1.37$, respectively. This result indicates that the most likely packing configuration of star-shaped particles in a compressed 3D packing is considerably looser than the closest possible crystalline packing configuration. Hence, 3D packings have a different morphology to 2D packings, as the peak location in the RDF of 2D packings of cross-shaped particles agrees very well with the closest possible crystalline packing configuration which, however, is not the case for 3D packings.

Additionally, when comparing the RDF of 2D and 3D packings, one finds that the height of the peaks in the RDF of 3D packings is lower than in 2D packings, a further sign of a reduced crystallinity when introducing an additional dimension. The reduced peak height is particularly noticeable when comparing the RDF of cross-shaped particles with $\Psi = 0.754$ (2D packing, Figure 36a) with the RDF of star-shaped particles with $\Psi = 0.702$ (3D packings, Figure 36b). Even a third peak is visible in the RDF of the 2D packing ($\Psi = 0.754$), whereas a third peak is absent in the RDF of a 3D packing ($\Psi = 0.754$). The reduction in crystallinity in 3D packings is more pronounced for particles of lower sphericity, i.e. $\Psi < 0.702$ ($\Psi < \Psi_{crit}$); in such packings even the first peak in the RDF disappears completely, indicating an amorphous packing structure. A reduced peak height in the RDF of packings of rod-like particles with decreasing particle sphericity has also been observed in previous works [51,134,170].

To summarize, the crystallinity of 3D packings of star-shaped particles decreases with decreasing particle sphericity. In 2D

packings of cross-shaped particles, however, such a decrease in crystallinity with decreasing sphericity could not be observed. The data in Figure 36 shows that interlocked, crystalline, configurations are found in 2D packings of cross-shaped particles with $\Psi < 0.7$, whereas such configurations do not seem to be present to a large extend in 3D packings of star-shaped particles with $\Psi < 0.7$. This can be explained by considering that 3D star-shaped particles have three additional degrees of freedom (one translational degree and two rotational), compared to 2D cross-shaped particles. It is therefore less likely that star-shaped particles, when dropped into a 3D

container followed by compression will configure themselves into a highly crystalline packing.
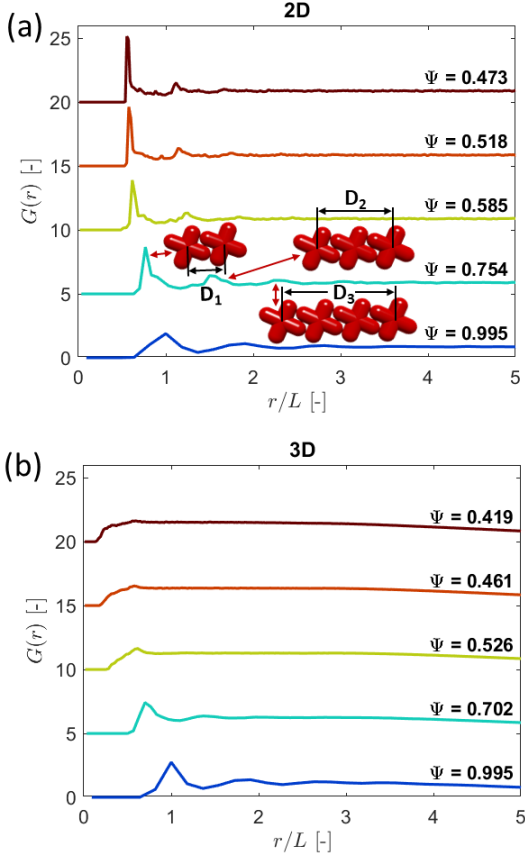
Figure 36: Radial distribution function (RDF), G(r), for (a) 2D and (b) 3D packings of particles of different sphericity. For better readability, the curves are shifted vertically with an offset of 5. In 2D packings, the distance between the particle centers corresponding to the first, second and third peak are labeled D_1, D_2 and D_3. The distances D_{1-3} can be determined analytically according to Eq. (4.11), and J_1 according to Eq. (4.12).
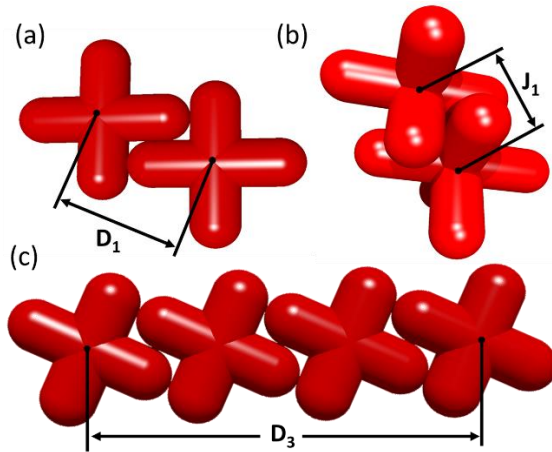
Figure 37: Visualization of particle configurations with the shortest possible distance (D_1, D_3, J_1) between particle centers (black dots): (a) cross-shaped particles used in 2D simulations, (b) star-shaped particles used in pseudo-2D and 3D simulations and (c) configuration of four cross-shaped particles. D_1 and D_3 can be calculated according to equation Eq. (4.11), and J_1 according to Eq. (4.12).

4.4.7   Linking force distributions to packing morphology

We described above that in 3D packings, below a critical value of $\Psi < \Psi_{\text{crit}} = 0.7$, the length of the exponential tail of the contact force distribution increases with decreasing particle sphericity. The increasing length of the exponential tail in 3D packings (and not in 2D packings) for sphericities $\Psi < 0.702$ seems to coincide with the disappearance of peaks in the RDF. To understand this observation, we revisit the work by Luding [154], who used the DEM to investigate particle stresses of

monodisperse and polydisperse packings of discs in a perfectly hexagonal 2D lattice. For perfectly monodisperse particles, a uniform particle stress distribution was observed. However, as soon as some polydispersity was introduced, by varying the disc diameter by a small amount ($\pm 0.33\%$), localized force chains were observed in the particle packing. Luding [154] also observed that the probability of large particle stresses to occur increases with increasing polydispersity, i.e. the length of the exponential tail of the particle stress distribution increases with increasing polydispersity. One can interpret the findings of the present work as complement to Luding's [154] results for non-spherical particles, i.e. a decreasing crystallinity of the packing (induced by either polydispersity or non-sphericity) leads to wider, less homogeneous, contact force and particle stress distributions, provided that the following two assumptions hold: (1) The introduction of polydispersity does lead to a reduction in crystallinity and (2) the behavior of the particle stress distribution, $P(i)$, depending on particle sphericity is very similar to that of the contact force distributions, $P(f)$.

Concerning the first assumption, there is indeed evidence of reduced peak heights in the RDF of a hexagonal packing with 5% polydispersity, when compared to the RDF of a monodisperse packing [171]. The reduced peak height hints towards a reduced crystallinity in polydisperse packings, however, further research is required to confirm the assumption.

To confirm the second assumption, that the exponential decay of the particle stress distribution is similar to the decay of the contact force distribution, one can compare $P(f)$ and $P(i)$, i.e. the probability distribution of the normalized first stress invariant $i = I_{1,i}/\langle I_1 \rangle$ shown in Figure 38. Generally, the shape

of $P(i)$ is similar to the shape of $P(f)$, i.e. for 2D packings distributions of type A and for 3D packings of low sphericity particles distributions of type B are obtained. For high sphericity ($\Psi > 0.7$) cross-shaped particles in 2D packings (Figure 38a), the distributions exhibit a pronounced peak at $i = 1$, which disappears for $\Psi < \Psi_{crit} = 0.7$ as $\lim_{i \to 0} P(i)$ increases with decreasing Ψ. Specifically, in 3D packings of star-shaped particles, $P(i)$ has a type A-like distribution for $\Psi \geq 0.7$ (peak at $i = 1$ and an exponential tail of similar length as in 2D packings), and no particle experiences a stress invariant with a magnitude of more than 6 times the mean. However, for 3D-packings of star-shaped particles with $\Psi < \Psi_{crit}$, the shape of $P(i)$ changes to a type B distribution and the length of the exponential tail of $P(i)$ increases with decreasing particle sphericity. The steep increase of $\lim_{i \to 0} P(i)$ implies that there is an increasing number of particles that experience only a very small fraction of the load that is put on the packing by uniaxial compression. At the same time, owing to the increasing length of the exponential tail, some particles experience stresses that are significantly higher than the mean. These trends match the behavior of $P(f)$, as described further above.

The transition of $P(i)$ to a type B distribution in 3D packings of star-shaped particles for decreasing sphericity, is attributed to an increasing frequency of contacts between the flat parts of the arms protruding from the particles (Figure 35c). Such contacts are only possible for star-shaped particles with $\Psi < \Psi_{crit}$, whereas for $\Psi \geq \Psi_{crit}$ all contacts between star-shaped particles involve the hemispherical end-caps of the spherocylinders. Particles forming contacts between the flat parts of the spherocylinders are less likely to rearrange during uniaxial compression. This effect can also be interpreted as an increased

apparent friction coefficient between particles. Such particles are more likely to jam during uniaxial compression, instead of rearranging into a configuration which would reduce the stress acting on the particle. As a consequence, high stresses can build up which results in an increased length of the tail of $P(i)$. The build-up of stresses in some particles leaves other particles to contribute little to the stress transmission in the packing leading in turn to an increase of $\lim_{i \to 0} P(i)$ with increasing apparent friction [172].

To summarize, the dependence of the length of the exponential tail of $P(i)$ on particle sphericity is very similar to the respective behavior of $P(f)$. Hence, our results can indeed be considered as complementary to Luding's [154] observation on the effect of polydispersity on the stress distribution in particle packings, i.e. a decreasing crystallinity (due to increasing non-sphericity or polydispersity) leads to a extended tail of the contact force and particle stress distributions.
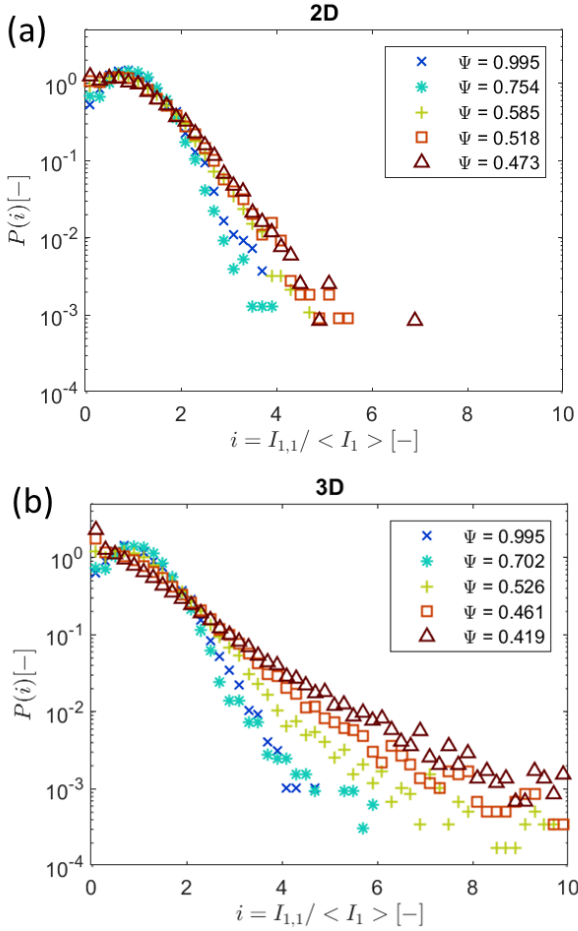
Figure 38: Probability distributions of the normalized first stress invariants P(i) as a function of particle sphericity in (a) 2D and (b) 3D packings. The normalized first stress invariants i are obtained by normalizing the first stress invariants $I_{1,i}$ by $<I_1>$.

4.5 Conclusions

This work investigated compressed 2D and 3D packings of non-spherical, non-convex, cross- and star-shaped particles using a newly developed DEM. Such non-convex particles can interlock forming packings that may sustain compressive and tensile forces despite containing purely non-cohesive particles. The particle sphericity (Ψ) was varied in the range $\Psi = 0.42$ - 1. The morphology of the packings was investigated by calculating the radial distribution function (RDF). Through the RDF we have established a link between the packing morphologies and the contact force probability distributions as expressed by the decay exponent k.

In 2D packings of cross-shaped particles a linear decrease of k was observed, from $k = 1.42$ for $\Psi = 0.995$ to $k = 1.32$ for $\Psi = 0.47$. For pseudo-2D and 3D packings of star-shaped particles k is independent of the sphericity ($k = 1.38\pm0.14$) for $\Psi \geq 0.7$; however, for smaller sphericities (i.e. $\Psi < 0.7$) the magnitude of k decreases exponentially with decreasing Ψ. These findings connect for the first time the results of previous works [62,79,152] on compressed packings of non-spherical particles. This allows us to establish the following general correlations between Ψ and the heterogeneity of the distribution of the contact forces expressed by the magnitude of k:

- In compressed 3D packings, the distribution of contact forces in the normal direction becomes increasingly heterogeneous, i.e. the length of the exponential tail increases exponentially with decreasing particle sphericity, independent of the specific particle shape.
- In 2D packings the influence of particle sphericity on the distribution of the contact force distribution in the normal direction is small. In contrast to the

153

exponentially decreasing k with decreasing Ψ in 3D packings, the decrease of k with decreasing Ψ in 2D packings is linear.

The heterogeneity of the contact force distribution needs to be considered when designing particles for specific applications such as aleatory construction for which non-convex particles with low sphericity (e.g. $\Psi = 0.45$ [62]) are desired. Such particles need to be able to withstand the highest contact forces, that can reach values that are an order of magnitude higher than the mean contact force.

We further establish a link between the increasing heterogeneity of the distribution of the contact forces and the packing morphology in packings of non-spherical particles. We have demonstrated that the increasing heterogeneity in the contact force distributions with decreasing sphericity correlates with a decreasing crystallinity of the packings. The link between a decreasing packing crystallinity and more heterogeneous contact force distributions has been postulated previously by Luding [154] for spherical particles, when assessing the effect of polydispersity on the homogeneity of the particle stress distributions. Hence, our results can be interpreted as complementary to this previous observation providing further evidence that a reduced packing crystallinity, through either an increase of domain dimensionality, particle non-sphericity or polydispersity, leads to a more heterogeneous stress distribution.

5 Manufacturing complex Al$_2$O$_3$ ceramic structures using consumer-grade fused deposition modelling printers

Adapted from:

5.1 Abstract

Purpose

The aim of this work was to fabricate complex ceramic tetrahedron structures, which are challenging to produce by more conventional methods such as injection molding. To achieve this aim, thermoplastic-ceramic composite filaments were developed and printed with unmodified, consumer-grade, fused deposition modelling (FDM) printers instead.

Design/methodology/approach

Al_2O_3 ceramic powder was mixed with ethylene vinyl acetate (EVA) polymer as a binder (50 vol.-%) to form a filament with a constant diameter of 1.75 mm. After the printing and thermal treatment stages, the shrinkage and mechanical properties of cuboid and tetrahedron structures were investigated.

Findings

The shrinkage of the parts was found to be anisotropic, depending on the orientation of the printing pattern, with an increase of 2.4% in the (vertical) printing direction compared to the (horizontal) printing layer direction. The alignment of the ceramic particle orientations introduced by FDM printing was identified as a potential cause of the anisotropy. This study further demonstrates that employing a powder bed during the thermal debinding process yields sintered structures that can withstand twice the compressive force.

Originality/value

Ceramic FDM had previously been used primarily for simple scaffold structures. In this study, the applicability of ceramic FDM was extended from simple scaffolds to more complex

geometries such as hollow tetrahedra. The structures produced in this study contain dense parts printed from multiple contiguous layers, as compared to the open structures usually found in scaffolds. The mechanical properties of the complex ceramic parts made by employing this FDM technique were also subjected to investigation.

5.2 Introduction

Fused deposition modelling (FDM) is a widely used, additive manufacturing technique for commercial as well as for consumer-grade applications, where it is colloquially known as 3D printing [173]. Other labels for FDM can be found in the literature such as fused deposition of ceramics (FDC), extrusion freeform fabrication (EFF) and fused filament fabrication (FFF) [174–176]. The technique uses a thermoplastic feedstock which is extruded through a heated nozzle that follows a pre-programmed path. Complex geometries can be built by depositing multiple layers of material that overlay each other [177]. After the extruded thermoplastic material leaves the nozzle, it fuses with the previously deposited material layer, before cooling and solidifying within seconds [178]. This technique has been adapted for the production of ceramic parts by mixing the thermoplastic binder material with a ceramic powder [179]. Depending on the properties of the ceramic powder and the thermoplastic binder material, a powder content of 45 to 60 vol.-% is necessary in order for the printed parts to retain their shape during the subsequent debinding and sintering process [180,181].

While the FDM method for ceramics offers advantages with regard to the storability and flexibility of the filament, certain

disadvantages have also been identified [175]. The difficulties in using FDM for ceramics arise from the necessity of removing the polymeric binder component from the printed part before sintering. Binder removal can lead to cracks and blisters in the final, sintered, ceramic parts, problems which are well known from other thermoplastic shaping processes for ceramics such as injection molding, thermoplastic extrusion and pressing [182,183]. Partial debinding with a solvent or super critical fluid can be used to avoid structural defects in the ceramic parts [184]. Alternatively, debinding in a powder bed can be used, where the capillary forces in action extract the liquid binder components and any decomposition products with a low viscosity from the part [185–188], a process also referred to as wicking.

Previous work using the ceramic FDM technique was done by Bach et al. who printed piezoelectric scaffold structures from lead zirconate titanate and barium titanate [189]. Further scaffold structures, some with functional materials, were manufactured by other researchers [190–192]. The effect of stearic acid on the stability of the 3D printed scaffold structures during thermal treatment was investigated by Gorjan et al. [193]. They used different grades of ethylene vinyl acetate (EVA), together with tricalcium phosphate (TCP) and stearic acid, in order to manufacture bio-ceramic scaffold structures. Another functional material was used by Rangarajan et al. who investigated the homogeneity of simple structures created by using the FDC method [194]. One of the observed results was anisotropic shrinkage, which occurred during the thermal treatment.

In this study we extend the applicability of ceramic FDM from simple scaffolds to more complex geometries such as hollow

tetrahedra (see Figure 41A), which are difficult to produce by other methods such as injection molding. Such structures are interesting for use as granular packing material with a high, connected porosity, for example in catalytic applications like refractories, fixed bed reactors in the chemical industry, or porous asphalt [195,196]. The structures manufactured in the course of this study contain dense parts printed from multiple contiguous layers, as compared to the open structures usually found in scaffolds. The industrial size of these applications demands keeping the processing stages as simple as possible. In the case of conventional polymer FDM it has already been previously shown that the printing direction can greatly influence the mechanical performance of the individual parts. For example, Ahn et al. found that specimens manufactured from ABS P400 polymer and compressed perpendicular to the printing layers had a 15% lower compressive strength when compared to specimens compressed parallel to the printing layers [197]. However, to the best of our knowledge, no investigation of the possible anisotropic mechanical properties of ceramic parts made by employing the FDM technique has been done up to date. In this work we study the anisotropic properties of ceramic FDM structures with complex geometries. The shrinkage of structures during thermal treatment is investigated in respect of the printing direction and their mechanical properties are investigated by means of compression tests.

5.3 Methods

An outline illustrating the development steps and investigations performed during this study is shown in Figure 39. The feedstock composition was developed and evaluated with

regard to its suitability for FDM. Cuboid samples were simultaneously manufactured using the FDM technique in order to perform a preliminary investigation of the influence of printing parameters such as the amount of infill on the properties of the samples during thermal treatment as well as the compression strength. The experience gained from these preliminary investigations was finally employed to manufacture complex tetrahedron structures, which were subsequently evaluated in respect of their performance during thermal treatment and mechanical testing.
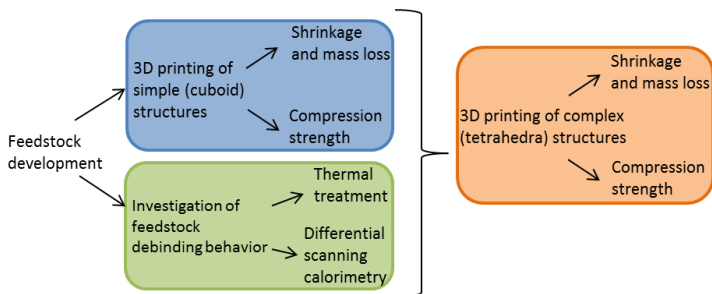
Figure 39: Schematic depicting the development steps and investigations performed during this study

The feedstock was developed on the basis of the experience obtained in previous studies [193]. An alumina powder loading of 50 vol.-% was chosen. A filament with a low powder content has a lower viscosity, which can cause buckling at the printing head during 3D printing. A high powder content increases the viscosity of the feedstock, thus increasing the risk of clogging the 3D printer nozzle. The alumina powder used was Al_2O_3 (CT 3000 LS SG, Almatis GmbH) with a mass median diameter (D50) of 0.5 µm. CT 3000 LS SG is an oxide material

widely used in ceramic research [198–205]. The binder consisted of ethylene vinyl acetate co-polymer (EVA) (Elvax 420™, DuPont International SARL) with a melting point of 73 °C and a melt flow rate of 150 g/10 min. In addition, stearic acid (Sigma Aldrich) was added as a surfactant. The exact formulation of the feedstock is shown in Table 9.

Table 9: Feedstock formulation used in this study.

Component	Volume [%]	Density [g/cm^3]	Mass [%]
EVA	40.9	0.93	15.6
Stearic acid	9.1	0.85	3.2
Alumina	50.0	3.97	81.3

The thermoplastic EVA-Al$_2$O$_3$ compound was mixed in a two-step procedure, using a high shear mixer (Rheomix 600, HAAKE Polylab OS, Thermo Electron Corporation Inc.) with roller rotors. In the first step, pre-mixing was performed at a temperature of 80 °C and a speed of 10 rpm for 20 minutes. After pre-mixing, the high shear mixer was emptied and cleaned to eliminate any unmixed zones from the chamber. In the second step, the material was mixed at 80 °C and a speed of 10 rpm for 20 minutes and then the speed was increased to 40 rpm for another 20 minutes. The feedstock was extruded with a piston extruder (RH7 Flowmaster, Malvern Instruments Ltd) using a circular die (diameter 1.75 mm) and at a temperature of 70 °C to create a filament for 3D printing with a consumer-grade FDM printer (K8200 3D printer, Velleman NV). The printing process was performed using a brass nozzle with a diameter of 0.6 mm and at a constant temperature of 170 °C. The extrusion multiplier, which defines the volumetric fraction of the feedstock being fed into the nozzle and extruded,

was set to 0.9. This value is <1 since the feedstock slightly expands after leaving the nozzle. The layer height, i.e. the distance from the nozzle to the previously deposited layer of material, was set to 0.5 mm. The printing speed, which defines the maximal velocity with which the nozzle traverses horizontally while material is being extruded, was set to 800 mm/min.

The geometric information was imported as stereolithography STL files into the Simplify3D software, which is used to slice the geometry into layers and determine the tooling path for each layer. A visualization of the tooling path for the square cuboid samples can be found in Figure 40A and Figure 40B. Figure 40 further shows two different cuboid orientations (upright Figure 40C and recumbent Figure 40D) used during printing. The printing direction (PD) denotes the direction in which the layers are stacked whereas the layer direction (LD) denotes the horizontal plane in which the printing tool moves during the creation of an individual layer. The printed cuboids have a length (l) of 15 mm and a width (w) of 3.54 mm independent of the printing orientation. Regardless of the geometry, the tool path first follows the contour of the object to be printed in order to create the surface. When a hollow sample is printed, the print head moves upwards and prints the next layer, which is in turn generated from the contour of the geometry (Figure 40A). When printing a sample with infill, the contour is printed first, as with the hollow sample. Before the next layer is deposited on top, the inside of the layer is filled with a predefined structure. This structure, for example a rectilinear grid of variable density, can be defined by the operator (Figure 40B).

After printing, the cuboid samples in this study were thermally treated according to the program shown in Figure 42, without

the use of a powder bed, in order to keep the thermal treatment as simple as possible.
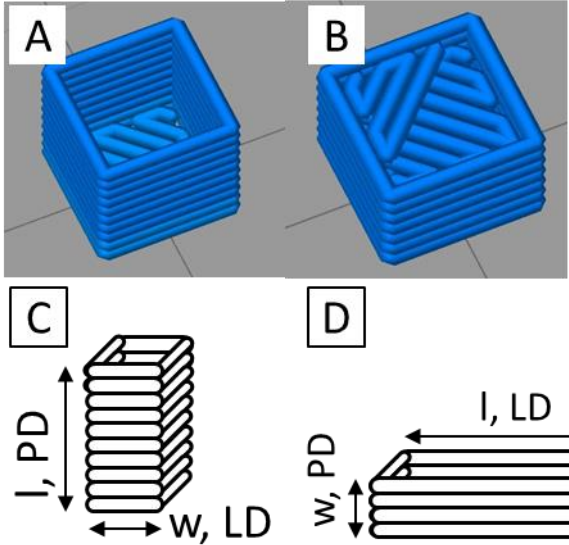

Figure 40: A/B) Visualization of tooling paths for the 3D printing of the cuboids, created using Simplify3D software. A) Hollow cuboid printed upright. B) Completely filled (100% infill) cuboid printed upright. C) Sketch of a cuboid sample printed in upright position. D) Sketch of a cuboid printed in recumbent position. PD denotes the vertical printing direction in which the layers are stacked, whereas LD denotes the horizontal layer direction in which individual layers are created. The length and width of the cuboid are denoted by l and w, respectively.

Using the knowledge gained in making these cuboids, the fabrication of more complex shapes, in this case tetrahedra, was undertaken next. The tetrahedron shape consisted of six

connected cylinders with a diameter of 3 mm and a length (c) of 20 mm with rounded ends, which were oriented along the edges of the tetrahedron, resulting in a height (h) of 16.33 mm. An image of this shape can be seen in Figure 41A. Due to the symmetry of a tetrahedron we can observe four different heights with equal length on a printed tetrahedron. One of these heights corresponds to the PD while the other three correspond to the other directions (OD). The tetrahedra were manufactured with three horizontal cylinders positioned flat on the printing platform while the remaining three cylinders were built upright on top of the lower three. After investigation of the printed cuboid structures, an infill comprised of a rectilinear grid with a porosity of 50% was selected for the manufacture of the tetrahedron. The tooling path for the three horizontal cylinders which form the base of the tetrahedron is shown in Figure 41B. The tooling path for the three upright cylinders is shown in Figure 41C (the blue hollow cylinders). Each of the tetrahedron's cylinders has a diameter of 3 mm, but the nozzle for printing the samples has a diameter of 0.6 mm. This leads to a thickness of contour of the shape of at least 0.6 mm. A single pass of the nozzle through the interior would already fill the remaining space by more than 50% (see Figure 41C). Therefore, the interior remains empty and the vertical cylinders of the tetrahedron remain hollow. This design problem does not occur in the horizontal cylinders forming the lower triangle of the tetrahedron shape. These layers have a shape resembling two concentric triangles, which leaves enough room to print a rectilinear grid with a 50% infill (Figure 41B). For debinding and sintering, the tetrahedra were placed in two different orientations: upright, which is the printing orientation (Figure 41D), and upended so that the PD was at an angle of 19.47° to the horizontal plane (Figure 41E). This was done to investigate

shrinkage independently of any deformation due to the tetrahedron's own weight.
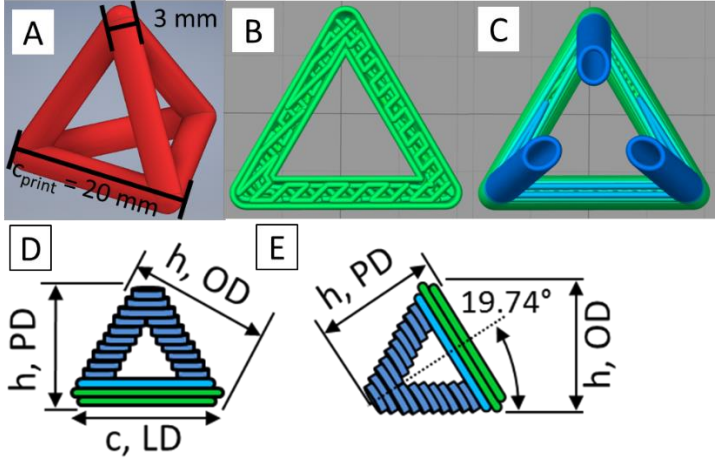

Figure 41: A) Image of the tetrahedron geometry to be printed. B) Horizontally printed cylinder parts of the tetrahedron, printed with a 50% infill of rectilinear grid structure. C) Vertically printed cylinder parts of the tetrahedron, printed without infill. The color indicates the printing speed (green is faster than blue). For debinding and sintering, the tetrahedra were placed in different positions in a furnace. D) Sketch of the layer orientation of a printed tetrahedron sample (the printing direction (PD) is vertical, this orientation is "upright" throughout the manuscript). The direction of the individual layers is denoted LD. E) Sketch of a tetrahedron sample upended so that the PD is at an angle of 19.47° to the horizontal plane. The height of a tetrahedron which does not correspond to the PD is labelled "other direction" (OD).

Thermal treatment of the printed samples was done in three stages. The first two stages, partial debinding and pre-sintering, were done in a PC12 furnace (Pyrotek GmbH) with a TC

405/30 controller (bentrup Industriesteuerungen). The third thermal treatment stage (sintering) was performed at 1600 °C in an air atmosphere for one hour using an LT 40/12 furnace (Nabertherm GmbH). After each stage, the samples were cooled down to room temperature by shutting off the oven in order to permit further analysis. Partial debinding was done at 230 °C for 8 hours unless otherwise stated, whilst full debinding and pre-sintering was done at 1000 °C for two hours. The pre-sintered samples were sufficiently robust to allow transfer to the high temperature oven for sintering. The complete temperature profile for all stages of the thermal treatment is shown in Figure 42. The cuboid samples were thermally treated in a recumbent position and placed on a solid surface. Upright printed cuboid samples were brought into a recumbent position for their thermal treatment. Overall, six different tetrahedra were investigated: three were thermally treated without a powder bed and three were partially debound and pre-sintered in a powder bed, thus facilitating the extraction of the binder using capillary forces [206]. Two of the tetrahedra were thermally treated in an upended position so that the printing direction was at a 19.47° angle to the horizontal plane (Figure 41E); one with and one without a powder bed. The powder bed consisted of Al_2O_3 (Nabalox NO 201, Nabaltec, Germany) with a mass median diameter (D50) of 80 μm.
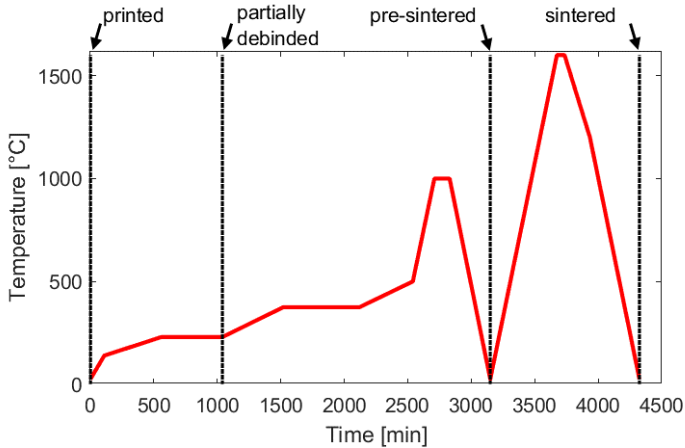
Figure 42: Temperature profile of the full thermal treatment for each of the 3D printed parts. The dotted vertical lines indicate the stages at which samples were inspected for further analysis.

For the thermogravimetric analysis (TGA) of the decomposition of the EVA binder in air, a STA 449 F3 Jupiter (Netzsch GmbH) thermal analyzer was used, together with pieces of the 1.75 mm thick filament. Thermo-mechanical analysis (TMA) of the cuboid samples was performed by using a TMA 402 F3 Hyperian (Netzsch GmbH) and heating them to 1550 °C in air. During the TMA measurements the samples were in an upright position and a static force of 0.1 N was applied in the vertical direction. Mechanical testing of the sintered parts was done using a universal testing machine (UPM 1478, ZwickRoell GmbH & Co. KG). The force was applied uniaxially in the vertical direction by means of placing rigid, flat plates placed on both sides. The surface of the sintered samples manufactured using FDM is uneven. Therefore, the steel plates on both ends were padded with cardboard and rubber to ensure that the applied force was

167

distributed evenly. During the experiments the samples were compressed uniaxially at a constant speed of 4 mm/min until the failure of a sample which led to a sudden drop in the compressive force. At that point compression was stopped. The tetrahedron samples were mechanically tested in the same position as that in which they had been thermally treated (upright or upended). Scanning electron microscope (SEM) images were acquired with a VEGA3 (Tescan a.s.).

5.4 Results and discussion

5.4.1 Development of printable filaments and thermal treatment

Once the samples are 3D printed, the thermoplastic binder must be removed (debinding stage). Figure 43 shows the TGA-DSC analysis of the filament samples. For the analysis, 2 mm-long pieces of the extruded filament with a diameter of 1.75 mm were used. Then two different heating programs were implemented, one with and one without the optimized debinding process stage. Figure 43A shows the heat treatment at a constant heating rate of 5 °C/min up to 600 °C. In Figure 43B the debinding program has been optimized for this study. The optimized program was used for all samples throughout this study. The binder starts to decompose at temperatures above 170 °C, as indicated by the mass loss seen in the TGA analysis of both samples. For the sample shown in Figure 43A, a sudden decrease of mass can be observed at a temperature of 322 °C and again at 433 °C. This sudden decrease of mass coincides with a strong exothermic peak in the DSC graph. The sudden loss of mass also leads to the formation of defects in the ceramic part [207]. When the optimized debinding program is used, the exothermic peak can be reduced significantly and a

more continuous loss of mass can be observed during the debinding stage, as shown in Figure 43B. The optimized debinding program is characterized by slower heating rates and additional dwell times for a gentler binder removal which mitigates the aforementioned formation of defects [187]. The final mass loss of the samples was 19.0% (Figure 43A) and 18.8% (Figure 43b). These values are close to the total content of the organic binder, (18.8%) based on the feedstock composition used (see Table 9).
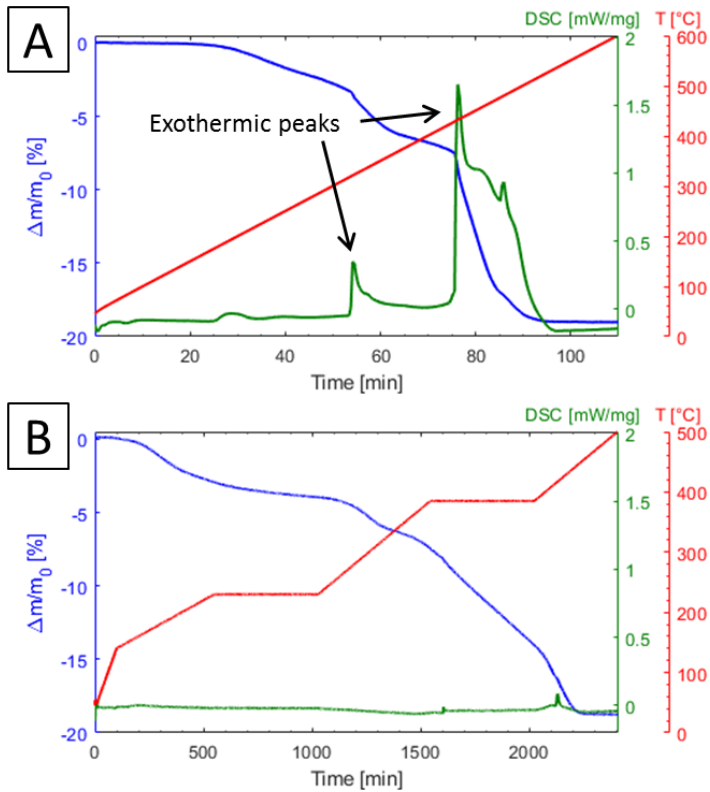
*Figure 43: Results of the thermogravimetric analysis of the debinding process stage used to remove thermoplastic binder and organic surfactant from a filament sample. The temperature profile is shown in red while the change in mass is shown in blue. The differential scanning calorimetry (DSC) is shown in green. A) Sample heated at a constant heating rate of 5 °C/min. B) Sample heated with an optimized debinding program.*

5.4.2　3D printed cuboid structures: thermal treatment and mechanical properties

Figure 44 shows images of the 3D printed and sintered cuboids for each of the four configurations (recumbent 100% infill, recumbent 0% infill, upright 100% infill and upright 0% infill). Four samples were used to investigate shrinkage and mass loss after the different thermal treatment stages (Figure 42). After sintering, the cuboids with 100% infill exhibited slightly convex surfaces. This can be attributed to gas transport from the center to the surface of the sample during the decomposition of the thermoplastic binder. If this gas transport is limited, pressure inside the sample will result in the expansion of the sample [207]. Such an expansion is shown in Figure 44A and Figure 44C, where the swelling is indicated with black arrows.
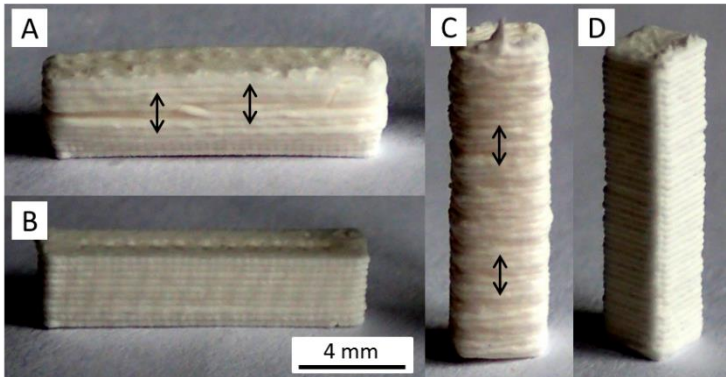
Figure 44: Images of 3D printed cuboids after sintering. A) Printed with 100% infill in recumbent position. The direction of expansion (swelling) observable in samples with 100% infill is denoted by black arrows. B) Printed hollow (0% infill) and in recumbent position. C) Printed upright with 100% infill. D) Printed with 0% infill in upright position. The scale bar is valid for all subfigures.

171

Figure 45A shows a cracked sample printed with 100% infill after sintering. The sample has irregular, internal void structures, which are a result of the decomposition of the thermoplastic binder. This observation corroborates the assumption that the decomposition of the binder leads to an increase in gas pressure, which forms bubbles inside the samples. Hrdina et al. proposed that the decomposition of EVA leads to the formation of acetic acid, which bloats the specimen [208]. This bloating in turn explains the swelling of the samples printed with 100% infill, as shown in Figure 44A and Figure 44C. Such an expansion could be avoided in samples with a 0% infill print parameter (Figure 45B).
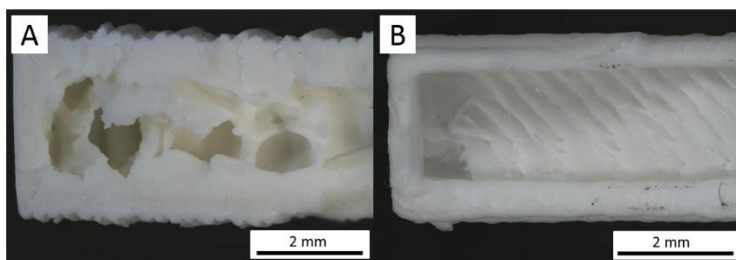
Figure 45: Microscopy images showing the inside of fragments of cuboid samples which cracked along their length. A) Sample printed with 100% infill. B) Sample printed with 0% infill.

Thermal mechanical analysis was used to investigate the shrinkage of the cuboids during the sintering process. Due to the softening of the polymeric binder (EVA and stearic acid), the shrinkage up to and including the pre-sintering stage cannot be analyzed using a dilatometer or TMA. Typically, a small load is applied between the sample and the TMA probe to ensure continuous contact. Therefore, deformation would

occur due to the softening of the thermoplastic EVA binder during TMA while debinding. It should be noted that the temperature range of the TMA used is limited to a maximum of 1550 °C and therefore full densification is not to be expected. The results of the TMA are shown in Figure 46. From this data (up to 1000° C) the coefficient of thermal expansion (CTE) for Al_2O_3 can be determined as being $8.7 \cdot 10^{-6}$ 1/K. The sintering of the CT3000 started at a temperature of 1086 °C and a heating rate of 3 °C/min. Vogt et al. performed dilatometry measurements using a heating rate of 5 °C/min and observed that the sintering of CT 3000 started at 981 °C [209]. The temperature at which the sintering process started shifted in the present study in comparison to the findings of Vogt et al. because a pre-sintering stage was employed. During sintering the sample measured in the LD direction has a slightly lower shrinkage value in comparison to the sample in the PD direction. This indicates that the printing direction has a significant effect on the total shrinkage of the sample and anisotropic shrinkage can be expected in structures printed by FDM. During the cooling process both samples shrank by an additional 1.34%, which corresponds to a CTE of $8.7 \cdot 10^{-6}$ 1/K. Munro previously reported a similar CTE of $8.1 \cdot 10^{-6}$ 1/K for polycrystalline Al_2O_3 at 1000 °C [210].
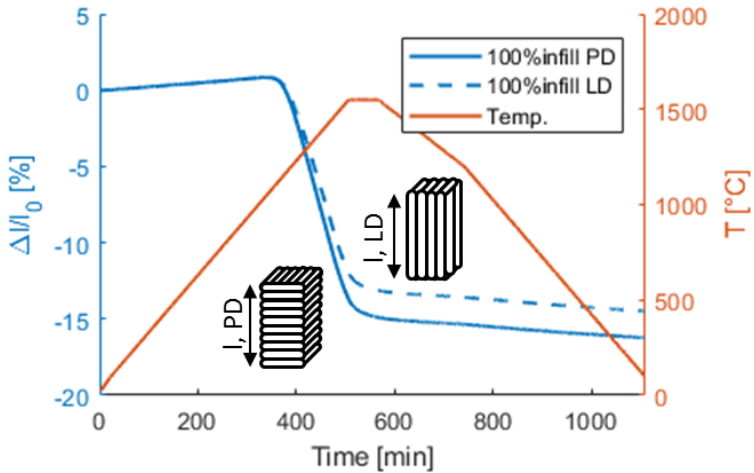
Figure 46: Thermomechanical analysis showing the shrinkage of cuboid samples printed with 100% infill in recumbent (measured along the LD) and upright position (measured in the PD).

In addition to the TGA and TMA analysis, mass loss and shrinkage of the cuboids were analyzed using an analytical scale and calipers after each thermal treatment stage. Figure 47A shows the shrinkage and the results of the mass loss analysis for the four configurations of cuboids (upright, measured in the PD, with 0% infill, recumbent, measured in the LD, with 0% infill, upright (PD) 100% infill and recumbent (LD) 100% infill). The data was averaged over all four samples of a respective configuration. In order to analyze the shrinkage, the length (*l*) of each cuboid was measured, which can correspond to either the PD or the LD, depending on whether the sample was printed upright or recumbent. The labels on the graphs indicate whether the PD or the LD was measured.

During the partial debinding stage, the samples with a 100% infill lost 3.4±0.2% (± one standard deviation) of their total mass (LD and PD) while the samples with 0% infill lost 4.5±0.2% and 4.9±0.3% of their total mass for the LD and PD orientation respectively. The reason for the higher mass loss of samples with 0% infill compared to samples with 100% infill is that the samples are less massive. In hollow samples the distance which the evaporating polymer needs to diffuse before escaping is shorter [185]. Furthermore, in the case of debinding in air, reactions with oxygen occur and the binder is transformed into a hard brown resin on the surface [211]. This leads to the formation of a dense skin on the surface, which hinders the transport of gaseous species and consequently leads to a pressure build-up which can cause cracking and bloating [193,198]. The formation of such a dense skin depends on the diffusion of oxygen into the samples.

In the TGA analysis (Figure 43B) a loss of 4.0% of the total mass has been observed after partial debinding (at the end of the 8h dwell time at 230 °C). Since the length and diameter of the TGA samples are smaller than the dimensions of the cuboid samples, the diffusion processes of the decomposition products have less significance and therefore a higher mass loss is to be expected. The influence of the diffusion process on the mass loss during partial debinding can be confirmed by cuboid samples with 0% and 100% infill. The mass loss of the TGA sample of 4.0% during partial debinding is closer to the mass loss of the cuboid samples with 0% infill (4.5±0.2% LD and 4.9±0.3% PD) than to that of the samples with 100% infill (3.4±0.2%). Similar results have been reported by Trunec et al. who reported that the binder mass loss at 230 °C increases with increasing surface to volume ratio [185].

175

After the pre-sintering stage at 1000 °C, all organics had decomposed, resulting in an overall mass loss of 19.0±0.9% averaged over all four sample configurations. This value corresponds to the average overall mass loss of the two TGA samples (19.0% and 18.8%) and the theoretical content of the organic material in the feedstock at 18.8% (see Table 9 and Figure 43). No further mass loss should occur during the sintering stage, which is confirmed by the constant average mass of the samples between the pre-sintering and sintering stage shown in Figure 47A.

The shrinkage data of the samples (Figure 47) shows that the most significant changes occur during sintering. During partial debinding and pre-sintering the samples shrank between 1.2±0.6% (0% infill PD) and 1.6±0.5% (100% infill LD). The shrinkages reported here are generally higher than the net shrinkage of 0.5% observed by Hrdina et al. during binder removal [212]. In their study, an EVA based binder blended with 51 vol.-% of ceramic powder was used and shrinkage was studied at 500 °C. Due to the fragility of the samples, the cuboids had to be heat-treated at 1000 °C, which resulted in higher shrinkage values compared to Hrdina et al. due to the effects of pre-sintering.

One exception is the 100% infill PD sample which was printed in an upright position, where an increase in length by 0.1±0.6% and 1.0±1.1% could be observed after the partial debinding and pre-sintering processes respectively. A possible explanation for this expansion in the PD is that the gas arising from the decomposing binder pushes the elongated ceramic particles apart while escaping the sample. Such particles can be seen in in Figure 48A. This SEM image shows that the CT 3000 LS SG powder used in this study contains a mixture of submicron

particles and 2 μm large platelet particles. During extrusion in the 3D printer, these elongated platelet particles become aligned due to shear in the nozzle [213–215]. Consequently, the elongated particles are aligned in LD, which is also illustrated in Figure 48B. Figure 48B further shows a gap d between the particles, which is filled with binder. When evaporating binder escapes the sample, these gaps expand. Assuming the gaps expand by equal amounts, one can envision from Figure 48B that the relative expansion in the LD is larger than in the PD. After binder decomposition the particles become locked into their positions. This prevents a full reversal of the expansion. The measured expansions are in well in line with the observed expansion of 100% infill samples after sintering (Figure 44A/C). Interestingly, such an expansion could not be observed for the 100% infill samples in the LD. This corroborates the theory proposed in Figure 48B.

The shrinkage of the cuboids during sintering was normalized by the length after the pre-sintering stage and is shown separately in Figure 47B. Samples with 100% infill printed in a recumbent position (measured in the LD) shrank by 14.6±0.2% and the samples printed upright (measured in the PD) shrank by 14.7±0.8%. At 16.1±0.6% for the samples measured in the LD and at 18.5±0.8% for those in the PD, the normalized shrinkage of the hollow samples is considerably higher. From this observation it can be deduced that the normalized shrinkage is generally higher for samples with 0% infill as compared to 100% infill samples. As already discussed for the TMA analysis (Figure 46), the shrinkage is anisotropic. For the 0% infill cases studied, the PD direction shrinks by an additional 2.4% compared to the LD direction. This cannot be observed in the 100% infill samples since these samples are

affected by the internal voids formed during the binder decomposition.

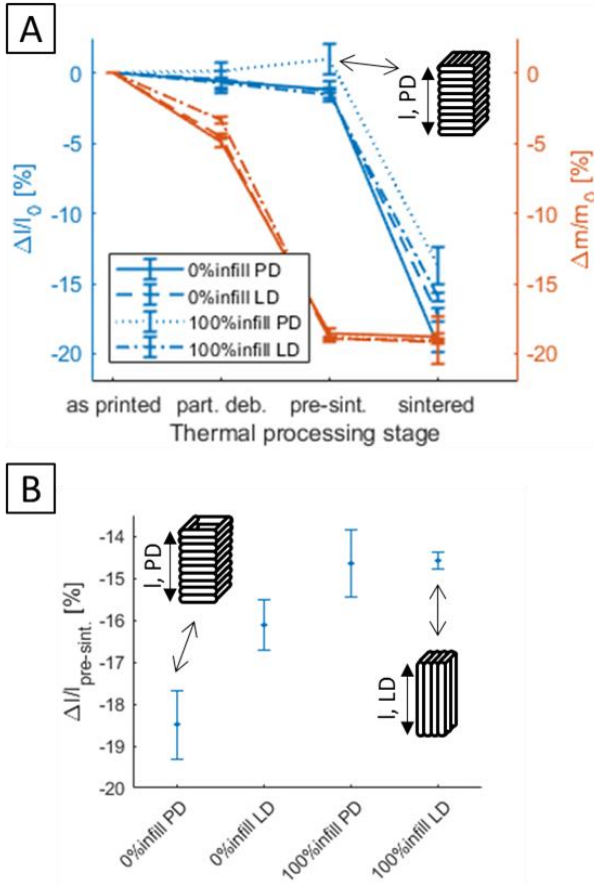*Figure 47: A) In blue: Average shrinkage of the cuboid samples during the different thermal treatment stages for the four different printing configurations (upright 0% infill (PD), recumbent 0% infill (LD), upright 100% infill (PD) and recumbent 100% infill (LD)) measured along the length of the samples. In orange: The average change of the samples during the different thermal treatment stages.*

B) The amount of shrinkage occurring during the final sintering stage relative to the pre-sintering length.
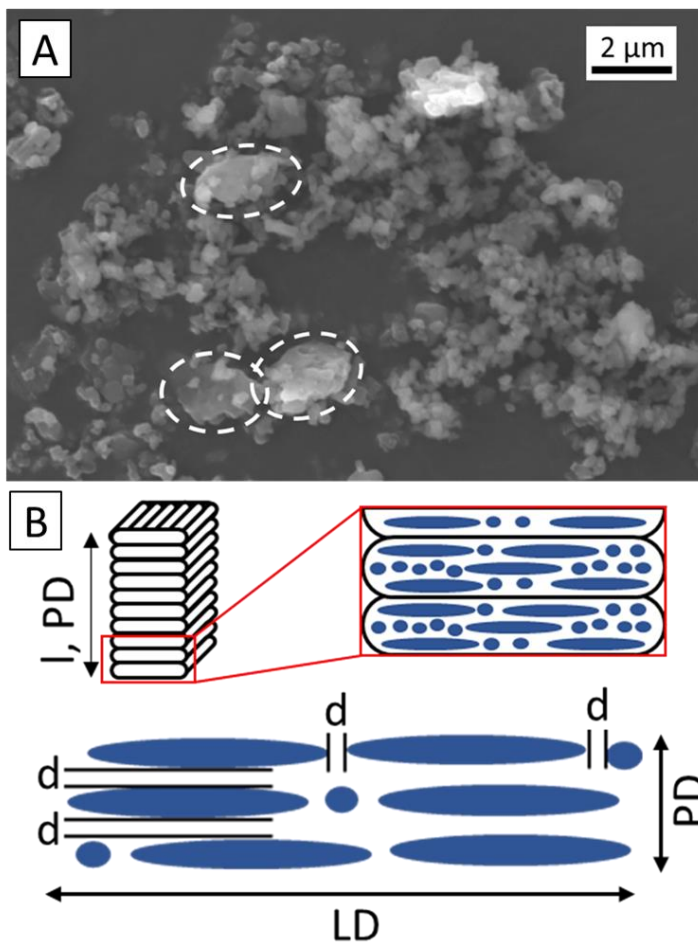

Figure 48: A) SEM image of CT 3000 LS SG powder used in this study showing some large platelet particles (dashed white circles). B)

Schematic explaining how the platelet particles contribute to the anisotropic expansion of samples during debinding.

As mentioned above, anisotropic expansion during debinding as well as anisotropic shrinkage during sintering was observed. According to the morphology of the CT 3000 LS SG alumina, which consist of slightly elongated submicron and platelet-like micro particles, the ceramic particles become aligned during the extrusion of the filament and the 3D printing. The orientation of the particles causes the expansion and shrinkage to be anisotropic.

The maximal compressive load of the different cuboid structures was evaluated by compression tests. The results of the three samples tested for each configuration are shown in Figure 49, together with the averages. One can see that the samples compressed along the LD show slightly higher values when compared with samples with the same infill percentage tested in the PD. A similar observation was made by Ahn et al. for 3D printed acrylonitrile butadiene styrene (ABS) polymer samples [197]. Figure 45 shows that, due to the formation of voids from the decomposing binder, the load-bearing cross-section is not considerably higher for the sample printed with 100% infill after sintering. Therefore, the average load at failure is only slightly lower for samples with 0% infill compared to samples with 100% infill with the same configuration.
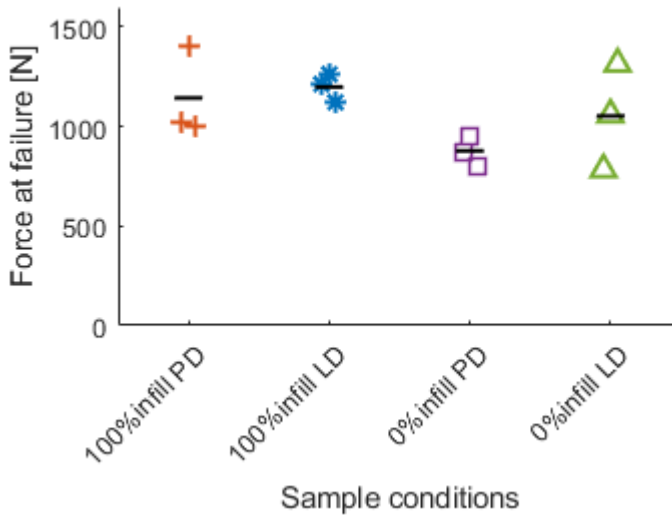
Figure 49: Compression force for the four different configurations of cuboid structures. The black bars depict the average value of the three samples analyzed.

5.4.3 3D printed tetrahedron structures: thermal treatment and mechanical properties

The knowledge gained from manufacturing the simple geometry of the cuboid samples was used directly in the production of the tetrahedron structures created using the FDM/FFF 3D printing method. Figure 50 shows tetrahedron structures and their transformation during the fabrication process after printing (Figure 50A), partial debinding (Figure 50B), pre-sintering (Figure 50C) and finally after sintering (Figure 50D). It was observed that the shape and surface quality do not change significantly until the pre-sintered stage (Figure 50C). The sintered samples decrease in size and the surface is

considerably smoother, with less roughness (Figure 50D). The brown discoloration during the partial debinding stage (Figure 50B) is due to the oxidation and decomposition of the thermoplastic binder [185,198,211]. This discoloration is related to the previously mentioned hard skin. It is suggested in the literature that this brown skin consists of products arising from the oxidation and thermal decomposition of the organic binder.
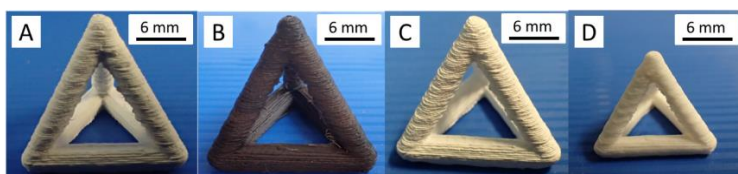
Figure 50: Tetrahedron-shaped part at different stages of the thermal treatment. A) As printed, B) after partial debinding, C) pre-sintered and D) fully sintered.

In order to assure shape stability, an infill of 50% had to be used in the printing of the tetrahedron samples. Some samples were placed in a powder bed to avoid expansion of the 50% infill parts in the tetrahedron due to gas pressure during the partial debinding stage. With the aid of capillary forces, the decomposed binder could be actively removed from the sample surface. Gorjan et al. have shown that, due to capillary forces, parts of a thermoplastic binder can be efficiently removed by use of a wicking process at 230 °C [186]. Figure 51 shows the shrinkage data (blue graph) of all horizontally oriented cylinders after the individual thermal treatment stages. During partial debinding some samples were treated with and some without a powder bed. In addition, upended samples (see Figure 41C) were partially debound under both conditions.

Furthermore, the mass loss for all experiments is shown in by the orange graph in Figure 51.

In addition, Figure 51 shows that samples treated in a powder bed initially lost a larger fraction of their total mass during the partial debinding stage compared to the samples treated without a powder bed (5.3±0.1% versus 4.0±0.02%). These values show that capillary forces indeed enhanced binder removal. The total mass loss of 4.0±0.02% in tetrahedra debound without a powder bed lies between the mass loss of cuboid structures with 100% infill (3.4±0.2%) and cuboid structures with 0% infill (4.5±0.2% LD and 4.9±0.3% PD). This result is consistent with tetrahedra having an infill percentage of 50% in the horizontal cylinders and 0% in the vertical cylinders. At the fully sintered stage, the samples treated in a powder bed and the samples treated without a powder bed had a total mass loss of 18.8±0.02% and 19.2±0.1% respectively, which is in the range of values obtained for cuboids and the theoretical mass loss of the feedstock composition.

The shrinkage of tetrahedra during debinding with and without a powder bed was investigated by measuring the length of each of the horizontal cylinders (corresponding to the LD) in the four samples with a caliper. The data shown as the blue line in Figure 51 suggests a slightly increased shrinkage for samples debound in a powder bed compared to samples debound without a powder bed. During debinding without a powder bed, the cylinders of the tetrahedra shrank by 1.8±0.7%. This value is comparable to the shrinkage of the cuboid structures in the LD (0% infill 1.2±0.6%; 100% infill 1.6±0.5%) which were likewise debound without a powder bed. The cylinders of tetrahedra debound in a powder bed shrank by 2.2±0.6%. After sintering, the final shrinkage in samples debound in a powder

183

bed was 17.8±1.6% as opposed to 18.3±2.0% in samples debound without a powder bed. These results are well in line with the shrinkage of cuboids with 0% infill when measured in the LD direction (17.2±0.5%).

Figure 52 compares the heights of the different tetrahedron configurations during the thermal treatment stages. In accordance with Figure 41, the heights of the tetrahedra were analyzed in the printing direction (PD) and in other directions (OD). Samples were partially debound with and without a powder bed. As already mentioned, the total shrinkage of tetrahedra partially debound in an upright position is not affected by the use of a powder bed. During partial debinding, upright and upended samples shrank by 2.5±1.3% and 2.4±0.3% respectively in the PD. For the OD, shrinkage of 1.6±0.5% (upright) and 1.8±0.5% (upended) was analyzed. The total shrinkage of the PD in upright and upended orientation is 20.9±0.4% and 17.2±0.4%, respectively. Since the PD and OD shrinkage values are equal regardless of the orientation of the tetrahedra during thermal treatment, deformation of the tetrahedra due to their own weight can be disregarded. Furthermore, the total shrinkage in the OD is in good agreement with the total shrinkage of the cuboids with 0% infill measured in LD (17.2±0.5%). As expected of the cuboids with 0% filling (total shrinkage of 19.5±0.5%), a larger shrinkage is to be observed in the PD. The anisotropy shown in these results can be explained with the non-random orientation of ceramic particles.

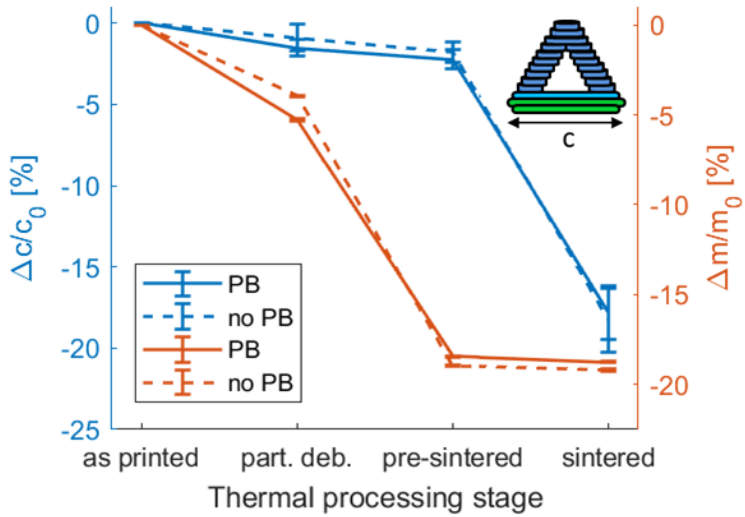*Figure 51: Shrinkage and mass loss of tetrahedra after different thermal treatment stages. Blue graph: Length c of the printed tetrahedra samples during thermal treatment with powder bed (PB) and without powder bed (no PB). The powder bed was employed only during partial debinding and pre-sintering. Orange graph: mass loss of the tetrahedra during thermal treatment stages.*

185
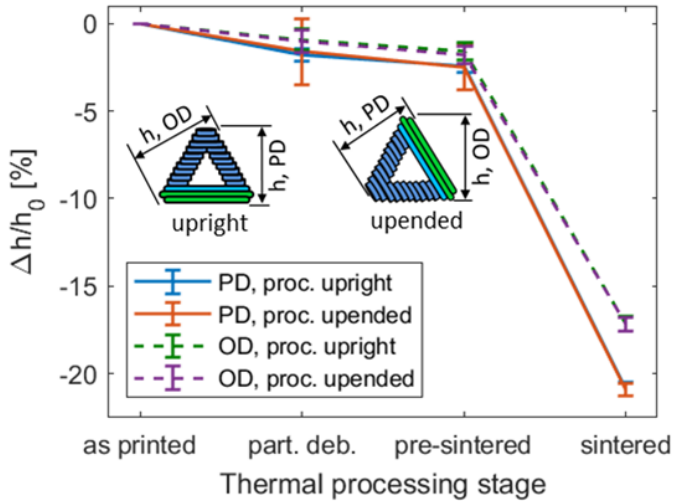
Figure 52: Shrinkage of tetrahedra that have been thermal treated in different positions. Heights (h) of tetrahedra, which correspond either to the print direction (PD) or the other directions (OD). The tetrahedra were either thermally treated in the upright direction in which they were printed (see Figure 41D) or upended so the PD was no longer vertical (see Figure 41E).

Figure 53 shows the force-displacement curves of the compression tests for the tetrahedra in different configurations and with different treatments. The samples were compressed from the top in the same orientation (upright/upended) that was used during the thermal treatment of each sample (see Figure 41C/D). The tetrahedra which were partially debound in a powder bed had a force at failure that was two times higher in comparison to those partially debound without a powder bed. This suggests that debinding without a powder bed introduced defects that negatively affected the mechanical strength of the

structures. Additional investigations on filament samples which were debound using the same thermal treatment as with the tetrahedra confirmed this. Several major as well as minor cracks could be observed inside filament samples debound without a powder bed. In filament samples debound with the use of a powder bed we observed that the magnitude and number of such cracks was greatly reduced. Images of the cross-sections of such filament samples can be found in the Figure 54 and Figure 55. Unexpectedly, the orientation of the samples (e.g. upright or upended) did not affect the force at failure.
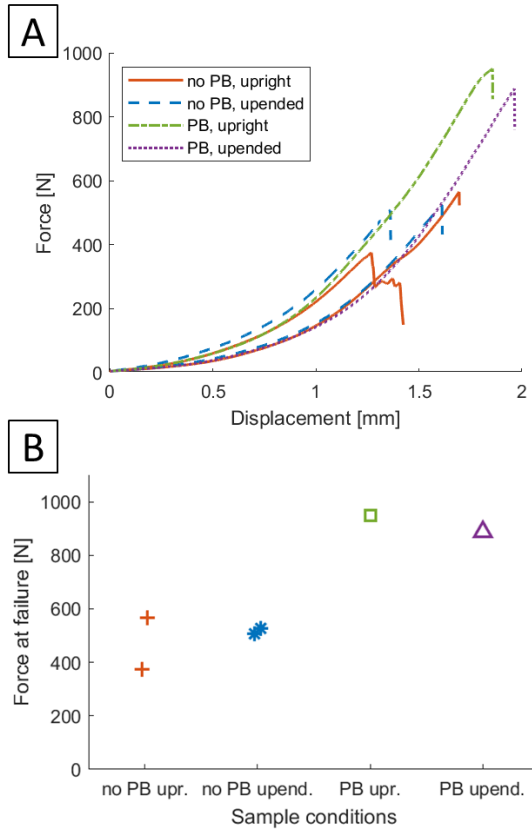
Figure 53: A) Force-displacement curve of tetrahedra during uniaxial compression tests. The samples were compressed vertically in the same orientation with regard to the layer structure as previously employed (see Figure 41D/E and Figure 52). B) The maximal force at failure of the tetrahedra samples.
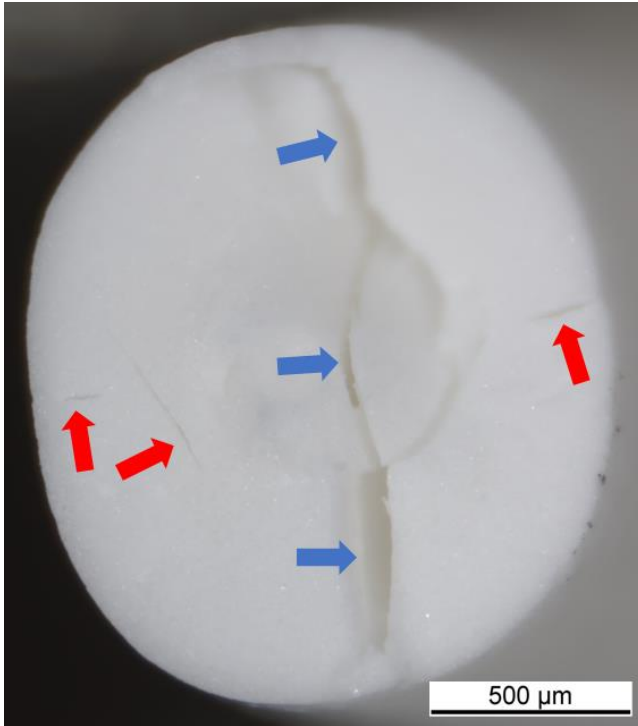
Figure 54: Image of the cross-section of a filament debound without a powder bed using the same thermal treatment as the other samples throughout this study. The blue arrows indicate a major crack through the whole diameter of the filament sample. The red arrows indicate minor cracks.

189
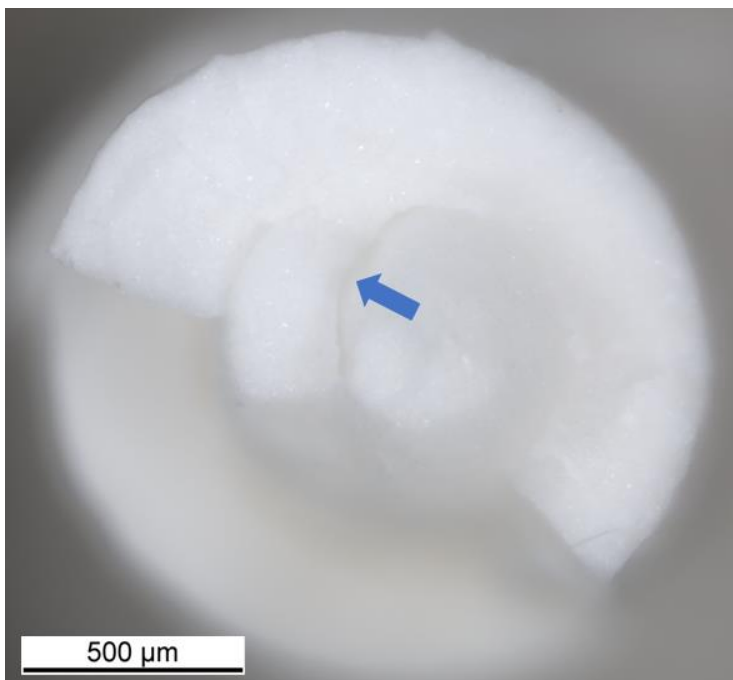
Figure 55: Image of the cross-section of a filament debound through the use of a powder bed while employing the same thermal treatment as with the other samples throughout this study. The blue arrow indicates a crack in the sample.

5.5 Conclusions

The thermoplastic alumina feedstock prepared as part of this study was successfully used to produce tetrahedron structures by means of a consumer grade FDM printer. This extends the applicability of ceramic FDM from simple scaffold structures to complex structures with multiple contiguous layers. An optimized thermal debinding program for an EVA-based binder system was developed. Slower heating rates and dwell

times were introduced to the debinding program to reduce exothermic events which could lead to defects in the parts. It was found that the shrinkage of parts during thermal treatment is anisotropic. Cuboids with 0% infill show increased shrinkage of 2.4% in the (vertical) printing direction compared to the (horizontal) layer direction. This result could be confirmed by analyzing the shrinkage of tetrahedra, where the printing direction shrank 3.7% more in comparison to the layer direction. From these results, we can deduce that ceramic structures manufactured using an FDM method show anisotropic shrinkage, which needs to be taken into account during the design of such structures. According to the morphology of the CT 3000 LS SG ceramic powder, the ceramic particles can be expected to obtain a preferential alignment during extrusion. Such an alignment of particles during the manufacturing of ceramic structures will result in anisotropic shrinkage. Further investigations with other ceramic powders will have to be done to confirm the relevance of process-related anisotropic shrinkage for other ceramic materials. Compression tests show that cuboid samples with 100% infill fail at roughly the same force as cuboids with 0% infill. This can be attributed to a reduction of the load-bearing cross-section of structures with 100% infill due to the formation of internal voids during debinding. The influence of the printing orientation on the mechanical properties was found to be minor. However, tetrahedra partially debound in a powder bed could withstand twice the compressive force compared to tetrahedra which were partially debound without a powder bed.

6 Conclusions and outlook

6.1 Conclusions

This dissertation has explored the benefits and challenges associated with the use of artificial aggregates of non-convex shapes for asphalt pavements. The work covered three areas: 1) An investigation of the beneficial properties of packings of non-convex aggregates, 2) a study of the influence of the aggregate shape on the stress distributions in their packings and 3) the manufacturing of complex aggregate shapes.

The investigation of the packings of non-convex aggregates shows that the packing density decreases with decreasing aggregate sphericity, confirming the findings of previous studies. Hence, using non-convex particles allows for packings with very low packing densities ($\varphi < 0.25$), which is much lower than the packing densities found for packings of common crushed rock aggregates ($0.75 < \varphi < 0.85$). A further finding is that the tortuosity of the pore space decreases linearly with decreasing packing density. A high porosity combined with a low tortuosity yields a high water permeability of packings of non-convex artificial aggregates of low sphericity. It was also found that the permeability increases exponentially with decreasing packing density and that the permeability of artificial aggregate packings can be two orders of magnitude higher compared to the permeability of crushed rock packings typically used for pavements. Moreover, the results of the permeability of the packings agree well with the prediction based on the Carman-Kozeny equation. Consequently, the elaborate measurement of the permeability for such artificial aggregate packings can be avoided in the future and instead the permeability can be predicted based on the packing porosity and the aggregate shape.

The beneficial properties of packings of artificial aggregates of low sphericity however do not come without drawbacks. The probability distributions of the inter-aggregate contact forces and the intra-aggregate stresses become more heterogeneous with decreasing aggregate sphericity. This increasing heterogeneity of the contact force distributions and stress distributions with decreasing aggregate sphericity was linked to a decrease in the packing crystallinity as the aggregates become less spherical. For low sphericity aggregates, long exponential tails are observed in both types of probability distributions, indicative of few aggregates that must withstand stresses exceeding ten times the average stress. A failure of such an aggregate due to breakage could lead to a rearrangement of the packing and therefore failure of the entire packing structure. Consequently, when designing the aggregate shape for a packing under load, some constraints on the aggregate sphericity might be required considering the material used for the manufacturing of the aggregates and the maximal load that can be supported by the packing.

As a material that offers high compressive strength, alumina (Al_2O_3) ceramic was investigated for the manufacturing of artificial aggregates. The alumina was compounded with an EVA polymer binder and formed into a filament that can be used in consumer-grade 3D printers to manufacture complex aggregate shapes. After 3D printing, heat treatment was used to evaporate the binder and sinter the alumina, yielding durable ceramic parts. This is an advancement compared to previous works, where similar ceramic-polymer filaments and heat treatment programs were employed, but only simple scaffolding structures were manufactured. It was further found that the parts shrink anisotropically during the heat treatment. Depending on the aggregate shape, the shrinkage is 2.4 to 3.7

percentage points higher in the direction in which the parts are layered, i.e. the direction that was vertical during 3D printing. It was proposed that the anisotropy of the shrinkage originates from a preferential orientation of the elongated alumina grains. This preferential orientation was introduced to the ceramic-polymer compound due to shear when the compound was formed into the filament and subsequently extruded through the 3D printer nozzle. Mechanical testing of the ceramic aggregates revealed that the anisotropy has no effect on the compression strength of sintered aggregates, which is identical for different orientations of the parts. The compression strength of the sintered aggregates however was found to increase when the 3D printed aggregate was submerged in a powder bed during binder evaporation. The reason for this is that the powder bed helps to draw out the binder from the 3D printed aggregate by wicking, which prevents the formation of defects such as cracks and blisters.

6.2 Outlook

The research presented in this dissertation lays the groundwork for the development of non-convex artificial aggregates for use in pavements. However, further work remains to be done in each of the three explored areas.

In chapter 3 it was shown that artificial aggregates of low sphericity form highly porous packings, which in turn is useful for applications such as permeable packings or energy harvesting from pavements. Consequently, such applications should be investigated further, for example by developing a pavement that incorporates highly porous channels formed by explicitly designed artificial aggregates. During hot days, water could be pumped through these porous channels with low

pressure loss to capture the heat energy while also cooling the pavement. This captured heat energy could also be used beneficially. Varying the aggregate shape can not only be used to maximize the porosity, but also to adjust the porosity to a specific value and to adjust the geometry of the pore space, such as the size of the necks between larger pores. By adjusting the pore space geometry an aggregate packing can for example be optimized for noise absorption, which is another desired property of asphalt pavements and should therefore be explored further. Yet another exciting property of non-convex aggregates is their interlocking. This has already been investigated for the construction of freestanding columns [62,113,114], however, in all of these studies the interlocking aggregate shapes were found by trial and error approaches. A systematic optimization of the aggregate shape for interlocking is missing thus far. Such an optimization study is rather complicated because there are infinite options to change the aggregate shape. One way to systematically explore the infinite optimization landscape of aggregate shapes would be to use a metaheuristic optimization technique, such as evolutionary computing or particle swarm optimization. In the end one could even imagine road pavements made from artificial aggregates that do not require any bituminous binder. Furthermore, the permeability and noise reduction properties can be useful for other construction materials such as facades of buildings.

Further work also remains to be done to investigate the stress distribution in aggregate packings. Previous studies on the contact force and stress distribution in aggregate packings have either reported probability distributions, or the force chain network topology. Curiously, a correlation between the topology of the force network and the probability distribution of the contact forces has not been proposed thus far. One reason

195

for the absence of such a correlation was the unclear origin of the different shapes observed for the probability distribution of the contact forces. This origin was unraveled in the present dissertation by establishing a link between the shape of these distributions and the packing morphology, which in turn is influenced by the aggregate shape. Consequently, in a future work the shape of the probability distribution of the contact forces can be varied via the aggregate shape, which should be used to explore the correlation between the topology of the force chain network and the probability distribution of the contact forces. Such a correlation would allow to build a bridge between the two viewpoints of an aggregate packing, i.e. the spatial viewpoint (network topology) and the probabilistic viewpoint, which are disconnected thus far.

This dissertation has shown that artificial ceramic aggregates of complex shapes can be manufactured via 3D printing. However, some disadvantages persist with this method, such as the large power consumption of the sintering process, which should be addressed with regards to its sustainability. The sustainability of artificial aggregates is also negatively affected by the use of virgin materials for both the ceramic and polymer. With further research these virgin materials could be replaced by recycled waste materials. To this end the alumina powder could, for example, be replaced by concrete waste from building demolition or ash from municipal waste incinerators, while the EVA polymer could potentially be replaced by other thermoplastics, for example from plastic bottles. The biggest hurdle for the advancement of the technology readiness level (TRL) and the adoption of complex shaped artificial aggregates for road pavements is certainly the scale-up of the manufacturing process. Currently it takes around 20 minutes to manufacture one aggregate with a size of approximately 20 mm

using a 3D printer. The possibly simplest approach that comes to mind might be to mount a 3D printer with several nozzle heads that all move in the same path to manufacture the same part multiple times simultaneously. This would leave the complexity of the three-axis mechanism of the 3D printer unchanged and would only require a scale-up of its size. This approach might scale-up the manufacturing speed of artificial aggregates by an order of magnitude. However, even faster might be the use of a ceramic-polymer feedstock for injection molding, where the time to manufacture a part is in the order of seconds [216], instead of minutes for 3D printing.

Bibliography

[1]   M.C. Betrò, Hieroglyphics: the writings of ancient Egypt, 1. ed., Abbeville Press Publishers, New York, London, Paris, 1996.

[2]   United Nations Environment Programme, Sand, rarer than one thinks, (2014).

[3]   Bundesamt für Statistik, Die Bodennutzung in der Schweiz, 2013.

[4]   Y. Yildirim, Polymer modified asphalt binders, Constr. Build. Mater. 21 (2007) 66–72.

[5]   J. Habbouche, E.Y. Hajj, P.E. Sebaaly, M. Piratheepan, A critical review of high polymer-modified asphalt binders and mixtures, Int. J. Pavement Eng. 21 (2020) 686–702.

[6]   S.M. Abtahi, M. Sheikhzadeh, S.M. Hejazi, Fiber-reinforced asphalt-concrete - A review, Constr. Build. Mater. 24 (2010) 871–877.

[7]   M. Zaumanis, R.B. Mallick, Review of very high-content reclaimed asphalt use in plant-produced pavements: State of the art, Int. J. Pavement Eng. 16 (2015) 39–55.

[8]   S. Xu, A. García, J. Su, Q. Liu, A. Tabaković, E. Schlangen, Self-Healing Asphalt Review: From Idea to Practice, Adv. Mater. Interfaces. 5 (2018) 1800536.

[9]   V. Bobes-Jesus, P. Pascual-Muñoz, D. Castro-Fresno, J. Rodriguez-Hernandez, Asphalt solar collectors: A literature review, Appl. Energy. 102 (2013) 962–970.

[10]   Z.N. Kalantar, M.R. Karim, A. Mahrez, A review of using waste and virgin polymer in pavement, Constr.

Build. Mater. 33 (2012) 55–62.

[11] Z. Piao, P. Mikhailenko, M.R. Kakar, M. Bueno, S. Hellweg, L.D. Poulikakos, Urban mining for asphalt pavements: A review, J. Clean. Prod. 280 (2021) 124916.

[12] M.C. Cavalli, M. Zaumanis, E. Mazza, M.N. Partl, L.D. Poulikakos, Effect of ageing on the mechanical and chemical properties of binder from RAP treated with bio-based rejuvenators, Compos. Part B Eng. 141 (2018) 174–181.

[13] S.E. Zoorob, L.B. Suparma, Laboratory design and investigation of the properties of continuously graded Asphaltic concrete containing recycled plastics aggregate replacement (Plastiphalt), Cem. Concr. Compos. 22 (2000) 233–242.

[14] A.C. Raposeiras, D. Movilla-Quesada, R. Bilbao-Novoa, C. Cifuentes, G. Ferrer-Norambuena, D. Castro-Fresno, The use of copper slags as an aggregate replacement in asphalt mixes with RAP: Physical–chemical and mechanical behavioural analysis, Constr. Build. Mater. 190 (2018) 427–438.

[15] G. Ruiz, F. Chávez, S. Santamaría, W. Araujo, J. Timaná, R. Schmitt, Laboratory evaluation of seashells used as fine aggregate in hot mix asphalt, Int. J. Pavement Eng. 21 (2020) 620–628.

[16] W.M.N.W.A. Rahman, A.F.A. Wahab, Green pavement using recycled Polyethylene Terephthalate (PET) as partial fine aggregate replacement in modified asphalt, in: Procedia Eng., Elsevier Ltd, 2013: pp. 124–128.

[17] M. Shamsaei, I. Aghayan, K.A. Kazemi, Experimental

investigation of using cross-linked polyethylene waste as aggregate in roller compacted concrete pavement, J. Clean. Prod. 165 (2017) 290–297.

[18]   H.F. Hassan, Recycling of municipal solid waste incinerator ash in hot-mix asphalt concrete, Constr. Build. Mater. 19 (2005) 91–98.

[19]   Y. Xue, H. Hou, S. Zhu, J. Zha, Utilization of municipal solid waste incineration ash in stone mastic asphalt mixture: Pavement performance and environmental impact, Constr. Build. Mater. 23 (2009) 989–996.

[20]   M. Arabani, A.R. Azarhoosh, The effect of recycled concrete aggregate and steel slag on the dynamic properties of asphalt mixtures, Constr. Build. Mater. 35 (2012) 1–7.

[21]   H.A. Rondón-Quintana, J.C. Ruge-Cárdenas, M.M. de Farias, Behavior of Hot-Mix Asphalt Containing Blast Furnace Slag as Aggregate: Evaluation by Mass and Volume Substitution, J. Mater. Civ. Eng. 31 (2019) 04018364.

[22]   A.M. Babalghaith, S. Koting, N.H. Ramli Sulong, M.R. Karim, S.A. Mohammed, M.R. Ibrahim, Effect of palm oil clinker (POC) aggregate on the mechanical properties of stone mastic asphalt (SMA) mixtures, Sustainability. 12 (2020) 2716.

[23]   L. Flynn, Recycling: Will Roads Become'Linear Landfills'?, Roads Bridg. (1992).

[24]   F. Colangelo, R. Cioffi, Use of cement kiln dust, blast furnace slag and marble sludge in the manufacture of sustainable artificial aggregates by means of cold bonding pelletization, Materials (Basel). 6 (2013) 3139–3159.

[25]   M. Shi, T.C. Ling, B. Gan, M.Z. Guo, Turning concrete waste powder into carbonated artificial aggregates, Constr. Build. Mater. 199 (2019) 178–184.

[26]   E. Güneyisi, M. Gesoğlu, Ö. Pürsünlü, K. Mermerdaş, Durability aspect of concretes composed of cold bonded and sintered fly ash lightweight aggregates, Compos. Part B Eng. 53 (2013) 258–266.

[27]   F. Tajra, M.A. Elrahman, D. Stephan, The production and properties of cold-bonded aggregate and its applications in concrete: A review, Constr. Build. Mater. 225 (2019) 29–43.

[28]   K.S. Wang, C.J. Sun, C.C. Yeh, The thermotreatment of MSW incinerator fly ash for use as an aggregate: A study of the characteristics of size-fractioning, Resour. Conserv. Recycl. 35 (2002) 177–190.

[29]   C.R. Cheeseman, A. Makinde, S. Bethanis, Properties of lightweight aggregate produced by rapid sintering of incinerator bottom ash, Resour. Conserv. Recycl. 43 (2005) 147–162.

[30]   R. Cioffi, F. Colangelo, F. Montagnaro, L. Santoro, Manufacture of artificial aggregate using MSWI bottom ash, Waste Manag. 31 (2011) 281–288.

[31]   K. Tian, Y. Wang, S. Hong, J. Zhang, D. Hou, B. Dong, F. Xing, Alkali-activated artificial aggregates fabricated by red mud and fly ash: Performance and microstructure, Constr. Build. Mater. 281 (2021) 122552.

[32]   M.S. Nadesan, P. Dinakar, Structural concrete using sintered flyash lightweight aggregate: A review, Constr. Build. Mater. 154 (2017) 928–944.

[33]   T. Hales, M. Adams, G. Bauer, T.D. Dang, J. Harrison, L.T. Hoang, C. Kaliszyk, V. Magron, S. McLaughlin, T.T. Nguyen, Q.T. Nguyen, T. Nipkow, S. Obua, J. Pleso, J. Rute, A. Solovyev, T.H.A. Ta, N.T. Tran, T.D. Trieu, J. Urban, K. Vu, R. Zumkeller, A formal proof of the Kepler conjecture, Forum Math. Pi. 5 (2017) 29.

[34]   J.C. Tsai, G.A. Voth, J.P. Gollub, Internal Granular Dynamics, Shear-Induced Crystallization, and Compaction Steps, Phys. Rev. Lett. 91 (2003) 064301.

[35]   K. Asencio, M. Acevedo, I. Zuriguel, D. Maza, Experimental Study of Ordering of Hard Cubes by Shearing, Phys. Rev. Lett. 119 (2017) 228002.

[36]   G.D. Scott, D.M. Kilgour, The density of random close packing of spheres, J. Phys. D. Appl. Phys. 2 (1969) 863–866.

[37]   A. Wouterse, S.R. Williams, A.P. Philipse, Effect of particle shape on the density and microstructure of random packings, J. Phys. Condens. Matter. 19 (2007) 406215.

[38]   S. Torquato, T.M. Truskett, P.G. Debenedetti, Is random close packing of spheres well defined?, Phys. Rev. Lett. 84 (2000) 2064–2067.

[39]   R.P. Behringer, B. Chakraborty, The physics of jamming for granular materials: a review, Reports Prog. Phys. 82 (2019) 012601.

[40]   A. Donev, F.H. Stillinger, P.M. Chaikin, S. Torquato, Unusually dense crystal packings of ellipsoids, Phys. Rev. Lett. 92 (2004) 255506.

[41]   A. Donev, I. Cisse, D. Sachs, E.A. Variano, F.H. Stillinger, R. Connelly, S. Torquato, P.M. Chaikin,

Improving the density of jammed disordered packings using ellipsoids., Science. 303 (2004) 990–3.

[42]   W. Man, A. Donev, F.H. Stillinger, M.T. Sullivan, W.B. Russel, D. Heeger, S. Inati, S. Torquato, P.M. Chaikin, Experiments on random packings of ellipsoids, Phys. Rev. Lett. 94 (2005) 198001.

[43]   G.W. Delaney, P.W. Cleary, The packing properties of superellipsoids, EPL. 89 (2010) 34002.

[44]   Z.-Y. Zhou, R.-P. Zou, D. Pinson, A.-B. Yu, Dynamic Simulation of the Packing of Ellipsoidal Particles, Ind. Eng. Chem. Res. 50 (2011) 9787–9798.

[45]   S. Zhao, N. Zhang, X. Zhou, L. Zhang, Particle shape effects on fabric of granular random packing, Powder Technol. 310 (2017) 175–186.

[46]   G. Lu, J.R. Third, C.R. Müller, Critical assessment of two approaches for evaluating contacts between super-quadric shaped particles in DEM simulations, Chem. Eng. Sci. 78 (2012) 226–235.

[47]   A.H. Barr, Superquadrics and Angle-Preserving Transformations, IEEE Comput. Graph. Appl. 1 (1981) 11–23.

[48]   Y. Jiao, F.H. Stillinger, S. Torquato, Distinctive features arising in maximally random jammed packings of superballs, Phys. Rev. E. 81 (2010) 041304.

[49]   R.M. Baram, P.G. Lind, Deposition of general ellipsoidal particles, Phys. Rev. E. 85 (2012) 041301.

[50]   L.J.H. Seelen, J.T. Padding, J.A.M. Kuipers, A granular Discrete Element Method for arbitrary convex particle shapes: Method and packing generation, Chem. Eng.

Sci. 189 (2018) 84–101.

[51]   S.R. Williams, A.P. Philipse, Random packings of spheres and spherocylinders simulated by mechanical contraction, Phys. Rev. E. 67 (2003) 051301.

[52]   C.R.A. Abreu, F.W. Tavares, M. Castier, Influence of particle shape on the packing and on the segregation of spherocylinders via Monte Carlo simulations, Powder Technol. 134 (2003) 167–180.

[53]   A. Baule, R. Mari, L. Bo, L. Portal, H.A. Makse, Mean-field theory of random close packings of axisymmetric particles, Nat. Commun. 4 (2013) 2194.

[54]   A. Haji-Akbari, M. Engel, A.S. Keys, X. Zheng, R.G. Petschek, P. Palffy-Muhoray, S.C. Glotzer, Disordered, quasicrystalline and crystalline phases of densely packed tetrahedra, Nature. 462 (2009) 773–777.

[55]   A. Jaoshvili, A. Esakia, M. Porrati, P.M. Chaikin, Experiments on the Random Packing of Tetrahedral Dice, Phys. Rev. Lett. 104 (2010) 1–4.

[56]   M. Neudecker, S. Ulrich, S. Herminghaus, M. Schröter, Jammed Frictional Tetrahedra are Hyperstatic, Phys. Rev. Lett. 111 (2013) 028001.

[57]   S. Torquato, Y. Jiao, Dense packings of polyhedra: Platonic and Archimedean solids, Phys. Rev. E. 80 (2009) 041104.

[58]   L. Babout, K. Grudzień, J. Wiącek, M. Niedostatkiewicz, B. Karpiński, M. Szkodo, Selection of material for X-ray tomography analysis and DEM simulations: comparison between granular materials of biological and non-biological origins, Granul. Matter 2018 203. 20 (2018) 1–14.

[59]   G.-C. Cho, J. Dodds, J.C. Santamarina, Particle Shape Effects on Packing Density, Stiffness, and Strength: Natural and Crushed Sands, J. Geotech. Geoenvironmental Eng. 132 (2006) 591–602.

[60]   I. Malinouskaya, V. V. Mourzenko, J.-F. Thovert, P.M. Adler, Random packings of spiky particles: Geometry and transport properties, Phys. Rev. E. 80 (2009) 011304.

[61]   N. Gravish, S. V. Franklin, D.L. Hu, D.I. Goldman, Entangled granular media, Phys. Rev. Lett. 108 (2012) 208001.

[62]   K.A. Murphy, N. Reiser, D. Choksy, C.E. Singer, H.M. Jaeger, Freestanding loadbearing structures with Z-shaped particles, Granul. Matter. 18 (2016) 26.

[63]   A.G. Athanassiadis, M.Z. Miskin, P. Kaplan, N. Rodenberg, S.H. Lee, J. Merritt, E. Brown, J. Amend, H. Lipson, H.M. Jaeger, Particle shape effects on the stress response of granular packings., Soft Matter. 10 (2014) 48–59.

[64]   L. Meng, S. Li, X. Yao, Maximally dense random packings of intersecting spherocylinders with central symmetry, Powder Technol. 314 (2017) 49–58.

[65]   L. Meng, C. Wang, X. Yao, Non-convex shape effects on the dense random packing properties of assembled rods, Phys. A Stat. Mech. Its Appl. 490 (2018) 212–221.

[66]   L. Meng, X. Yao, X. Zhang, Effects of central symmetry and elongation on the dense disordered packings of entangled particles, Phys. A Stat. Mech. Its Appl. 523 (2019) 120–128.

[67]   A. Donev, R. Connelly, F.H. Stillinger, S. Torquato,

Underconstrained jammed packings of nonspherical hard particles: Ellipses and ellipsoids, Phys. Rev. E - Stat. Nonlinear, Soft Matter Phys. 75 (2007) 1–32.

[68]   C. Song, P. Wang, H.A. Makse, A phase diagram for jammed matter, Nature. 453 (2008) 629–632.

[69]   S. Papanikolaou, C.S. O'Hern, M.D. Shattuck, Isostaticity at Frictional Jamming, Phys. Rev. Lett. 110 (2013) 198002.

[70]   K. VanderWerf, W. Jin, M.D. Shattuck, C.S. O'Hern, Hypostatic jammed packings of frictionless nonspherical particles, Phys. Rev. E. 97 (2017) 012909.

[71]   M. Neudecker, S. Ulrich, S. Herminghaus, M. Schröter, Jammed Frictional Tetrahedra are Hyperstatic, Phys. Rev. Lett. 111 (2013) 028001.

[72]   A. Drescher, G. de Josselin de Jong, Photoelastic verification of a mechanical model for the flow of a granular material, J. Mech. Phys. Solids. 20 (1972) 337–340.

[73]   A. Abed Zadeh, J. Barés, T.A. Brzinski, K.E. Daniels, J. Dijksman, N. Docquier, H.O. Everitt, J.E. Kollmer, O. Lantsoght, D. Wang, M. Workamp, Y. Zhao, H. Zheng, Enlightening force chains: a review of photoelasticimetry in granular matter, Granul. Matter. 21 (2019) 1–12.

[74]   T.S. Majmudar, R.P. Behringer, Contact force measurements and stress-induced anisotropy in granular materials., Nature. 435 (2005) 1079–1082.

[75]   J.A. Dijksman, L. Kovalcinova, J. Ren, R.P. Behringer, M. Kramar, K. Mischaikow, L. Kondic, Characterizing granular networks using topological metrics, Phys. Rev.

E. 97 (2018).

[76] J.E. Kollmer, K.E. Daniels, Betweenness centrality as predictor for forces in granular packings, Soft Matter. 15 (2019) 1793–1798.

[77] L. Papadopoulos, M.A. Porter, K.E. Daniels, D.S. Bassett, Network analysis of particles and grains, J. Complex Networks. 6 (2018) 485–565.

[78] D.M. Mueth, H.M. Jaeger, S.R. Nagel, Force distribution in a granular medium, Phys. Rev. E. 57 (1998) 3164–3169.

[79] J.Q. Gan, Z.Y. Zhou, A.B. Yu, Interparticle force analysis on the packing of fine ellipsoids, Powder Technol. 320 (2017) 610–624.

[80] P.A. Cundall, O.D.L. Strack, A discrete numerical model for granular assemblies, Geotechnique. 29 (1979) 47–65.

[81] G. Lu, J.R.R. Third, C.R.R. Müller, Discrete element models for non-spherical particle systems: From theoretical developments to applications, Chem. Eng. Sci. 127 (2015) 425–465.

[82] J. Third, Modelling Particle Motion within Rotating Cylinders, Ph.D. thesis, University of Cambridge, 2009.

[83] J.R. Williams, R. O'Connor, Discrete Element Simulation and the Contact Problem, Arch. Comput. Methods Eng. 6 (1999) 279–304.

[84] J.R. Williams, R. O'connor, A linear complexity intersection algorithm for discrete element simulation of arbitrary geometries, Eng. Comput. 12 (1995) 185–201.

[85]   R. Cai, L. Xu, J. Zheng, Y. Zhao, Modified cell-linked list method using dynamic mesh for discrete element method, Powder Technol. 340 (2018) 321–330.

[86]   Y. Guo, C. Wassgren, W. Ketterhagen, B. Hancock, J. Curtis, Some computational considerations associated with discrete element modeling of cylindrical particles, Powder Technol. 228 (2012) 193–198.

[87]   Vladimir J. Lumelsky, On Fast Computation of Distance Between Line Segments, Inf. Process. Lett. 21 (1985) 55–61.

[88]   R. Kumar, A. Sarkar, W. Ketterhagen, B. Hancock, J. Curtis, C. Wassgren, Influence of normal contact force model on simulations of spherocylindrical particles, AIChE J. 64 (2018) 1986–2001.

[89]   M. Kodam, R. Bharadwaj, J. Curtis, B. Hancock, C. Wassgren, Force model considerations for glued-sphere discrete element method simulations, Chem. Eng. Sci. 64 (2009) 3466–3475.

[90]   D. Höhner, S. Wirtz, H. Kruggel-Emden, V. Scherer, Comparison of the multi-sphere and polyhedral approach to simulate non-spherical particles within the discrete element method: Influence on temporal force evolution for multiple contacts, Powder Technol. 208 (2011) 643–656.

[91]   T. Kidokoro, R. Arai, M. Saeki, Investigation of dynamics simulation of granular particles using spherocylinder model, Granul. Matter. 17 (2015) 743–751.

[92]   B.H. Nam, Z. Behring, J. Kim, M. Chopra, others, Evaluate the use of reclaimed concrete aggregate in french drain applications., 2014.

[93] S. Takahashi, M.N. Partl, Improvement of Mix Design for Porous Asphalt, Road Mater. Pavement Des. 2 (2001) 283–296.

[94] H. Boler, Y. Qian, E. Tutumluer, Influence of Size and Shape Properties of Railroad Ballast on Aggregate Packing, Transp. Res. Rec. J. Transp. Res. Board. 2448 (2014) 94–104.

[95] I. Gruber, I. Zinovik, L. Holzer, A. Flisch, L.D. Poulikakos, A computational study of the effect of structural anisotropy of porous asphalt on hydraulic conductivity, Constr. Build. Mater. 36 (2012) 66–77.

[96] A. Kia, H.S. Wong, C.R. Cheeseman, Clogging in permeable concrete: A review, J. Environ. Manage. 193 (2017) 221–233.

[97] J. Hu, Z. Qian, P. Liu, D. Wang, M. Oeser, Investigation on the permeability of porous asphalt concrete based on microstructure analysis, Int. J. Pavement Eng. (2019) 1–11.

[98] A. García, M.N. Partl, How to transform an asphalt concrete pavement into a solar turbine, Appl. Energy. 119 (2014) 431–437.

[99] A.J. Arnfield, Two decades of urban climate research: a review of turbulence, exchanges of energy and water, and the urban heat island, Int. J. Climatol. 23 (2003) 1–26.

[100] A. Chiarelli, A. Al-Mohammedawi, A.R. Dawson, A. García, Construction and configuration of convection-powered asphalt solar collectors for the reduction of urban temperatures, Int. J. Therm. Sci. 112 (2017) 242.

[101] Y. Liu, T. Li, L. Yu, Urban heat island mitigation and

hydrology performance of innovative permeable pavement: A pilot-scale study, J. Clean. Prod. 244 (2020) 118938.

[102] T.N. Mansour, B.J. Putman, Influence of Aggregate Gradation on the Performance Properties of Porous Asphalt Mixtures, J. Mater. Civ. Eng. 25 (2013) 281–288.

[103] H. Darcy, Les fontaines publiques de la ville de Dijon: exposition et application..., Victor Dalmont, 1856.

[104] J. Kozeny, Über kapillare Leitung des Wassers im Boden, R. Acad. Sci. Vienna, Proc. Cl. I. 136 (1927) 271–306.

[105] P.C. Carman, Fluid Flow through Granular Beds, Trans. Inst. Chem. Eng. 15 (1937) 150–166.

[106] P.C. Carman, Flow of Gases through Porous Media, Academic Press, New York, 1956.

[107] A. Cancelliere, C. Chang, E. Foti, D.H. Rothman, S. Succi, The permeability of a random medium: Comparison of simulation with theory, Phys. Fluids A. 2 (1990) 2085–2088.

[108] E. Rodriguez, F. Giacomelli, A. Vazquez, Permeability-Porosity Relationship in RTM for Different Fiberglass and Natural Reinforcements, J. Compos. Mater. 38 (2004) 259–268.

[109] N. Henderson, J.C. Brêttas, W.F. Sacco, A three-parameter Kozeny-Carman generalized equation for fractal porous media, Chem. Eng. Sci. 65 (2010) 4432–4442.

[110] R. Zhong, M. Xu, R. Vieira Netto, K. Wille, Influence

of pore tortuosity on hydraulic conductivity of pervious concrete: Characterization and modeling, Constr. Build. Mater. 125 (2016) 1158–1168.

[111] A. Koponen, M. Kataja, J. Timonen, Permeability and effective porosity of porous media, Phys. Rev. E - Stat. Physics, Plasmas, Fluids, Relat. Interdiscip. Top. 56 (1997) 3319–3325.

[112] M. Smith, L. Collis, Aggregates: Sand, gravel and crushed rock aggregates for construction purposes, The Geological Society, 2001.

[113] K. Dierichs, A. Menges, Towards an aggregate architecture: designed granular systems as programmable matter in architecture, Granul. Matter. 18 (2016) 25.

[114] K. Murphy, L. Roth, D. Peterman, H. Jaeger, Aleatory Construction Based on Jamming: Stability Through Self-Confinement, Archit. Des. 87 (2017) 74–81.

[115] H.. Burcharth, K. D'Angremond, J.. van der Meer, Z. Liu, Empirical formula for breakage of Dolosse and Tetrapods, Coast. Eng. 40 (2000) 183–206.

[116] N.A. Conzelmann, L. Gorjan, F. Sarraf, L.D. Poulikakos, M.N. Partl, C.R. Müller, F.J. Clemens, Manufacturing complex Al2O3 ceramic structures using consumer-grade fused deposition modelling printers, Rapid Prototyp. J. 26 (2020) 1035–1048.

[117] S. V. Franklin, Geometric cohesion in granular materials, Phys. Today. 65 (2012) 70–71.

[118] N.A. Conzelmann, A. Penn, M.N. Partl, F.J. Clemens, L.D. Poulikakos, C.R. Müller, Link between packing morphology and the distribution of contact forces and

211

stresses in packings of highly nonconvex particles, Phys. Rev. E. 102 (2020) 062902.

[119] H.K. Kim, H.K. Lee, Acoustic absorption modeling of porous concrete considering the gradation and shape of aggregates and void ratio, J. Sound Vib. 329 (2010) 866–879.

[120] Y. Zhao, J. Barés, J.E.S. Socolar, Yielding, rigidity, and tensile stress in sheared columns of hexapod granules, Phys. Rev. E. 101 (2020) 062903.

[121] G. Lu, J.R. Third, C.R. Müller, Effect of particle shape on domino wave propagation: A perspective from 3D, anisotropic discrete element simulations, Granul. Matter. 16 (2014) 107–114.

[122] G. Lu, J.R. Third, C.R. Müller, The parameters governing the coefficient of dispersion of cubes in rotating cylinders, Granul. Matter. 19 (2017) 12.

[123] G. Lu, C.R. Müller, Particle-shape induced radial segregation in rotating cylinders, Granul. Matter. 22 (2020) 50.

[124] M. Dawoud, I. Taha, S.J. Ebeid, Effect of processing parameters and graphite content on the tribological behaviour of 3D printed acrylonitrile butadiene styrene, Materwiss. Werksttech. 46 (2015) 1185–1195.

[125] S. Luding, Collisions & Contacts between Two Particles, in: H.J. Herrmann (Ed.), Phys. Dry Granul. Media, Springer Netherlands, 1998: pp. 285–304.

[126] M. Paulick, M. Morgeneyer, A. Kwade, Review on the influence of elastic particle properties on DEM simulation results, Powder Technol. 283 (2015) 66–76.

[127] Y. Yang, J.F. Wang, Y.M. Cheng, Quantified evaluation of particle shape effects from micro-to-macro scales for non-convex grains, Particuology. 25 (2016) 23–35.

[128] Persistence of Vision Pty. Ltd. (2004) Persistence of Vision Raytracer (Version 3.6) [Computer software]. Retrieved from http://www.povray.org/, (n.d.).

[129] M. Ben Clennell, Tortuosity: a guide through the maze, Geol. Soc. London, Spec. Publ. 122 (1997) 299–344.

[130] A. Duda, Z. Koza, M. Matyka, Hydraulic tortuosity in arbitrary porous media flow, Phys. Rev. E - Stat. Nonlinear, Soft Matter Phys. 84 (2011) 036319.

[131] J. Latt, O. Malaspinas, D. Kontaxakis, A. Parmigiani, D. Lagrava, F. Brogi, M. Ben Belgacem, Y. Thorimbert, S. Leclaire, S. Li, F. Marson, J. Lemus, C. Kotsalos, R. Conradin, C. Coreixas, R. Petkantchin, F. Raynaud, J. Beny, B. Chopard, Palabos: Parallel Lattice Boltzmann Solver, Comput. Math. with Appl. 81 (2021) 334–350.

[132] Z. Guo, B. Shi, N. Wang, Lattice BGK Model for Incompressible Navier-Stokes Equation, J. Comput. Phys. 165 (2000) 288–306.

[133] Trimesh (2020) [Computer software]. Retrieved from https://github.com/mikedh/trimesh, (n.d.).

[134] C. Ferreiro-Córdova, J.S. Van Duijneveldt, Random packing of hard spherocylinders, J. Chem. Eng. Data. 59 (2014) 3055–3060.

[135] H. Pourtavakoli, E.J.R. Parteli, T. Pöschel, Granular dampers: Does particle shape matter?, New J. Phys. 18 (2016) 73049.

213

[136] L. Shen, Z. Chen, Critical review of the impact of tortuosity on diffusion, Chem. Eng. Sci. 62 (2007) 3748–3755.

[137] M. Matyka, A. Khalili, Z. Koza, Tortuosity-porosity relation in porous media flow, Phys. Rev. E - Stat. Nonlinear, Soft Matter Phys. 78 (2008) 026306.

[138] B. Ghanbarian, A.G. Hunt, R.P. Ewing, M. Sahimi, Tortuosity in Porous Media: A Critical Review, Soil Sci. Soc. Am. J. Soil Sci. Soc. Am. J. 77 (2013) 1461–1477.

[139] S. Khirevich, A. Höltzel, A. Daneyko, A. Seidel-Morgenstern, U. Tallarek, Structure-transport correlation for the diffusive tortuosity of bulk, monodisperse, random sphere packings, J. Chromatogr. A. 1218 (2011) 6489–6497.

[140] D.S. Tsai, W. Strieder, Effective Conductivities of Random Fiber Bedst, Chem. Eng. Commun. 40 (1986) 207–218.

[141] S. Feranie, F.D.E. Latief, Tortuosity-porosity relationship in two-dimensional fractal model of porous media, Fractals. 21 (2013) 1350013.

[142] S. Hou, A lattice Boltzmann subgrid model for high Reynolds number flows., Fields Inst. Comm. 6 (1996) 151–66.

[143] B. Indraratna, D. Ionescu, H.D. Christie, Shear Behavior of Railway Ballast Based on Large-Scale Triaxial Tests, J. Geotech. Geoenvironmental Eng. 124 (1998) 439–449.

[144] L.D. Poulikakos, M.N. Partl, Investigation of porous asphalt microstructure using optical and electron

microscopy, J. Microsc. 240 (2010) 145–154.

[145] N. Kaliyan, R.V. Morey, D.R. Schmidt, Roll press compaction of corn stover and perennial grasses to increase bulk density, Biomass and Bioenergy. 55 (2013) 322–330.

[146] R. Linemann, J. Runge, M. Sommerfeld, U. Weißgüttel, Compaction of Powders due to Vibrations and Shocks, Part. Part. Syst. Charact. 21 (2004) 261–267.

[147] C. -h. Liu, S.R. Nagel, D.A. Schecter, S.N. Coppersmith, S. Majumdar, O. Narayan, T.A. Witten, Force fluctuations in bead packs, Science. 269 (1995) 513–515.

[148] R.C. Hidalgo, C.U. Grosse, F. Kun, H.W. Reinhardt, H.J. Herrmann, Evolution of Percolating Force Chains in Compressed Granular Media, Phys. Rev. Lett. 89 (2002) 205501.

[149] A. Rechenmacher, S. Abedi, O. Chupin, Evolution of force chains in shear bands in sands, Geotech. London. 60 (2010) 343–351.

[150] M. Oda, H. Kazama, Microstructure of shear bands and its relation to the mechanisms of dilatancy and failure of dense granular soils, Géotechnique. 48 (1998) 465–481.

[151] H. Laubie, F. Radjai, R. Pellenq, F.-J. Ulm, Stress Transmission and Failure in Disordered Porous Media, Phys. Rev. Lett. 119 (2017) 1–6.

[152] B. Saint-Cyr, J.-Y. Delenne, C. Voivret, F. Radjai, P. Sornay, Rheology of granular materials composed of nonconvex particles, Phys. Rev. E. 84 (2011) 041302.

215

[153] E. Azéma, F. Radjaï, Force chains and contact network topology in sheared packings of elongated particles, Phys. Rev. E. 85 (2012) 031303.

[154] S. Luding, Stress distribution in static two-dimensional granular model media in the absence of friction, Phys. Rev. E - Stat. Physics, Plasmas, Fluids, Relat. Interdiscip. Top. 55 (1997) 4720–4729.

[155] J. Jose, A. van Blaaderen, A. Imhof, A. Imhof, Random three-dimensional jammed packings of elastic shells acting as force sensors., Phys. Rev. E. 93 (2016) 062901.

[156] E. Olsson, D. Jelagin, M.N. Partl, New discrete element framework for modelling asphalt compaction, Road Mater. Pavement Des. 20 (2019) S604–S616.

[157] Y. Zhao, K. Liu, M. Zheng, J. Barés, K. Dierichs, A. Menges, R.P. Behringer, Packings of 3D stars: stability and structure, Granul. Matter. 18 (2016) 24.

[158] P. Aejmelaeus-Lindström, J. Willmann, S. Tibbits, F. Gramazio, M. Kohler, Jammed architectural structures: towards large-scale reversible construction, Granul. Matter. 18 (2016) 28.

[159] H.P. Zhu, Z.Y. Zhou, R.Y. Yang, A.B. Yu, Discrete particle simulation of particulate systems: Theoretical developments, Chem. Eng. Sci. 62 (2007) 3378–3396.

[160] G. Lu, R.C. Hidalgo, J.R. Third, C.R. Müller, Ordering and stress transmission in packings of straight and curved spherocylinders, Granul. Matter. 18 (2016) 34.

[161] T. Schwager, T. Pöschel, Coefficient of restitution and linear-dashpot model revisited, Granul. Matter. 9 (2007) 465–469.

[162] L.E. Silbert, D. Ertaş, G.S. Grest, T.C. Halsey, D. Levine, S.J. Plimpton, Granular flow down an inclined plane: Bagnold scaling and rheology, Phys. Rev. E - Stat. Physics, Plasmas, Fluids, Relat. Interdiscip. Top. 64 (2001) 14.

[163] J.R. Third, C.R. Müller, Is axial dispersion within rotating cylinders governed by the Froude number?, Phys. Rev. E - Stat. Nonlinear, Soft Matter Phys. 86 (2012).

[164] M.J. Jiang, J.M. Konrad, S. Leroueil, An efficient technique for generating homogeneous specimens for DEM studies, Comput. Geotech. 30 (2003) 579–597.

[165] A. Wachs, L. Girolami, G. Vinay, G. Ferrer, Grains3D, a flexible DEM approach for particles of arbitrary convex shape — Part I: Numerical model and validations, Powder Technol. 224 (2012) 374–389.

[166] F. Ludewig, N. Vandewalle, Strong interlocking of nonconvex particles in random packings, Phys. Rev. E. 85 (2012) 051307.

[167] R.J. Bathurst, L. Rothenburg, Micromechanical aspects of isotropic granular assemblies with linear contact interactions, J. Appl. Mech. Trans. ASME. 55 (1988) 17–23.

[168] T. Marschall, S. Teitel, Compression-driven jamming of athermal frictionless spherocylinders in two dimensions, Phys. Rev. E. 97 (2018) 012905.

[169] J. Zhao, S. Li, R. Zou, A. Yu, Dense random packings of spherocylinders, Soft Matter. 8 (2012) 1003–1009.

[170] R.C. Hidalgo, I. Zuriguel, D. Maza, I. Pagonabarraga, Granular packings of elongated faceted particles

217

deposited under gravity, J. Stat. Mech. Theory Exp. 2010 (2010) P06025.

[171]   S.E. Phan, W.B. Russel, J. Zhu, P.M. Chaikin, Effects of polydispersity on hard sphere crystals, J. Chem. Phys. 108 (1998) 9789–9795.

[172]   N. Estrada, A. Taboada, F. Radjaï, Shear strength and force transmission in granular media with rolling resistance, Phys. Rev. E - Stat. Nonlinear, Soft Matter Phys. 78 (2008) 1–11.

[173]   B. Berman, 3-D printing: The new industrial revolution, Bus. Horiz. 55 (2012) 155–162.

[174]   N. Travitzky, A. Bonet, B. Dermeik, T. Fey, I. Filbert-Demut, L. Schlier, T. Schlordt, P. Greil, Additive Manufacturing of Ceramic-Based Materials, Adv. Eng. Mater. 16 (2014) 729–754.

[175]   S. Rangarajan, G. Qi, A. Bandyopadhyay, C. Dai, J.W. Han, P. Bharagava, S. Wu, A. Safari, S.C. Danforth, The role of materials processing variables in FDC process, Proc. Ofthe Solid Free. Fabr. Symp. 4 (1997) 431–440.

[176]   I. Grida, J.R.G. Evans, Extrusion freeforming of ceramics through fine nozzles, J. Eur. Ceram. Soc. 23 (2003) 629–635.

[177]   M.K. Agarwala, V.R. Jamalabad, N.A. Langrana, A. Safari, P.J. Whalen, S.C. Danforth, Structural quality of parts processed by fused deposition, Rapid Prototyp. J. 2 (1996) 4–19.

[178]   O.A. Mohamed, S.H. Masood, J.L. Bhowmik, Optimization of fused deposition modeling process parameters: a review of current research and future

prospects, Adv. Manuf. 3 (2015) 42–53.

[179] S. Danforth, Fused Deposition of Ceramics: A New Technique for the Rapid Fabrication of Ceramic Components, Mater. Technol. 10 (1995) 144–146.

[180] J.A. Lewis, Binder Removal from Ceramics, Annu. Rev. Mater. Sci. 27 (1997) 147–173.

[181] F. Clemens, Thermoplastic Extrusion for Ceramic Bodies, in: Extrus. Ceram., Springer, Berlin, Heidelberg, 2009: pp. 295–311.

[182] G. Bandyopadhyay, K.W. French, Injection-molded ceramics: Critical aspects of the binder removal process and component fabrication, J. Eur. Ceram. Soc. 11 (1993) 23–34.

[183] R.K. Enneti, S.J. Park, R.M. German, S. V. Atre, Review: Thermal Debinding Process in Particulate Materials Processing, Mater. Manuf. Process. 27 (2012) 103–118.

[184] T. Chartier, M. Ferrato, J.F. Baumard, Supercritical Debinding of Injection Molded Ceramics, J. Am. Ceram. Soc. 78 (1995) 1787–1792.

[185] M. Trunec, J. Cihlar, Thermal removal of multicomponent binder from ceramic injection mouldings, J. Eur. Ceram. Soc. 22 (2002) 2231–2241.

[186] L. Gorjan, T. Lusiola, D. Scharf, F. Clemens, Kinetics and equilibrium of Eco-debinding of PZT ceramics shaped by thermoplastic extrusion, J. Eur. Ceram. Soc. 37 (2017) 5273–5280.

[187] L. Gorjan, Wick Debinding - An Effective Way of Solving Problems in the Debinding Process of Powder

Injection Molding, in: Some Crit. Issues Inject. Molding, InTech, 2012.

[188] L. Gorjan, G. Blugan, T. Graule, J. Kuebler, Effectiveness of wick-debinding inside powder bed for ceramic laminates made by tape casting, Powder Technol. 273 (2015) 197–202.

[189] M. Bach, T. Sebastian, M. Melnykowycz, T. Lusiola, D. Scharf, F. Clemens, Additive Manufacturing of Piezoelectric 3-3 Composite Structures, in: Ind. Addit. Manuf. - Proc. Addit. Manuf. Prod. Appl. - AMPA2017, Springer International Publishing, Cham, 2018: pp. 93–103.

[190] S.L. Ho, S.F. Yang, C.K. Chua, K.F. Leong, C.M. Cheah, M.H. Too, Z.H. Du, Investigation of 3D Non-Random Porous Structures by Fused Deposition Modelling, Int. J. Adv. Manuf. Technol. 19 (2002) 217–223.

[191] M. Houmard, Q. Fu, M. Genet, E. Saiz, A.P. Tomsia, On the structural, mechanical, and biodegradation properties of HA/β-TCP robocast scaffolds, J. Biomed. Mater. Res. Part B Appl. Biomater. 101 (2013) 1233–1242.

[192] D.-W. Jang, R.A. Franco, S.K. Sarkar, B.-T. Lee, Fabrication of porous hydroxyapatite scaffolds as artificial bone preform and its biocompatibility evaluation., ASAIO J. 60 (2014) 216–23.

[193] L. Gorjan, L. Reiff, A. Liersch, F. Clemens, Ethylene vinyl acetate as a binder for additive manufacturing of tricalcium phosphate bio-ceramics, Ceram. Int. 44 (2018) 15817–15823.

[194] S. Rangarajan, I. Pozsgai, J. McIntosh, R. McCuiston,

B.L. Harper, N. Langrana, A. Safari, S.C. Danforth, R.B. Clancy, C. Gasdaska, P.J. Whalen, Homogeneity, Anisotropy, and Texture In Si3n4 Ceramics made by Fused Deposition, MRS Proc. 542 (1998) 97.

[195] D. Nemec, J. Levec, Flow through packed bed reactors: 1. Single-phase flow, Chem. Eng. Sci. 60 (2005) 6947–6957.

[196] J.J. Stempihar, T. Pourshams-Manzouri, K.E. Kaloush, M.C. Rodezno, Porous Asphalt Pavement Temperature Effects for Urban Heat Island Analysis, Transp. Res. Rec. J. Transp. Res. Board. 2293 (2012) 123–130.

[197] S.H. Ahn, M. Montero, D. Odell, S. Roundy, P.K. Wright, Anisotropic material properties of fused deposition modeling ABS, Rapid Prototyp. J. 8 (2002) 248–257.

[198] J.E. Zorzi, C.A. Perottoni, J.A.H. Da Jornada, Hard-skin development during binder removal from Al2O3-based green ceramic bodies, J. Mater. Sci. 37 (2002) 1801–1807.

[199] R. Melcher, N. Travitzky, C. Zollfrank, P. Greil, 3D printing of Al2O3/Cu–O interpenetrating phase composite, J. Mater. Sci. 46 (2011) 1203–1210.

[200] V.M. Beresnev, M.Y. Smolyakova, A.D. Pogrebnyak, A.S. Kaverina, A.A. Drobyshevskaya, E.A. Svetlichnyy, D.A. Kolesnikov, Studying tribological characteristics of alumina- and zirconia-based ceramics, J. Frict. Wear. 35 (2014) 137–140.

[201] Z. Károly, C. Balázsi, K. Balázsi, A. Petrik, J. Lábár, A. Dhar, Hybride aluminum matrix composites prepared by spark plasma sintering (SPS), Eur. Chem. Bull. 3 (2014) 247–250.

[202] I. Lauria, M. Kramer, T. Schröder, S. Kant, A. Hausmann, F. Böke, R. Leube, R. Telle, H. Fischer, Inkjet printed periodical micropatterns made of inert alumina ceramics induce contact guidance and stimulate osteogenic differentiation of mesenchymal stromal cells, Acta Biomater. 44 (2016) 85–96.

[203] D.A. Polsakiewicz, W. Kollenberg, Highly loaded alumina inks for use in a piezoelectric print head, Materwiss. Werksttech. 42 (2011) 812–819.

[204] J. Chovanec, D. Galusek, J. Ráheμ, P. Šajgalík, Low loss alumina dielectrics by aqueous tape casting: The influence of composition on the loss tangent, Ceram. Int. 38 (2012) 3747–3755.

[205] F. del Río, M.G. Boado, A. Rama, F. Guitián, A comparative study on different aqueous-phase graphite exfoliation methods for few-layer graphene production and its application in alumina matrix composites, J. Eur. Ceram. Soc. 37 (2017) 3681–3693.

[206] S.W. Kim, H.-W. Lee, H. Song, Effect of minor binder on capillary structure evolution during wicking, Ceram. Int. 25 (1999) 671–676.

[207] K.E. Hrdina, J.W. Halloran, A. Oliveira, M. Kaviany, Chemistry of removal of ethylene vinyl acetate binders, J. Mater. Sci. 33 (1998) 2795–2803.

[208] K.E. Hrdina, J.W. Halloran, M. Kaviany, A. Oliveira, Defect formation during binder removal in ethylene vinyl acetate filled system, J. Mater. Sci. 34 (1999) 3281–3290.

[209] U.F. Vogt, M. Gorbar, P. Dimopoulos-Eggenschwiler, A. Broenstrup, G. Wagner, P. Colombo, Improving the properties of ceramic foams by a vacuum infiltration

process, J. Eur. Ceram. Soc. 30 (2010) 3005–3011.

[210] R.G. Munro, Evaluated Material Properties for a Sintered alpha-Alumina, J. Am. Ceram. Soc. 80 (1997) 1919–1928.

[211] L. Gorjan, A. Dakskobler, T. Kosmač, Strength Evolution of Injection-Molded Ceramic Parts During Wick-Debinding, J. Am. Ceram. Soc. 95 (2012) 188–193.

[212] K.E. Hrdina, J.W. Halloran, Dimensional changes during binder removal in a mouldable ceramic system, J. Mater. Sci. 33 (1998) 2805–2815.

[213] T. Börzsönyi, B. Szabó, G. Törös, S. Wegner, J. Török, E. Somfai, T. Bien, R. Stannarius, Orientational Order and Alignment of Elongated Particles Induced by Shear, Phys. Rev. Lett. 108 (2012) 228302.

[214] D.B. Nagy, P. Claudin, T. Börzsönyi, E. Somfai, Rheology of dense granular flows for elongated particles, Phys. Rev. E. 96 (2017) 062903.

[215] G.A. Patterson, P.I. Fierens, F. Sangiuliano Jimka, P.G. König, A. Garcimartín, I. Zuriguel, L.A. Pugnaloni, D.R. Parisi, Clogging Transition of Vibration-Driven Vehicles Passing through Constrictions, Phys. Rev. Lett. 119 (2017) 248301.

[216] A.B.M. Saifullah, S.H. Masood, Cycle time reduction in injection moulding with conformal cooling channels, in: Conf. Proc. Int. Conf. Mech. Eng., 2007: pp. 29–31.

Acknowledgements

I am deeply grateful to everyone who has supported me during the work for this dissertation and want to specifically thank the following people:

Prof. Dr. Christoph Müller, for accepting me as a PhD student to his group and for being a great scientific advisor. Whilst giving great advice, he always gave me the freedom to try my own solutions (in the end I usually found out he was right all along).

Dr. Lily Poulikakos for being a great academic advisor, for supporting me when I struggled but also pushing me when I needed it.

Dr. Frank Clemens for creating a very welcoming atmosphere in the ceramics laboratory and for guiding me through the arduous process of writing my first paper.

Prof. Dr. Manfred Partl for open-minded discussions and his creative ideas on how to approach challenges.

Prof. Dr. Erik Schlangen for taking time to serve as a co-examiner for this dissertation.

Jens, for quickly becoming the best colleague one could wish and for lending some of his great creativity and intellect to my challenges to find solutions no one else could possibly come up with.

Aga, for her incredible kindness and for always helping me out with orders of material and lab equipment.

225

Lovro Gorjan, Tobias Rantze, Fateme Sarraf and Dr. Tutu Sebastian for introducing me to the world of ceramics processing and additive manufacturing and helping me out in the ceramics lab.

Janine Gremion, for taking care of a lot of administrative tasks, in such a way that I did not have to worry about anything.

My office mates at Empa, Farrokh and Zhengyin for the unique perspectives I gained from our discussions.

Everyone else at Empa for supporting me during the work for this dissertation.

The group of friends who I met during my undergraduate studies; you know who you are. Your companionship kept me going all these years, from studying at the RWI-library all through the PhD. Sharing a few beers and a chat with you means the world to me.

Dani, Lucky and Reto for their great friendship, I have learned so much from every one of you.

My parents for their enduring support and encouragement, I always know you will have my back, no matter which path I take.

My wife Kathrin for her incredible strength and calmness and for giving me wonderful family.